

APPLIED COMPUTATIONAL ELECTROMAGNETICS SOCIETY JOURNAL

February 2014
Vol. 29 No. 2
ISSN 1054-4887

The ACES Journal is abstracted in INSPEC, in Engineering Index, DTIC, Science Citation Index Expanded, the Research Alert, and to Current Contents/Engineering, Computing & Technology.

The illustrations on the front cover have been obtained from the research groups at the Department of Electrical Engineering, The University of Mississippi.

THE APPLIED COMPUTATIONAL ELECTROMAGNETICS SOCIETY

<http://www.aces-society.org>

EDITOR-IN-CHIEF

Atef Elsherbeni

University of Mississippi, EE Dept.
University, MS 38677, USA

ASSOCIATE EDITORS-IN-CHIEF

Sami Barmada

University of Pisa, EE Dept.
Pisa, Italy, 56126

Fan Yang

University of Mississippi, EE Dept.
University, MS 38677, USA

Mohamed Bakr

McMaster University, ECE Dept.
Hamilton, ON, L8S 4K1, Canada

Yasushi Kanai

Niigata Inst. of Technology
Kashiwazaki, Japan

Mohammed Hadi

Kuwait University, EE Dept.
Safat, Kuwait

Mohamed Abouzahra

MIT Lincoln Laboratory
Lexington, MA, USA

Ozlem Kilic

Catholic University of America
Washington DC, 20064, USA

Alistair Duffy

De Montfort University
Leicester, UK

Levent Gurel

Bilkent University
Ankara, Turkey

EDITORIAL ASSISTANTS

Matthew J. Inman

University of Mississippi, EE Dept.
University, MS 38677, USA

Mohamed Al Sharkawy

Arab Academy for Science and
Technology, ECE Dept. Alexandria,
Egypt

EMERITUS EDITORS-IN-CHIEF

Duncan C. Baker

EE Dept. U. of Pretoria
0002 Pretoria, South Africa

Allen Glisson

University of Mississippi, EE Dept.
University, MS 38677, USA

David E. Stein

USAF Scientific Advisory Board
Washington, DC 20330, USA

Robert M. Bevenssee

Box 812
Alamo, CA 94507-0516, USA

Ahmed Kishk

University of Mississippi, EE Dept.
University, MS 38677, USA

EMERITUS ASSOCIATE EDITORS-IN-CHIEF

Alexander Yakovlev

University of Mississippi, EE Dept.
University, MS 38677, USA

Erdem Topsakal

Mississippi State University, EE Dept.
Mississippi State, MS 39762, USA

EMERITUS EDITORIAL ASSISTANTS

Khaled ElMaghoub

University of Mississippi, EE Dept.
University, MS 38677, USA

Anne Graham

University of Mississippi, EE Dept.
University, MS 38677, USA

Christina Bonnington

University of Mississippi, EE Dept.
University, MS 38677, USA

FEBRUARY 2014 REVIEWERS

**Iraj Arghand
Toni Bj
Ivan Bonev
William Coburn
Grant Ellis
Samir Gupta
Abdel Kader Hamid
Julie Huffman**

**Baek Jung
Darko Kajfez
Ali Lalbakhsh
Angelo Liseno
Zi-Liang Liu
Mario Pantoja
Lotfollah Shafai**

THE APPLIED COMPUTATIONAL ELECTROMAGNETICS SOCIETY
JOURNAL

Vol. 29 No. 2

February 2014

TABLE OF CONTENTS

“Time-Domain Integral Equation Solver Using Variable-Order Temporal Interpolators” N. Ojaroudi, M. Mehranpour, S. Ojaroudi, and Y. Ojaroudi.....	116
“Spherical Conformal Bow-Tie Antenna for Ultra-Wide Band Microwave Imaging of Breast Cancer Tumor” I. Ünal, B. Türetken, and C. Canba.....	124
“A CPW-Fed Band-Notched UWB Antenna with T-Shape Construct and Matching Branches” A. Chen, C. Yang, Z. Chen, K. AN, J. Fang, and W. Jiang.....	134
“Modal Analysis for a Waveguide of Nanorods Using the Field Computation for a Chain of Finite Length” Y. Rahbarihagh, F. Kalhor, J. Rashed-Mohassel, and M. Shahabadi.....	140
“Single Feed Dual-Polarization Dual-Band Transmitarray for Satellite Applications” S. Zainud-Deen, S. Gaber,H. Malhat, and K. Awadalla.....	149
“Broad-Band Power Divider Based on the Novel Split Ring Resonators” D. Jiang, Y. Xu, R. Xu, and Z. Shao.....	157
“An Efficient Rough Surface Scattering Analysis for Ray Tracing Algorithm Using Strong Harmonics Extraction and the Kirchhoff Approach” A. Torabi and A. A. Shishegar.....	163
“A Compact UWB Band-Pass Filter with Ultra-Narrow Tri-Notch-Band Characteristic” Y. Li, W. Li, C. Liu, and Qiubo Ye	170
“Microstrip Patch Antenna Covered With Left Handed Metamaterial” E. Dogan, E. Unal, D. Kapusuz, M. Karaaslan, and C. Sabah.....	178
“Application of the Protruded Structures to Design an UWB Slot Antenna with Band-Notched Characteristic” N. Ojaroudi, M. Mehranpour, S. Ojaroudi, and Y. Ojaroudi.....	184

Time-Domain Integral Equation Solver Using Variable-Order Temporal Interpolators

M. Ghaffari-Miab^{1,2}, F. Valdés³, R. Faraji-Dana¹, and E. Michielssen³

¹Centre of Excellence on Applied Electromagnetic Systems, School of Electrical and Computer Engineering, College of Engineering University of Tehran, Tehran, Iran
m.ghaffari@ut.ac.ir, reza@ut.ac.ir

² Department of Engineering Science, College of Engineering, University of Tehran, Tehran, Iran

³ Radiation Laboratory, Department of Electrical Engineering and Computer Science, University of Michigan, Ann Arbor, MI 48104, USA
fvaldes@umich.edu, emichiel@umich.edu

Abstract — A novel, efficient, and simple modification to standard marching-on-in-time (MOT)-based time-domain integral equation (TDIE) solvers is presented. It allows for the use of high-order temporal interpolators without the need to extrapolate and predict future unknowns. The order of these temporal interpolators is increased as the distance of source and testing quadrature points increases. The proposed TDIE solver significantly increases the accuracy of solutions by exploiting high-order temporal interpolation at no significant extra computational cost. Numerical examples are presented to validate the proposed method.

Index Terms - Marching-on-in-time (MOT), temporal interpolator, and time-domain integral equation (TDIE).

I. INTRODUCTION

MOT-based TDIE solvers represent an increasingly mature technology for analyzing transient electromagnetic wave interactions with perfect electrically conducting (PEC) surfaces. To allow for the solution of large-scale scattering problems, these solvers often are accelerated by multilevel plane wave time domain (PWTD) [1] or time-domain adaptive integral methods (TD-AIM) [2]. Their stability and accuracy has been observed to be closely related to the method used for discretizing the surface current in both space and time as well as the method used for evaluation of

MOT matrix elements [3-5]. To increase the accuracy of the spatial discretization, high-order interpolatory [6, 7] or hierarchical [8] spatial basis functions are often used. To enhance the solver's stability, smooth temporal basis functions are preferred [9, 10]. Two basis functions often used for this purpose are Lagrange [11] and Quadratic B-Spline (QBS) interpolants [10]. Their frequency spectra decay as $1/f^2$ and $1/f^3$, respectively; this renders the QBS slightly preferable.

In this paper a new MOT scheme that allows for the use of different temporal interpolators depending on the distance between source and test points, is presented. The advantages of the proposed method are threefold: (i) It increases the accuracy of a TDIE solver without sacrificing its stability or computational efficiency. (ii) It alleviates the introduction of spurious high-frequency modes into the solution without the need to extrapolate and/or predict future unknowns. (iii) When applied to TDIE solvers based on time domain Green's functions (TDGFs) of layered media [12-15], in addition to the above-mentioned advantages, which lead to more stable TDIE solvers, the proposed method significantly decreases the computational expense of taking the convolution of TDGFs with temporal interpolators by increasing the temporal smoothness.

II. STANDARD TIME DOMAIN EFIE

Consider a perfect electrically conducting (PEC) surface S with unit normal vector $\hat{\mathbf{n}}$ that resides in a homogeneous medium with permittivity ϵ and permeability μ . The incident electric field $\mathbf{E}^{inc}(\mathbf{r}, t)$ induces a current $\mathbf{J}(\mathbf{r}, t)$ on S , which generates the scattered electric field $\mathbf{E}^{sca}(\mathbf{r}, t)$. The total electric field $\mathbf{E}^{inc}(\mathbf{r}, t) + \mathbf{E}^{sca}(\mathbf{r}, t)$ tangential to S vanishes. The same therefore is true for its time derivative,

$$\hat{\mathbf{n}} \times [\dot{\mathbf{E}}^{inc}(\mathbf{r}, t) + \dot{\mathbf{E}}^{sca}(\mathbf{r}, t)] = 0 \quad \mathbf{r} \in S. \quad (1)$$

Here, a dot on a symbol implies temporal differentiation, and

$$\dot{\mathbf{E}}^{sca}(\mathbf{r}, t) = -\mu \ddot{\mathbf{A}}(\mathbf{r}, t) + \frac{1}{\epsilon} \nabla \nabla \cdot \mathbf{A}(\mathbf{r}, t) \quad (2)$$

with

$$\mathbf{A}(\mathbf{r}, t) = \iint_S \frac{\mathbf{J}(\mathbf{r}', t - \frac{R}{c})}{4\pi R} d\mathbf{r}', \quad (3)$$

$c = 1/\sqrt{\mu\epsilon}$ is the speed of light, and $R = |\mathbf{r} - \mathbf{r}'|$. To solve equation (1), $\mathbf{J}(\mathbf{r}, t)$ is spatially discretized as,

$$\mathbf{J}(\mathbf{r}, t) = \sum_{n=1}^{N_s} \mathbf{S}_n(\mathbf{r}) I_n(t); \quad (4)$$

$I_n(t)$ is the temporal signature of the n^{th} spatial basis function $\mathbf{S}_n(\mathbf{r})$. Assuming that $\mathbf{E}^{inc}(\mathbf{r}, t)$ is temporally quasi-bandlimited to frequency f_{\max} and vanishingly small for $\mathbf{r} \in S$ and $t < 0$, $I_n(t)$ can be reconstructed from its samples,

$$I_n(j\Delta t) = I_{nj}, \quad j = 1, 2, \dots, N_t \quad (5)$$

as

$$I_n(t) = \sum_{j=1}^{N_t} I_{nj} T(t - j\Delta t) \quad (6)$$

where the time step $\Delta t = 1/(2\beta f_{\max})$, β is a temporal oversampling factor typically chosen in the range $3 < \beta < 20$, and $T(t - j\Delta t)$ is a suitably chosen interpolator. Equation (6) and (4) imply the following space-time discretization of $\mathbf{J}(\mathbf{r}, t)$,

$$\mathbf{J}(\mathbf{r}, t) = \sum_{n=1}^{N_s} \sum_{j=1}^{N_t} I_{nj} \mathbf{S}_n(\mathbf{r}) T(t - j\Delta t). \quad (7)$$

Substituting equation (7) into equations (1-3) and enforcing the resulting equation by Galerkin testing in space and point matching in time yields [1, 2, 16-18],

$$\sum_{j=1}^{N_t} \mathbf{Z}_{i-j} \mathbf{I}_j = \mathbf{V}_i, \quad i = 1, 2, \dots, N_t \quad (8)$$

where

$$[V_i]_m = \iint_S \mathbf{S}_m(\mathbf{r}) \cdot \dot{\mathbf{E}}^{inc}(\mathbf{r}, i\Delta t) ds, \quad [I_j]_m = I_{mj}. \quad (9)$$

and

$$[Z_k]_{mn} = \frac{\mu}{4\pi} \iint_S \iint_{S'} \frac{\mathbf{S}_m(\mathbf{r}) \cdot \mathbf{S}_n(\mathbf{r}')}{R} \ddot{T}(k\Delta t - \frac{R}{c}) ds' ds + \frac{1}{4\pi\epsilon} \iint_S \iint_{S'} \frac{\nabla \cdot \mathbf{S}_m(\mathbf{r}) \nabla' \cdot \mathbf{S}_n(\mathbf{r}')}{R} T(k\Delta t - \frac{R}{c}) ds' ds \quad (10)$$

A temporal interpolator $T(t)$ satisfying,

$$T(t) = 0, \quad t < -\Delta t \quad (11)$$

is said to be causal. For causal interpolators,

$$\mathbf{Z}_{-k} = 0, \quad k = 1, 2, 3, \dots \quad (12)$$

and equation (8) reduces to the standard MOT equations from which the expansion coefficients I_{nj} can be retrieved, one time step at a time,

$$\mathbf{Z}_0 \mathbf{I}_i = \mathbf{V}_i - \sum_{j=1}^{i-1} \mathbf{Z}_{i-j} \mathbf{I}_j, \quad i = 1, 2, \dots, N_t. \quad (13)$$

Next we demonstrate that condition (11) can be relaxed without relinquishing the MOT form of equation (13).

III. DISTANCE-DEPENDENT TEMPORAL INTERPOLATORS

A. Concept

By discretizing the spatial integrations in equation (10) by N_{tqp} test quadrature points and N_{sqp} source quadrature points, equation (8) can be rewritten as,

$$[V_i]_m = \sum_{j=1}^{N_t} \sum_{n=1}^{N_s} [Z_{i-j}]_{mn} [I_j]_n = \sum_{n=1}^{N_s} \sum_{q=1}^{N_{tqp}} \sum_{q'=1}^{N_{sqp}} w_{mq} w_{nq'} \left[a_{mq, nq'} \sum_{j=1}^{N_t} I_{nj} \ddot{T}((i-j)\Delta t - \frac{R_{mq, nq'}}{c}) + b_{mq, nq'} \sum_{j=1}^{N_t} I_{nj} T((i-j)\Delta t - \frac{R_{mq, nq'}}{c}) \right] \quad (14)$$

where

$$a_{mq, nq'} = \frac{\mu \mathbf{S}_m(\mathbf{r}_{mq}) \cdot \mathbf{S}_n(\mathbf{r}'_{nq'})}{4\pi R_{mq, nq'}}, \quad (15)$$

$$b_{mq, nq'} = \frac{\nabla \cdot \mathbf{S}_m(\mathbf{r}_{mq}) \nabla' \cdot \mathbf{S}_n(\mathbf{r}'_{nq'})}{4\pi\epsilon R_{mq, nq'}}$$

with $R_{mq,nq'} = |\mathbf{r}_{mq} - \mathbf{r}'_{nq'}|$, \mathbf{r}_{mq} and $\mathbf{r}'_{nq'}$ are position vectors of q^{th} quadrature point of m^{th} spatial basis function and q'^{th} quadrature point of n^{th} spatial basis functions, respectively, w_{mq} and $w_{nq'}$ are the corresponding quadrature weights.

The two summations inside brackets of equation (14) are nothing but the temporal interpolation of $\dot{I}_n(t)$ and $I_n(t)$, respectively at time $t = i\Delta t - R_{mq,nq'}/c$. More clearly from equation (6) we have,

$$\begin{aligned} I_n(i\Delta t - \frac{R_{mq,nq'}}{c}) &= \sum_{j=1}^{N_t} I_{n_j} T((i-j)\Delta t - \frac{R_{mq,nq'}}{c}) \\ \dot{I}_n(i\Delta t - \frac{R_{mq,nq'}}{c}) &= \sum_{j=1}^{N_t} I_{n_j} \dot{T}((i-j)\Delta t - \frac{R_{mq,nq'}}{c}) \end{aligned} \quad (16)$$

It is easy to see that by replacing $T(t)$ by any other interpolatory function, equations (14)-(16) still remain valid. Moreover, this replacement can be done based on the position of source and test quadrature points. Therefore, a more flexible restriction on $T(t)$ to satisfy equation (12) is,

$$T(t) = 0, \quad t < -\Delta t - \frac{R_{mq,nq'}}{c}. \quad (17)$$

This condition means that as the distance of source and test quadrature points increases, it is allowed to choose wider temporal interpolator $T(t)$ that contradicts equation (11) and still use the MOT scheme of equation (13).

In the next section B-Spline functions of arbitrary order, which are used in numerical results as distance-dependent interpolators are defined.

B. B-Spline functions

B-Spline functions of order m are defined as,

$$b^{(m)}(t) = \frac{1}{\Delta t} b^{(0)}(t) * b^{(m-1)}(t), \quad m = 1, 2, 3, \dots \quad (18)$$

where ‘*’ denotes temporal convolution and

$$b^{(0)}(t) = \text{rect}\left(\frac{t}{\Delta t}\right) = \begin{cases} 1 & , \quad \left|\frac{t}{\Delta t}\right| < 1 \\ 0 & , \quad \text{otherwise} \end{cases} \quad (19)$$

Consider the shifted B-Spline functions defined as,

$$b^{(m)}(t) = b^{(m)}(t - \Delta t / 2), \quad m = 2, 3, 4, \dots \quad (20)$$

Given the definition in equation (18), the spectrum of shifted B-Spline functions of equation (20) is,

$$\begin{aligned} \tilde{b}^{(m)}(f) &= \Delta t \text{Sinc}^{m+1}(f\Delta t) e^{-j\pi f\Delta t} \\ &= \frac{1}{(\Delta t)^m} \left(\frac{\sin(\pi f\Delta t)}{\pi f} \right)^{m+1} e^{-j\pi f\Delta t} \end{aligned} \quad (21)$$

which indicates that the spectrum of B-Spline function of order m , decays as $1/f^{(m+1)}$.

Shifted B-Spline functions of different orders are depicted in Fig. 1. An arbitrary function $s(t)$ can be expanded in terms of B-Spline functions of equations (18) and (19) as,

$$s(t) \approx \sum_{n=-\infty}^{+\infty} s(n\Delta t) b^{(m)}(t - n\Delta t), \quad m \in \{0, 1, 2, \dots\} \quad (22)$$

Note that for the special case of $m=1$, equation (18) is the standard triangular (hat) function and equation (22) is nothing but a piecewise linear interpolation of $s(t)$. Considering equations (20) and (22), it is obvious that an arbitrary function $s(t)$ can also be expanded in terms of shifted B-Spline functions of equation (20) as,

$$s(t - \Delta t / 2) \approx \sum_{n=-\infty}^{+\infty} s(n\Delta t) b^{(m)}(t - n\Delta t), \quad m \in \{2, 3, 4, \dots\} \quad (23)$$

By applying the restriction in equation (17) it is seen that $b^{(m)}(t)$ can be safely used in TDIE solvers for distances R satisfying,

$$R > \frac{(m-2)}{2} c \Delta t. \quad (24)$$

Note that $b^{(2)}(t)$ is the only shifted B-Spline temporal interpolator defined in equation (20) that satisfies equation (17) for the worst case of $R_{mq,nq'} = 0$ and therefore is selected as temporal interpolator for near distances of source and test quadrature points in numerical results.

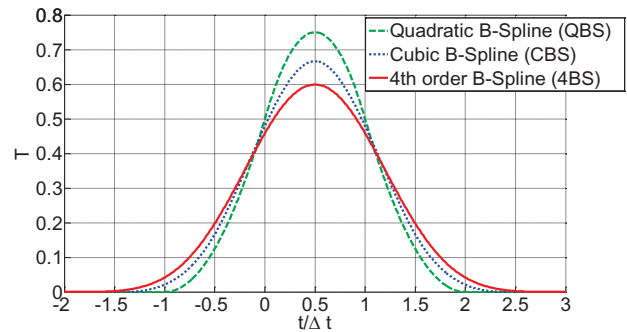


Fig. 1. Shifted B-Spline functions of different order.

IV. NUMERICAL RESULTS

In parts A and B of this section, the above solver is applied to the analysis of scattering from a sphere and cube illuminated by the modulated Gaussian plane wave,

$$\mathbf{E}^{inc}(\mathbf{r}, t) = \hat{\mathbf{x}} e^{-[(t-t_p)/\sqrt{2}\sigma]^2} \cos(2\pi f_0 \tau). \quad (25)$$

with $\tau = t - \mathbf{r} \cdot \hat{\mathbf{z}} / c$, the center frequency $f_0 = 40$ MHz, the delay $t_p = 0.5 \times 10^{-6}$ s, and $\sigma = 6 / (2\pi f_{BW})$ with the nominal bandwidth $f_{BW} = 20$ MHz. The MOT time step is $\Delta t = 6.25 \times 10^{-10}$ s and the number of time steps $N_t = 1600$. In these examples, shifted B-Splines of order $m = 2, 3$, and 4 are used for $R < 0.0938$ m, $0.1875 \text{ m} > R \geq 0.0938$ m, and $R \geq 0.1875$ m, respectively, in agreement with the condition of equation (24). Frequency-domain results attributed to the solver were obtained by Fourier transforming time-domain data while accounting for the spectral content of the incident field.

In part C of this section the proposed distance-dependent temporal interpolation scheme is applied to a recently developed TDIE solver for analyzing planar structures in layered media.

A. Sphere

The surface of a PEC sphere of radius 1 m (centered about the origin) is discretized using 48 curvilinear patches, resulting in $N_s = 72$ spatial RWG basis functions [19]. Each patch is obtained by means of an exact mapping from a reference RWG patch onto the sphere surface.

Fig. 2 (a) shows the bistatic radar cross section (RCS) for $\varphi = 0$ and $-180 \leq \theta \leq 0$ for frequency $f = 43$ MHz and different choices of temporal interpolating functions.

Fig. 2 (b) shows the relative error of the computed RCS with respect to Mie series solution. The norm of current vector \mathbf{I}_j is plotted in

Fig. 2 (c). Clearly the use of a shifted QBS temporal interpolator results in more accurate results compared to Lagrange interpolators [11, 20]. Moreover, as expected, using distance-dependent variable order B-Splines of Fig. 1 as temporal interpolators, significantly increases the accuracy without affecting the stability of solutions. By exploiting variable order B-Splines as temporal interpolators, the worst case relative error in RCS is decreased by 48 % with respect to the case where only QBS is used as temporal interpolator.

B. Cube

The surface of a PEC cube with side length of 1 m (centered about the origin and with cube edges aligned with the major coordinate axes) is discretized using 256 flat patches, resulting in $N_s = 384$ spatial RWG basis functions. Since there is no analytical solution for the cube example, the results of the TDIE solver when the surface current of the cube is densely discretized using 1773 RWG spatial basis functions are considered as reference solution for comparison. The results for frequency $f = 50$ MHz and different choices of temporal interpolating functions are plotted in

Fig. 3. Accuracy improvements on par with those observed in the previous example when using distance-dependent high-order B-Splines are obtained here leading to 45% decrease in worst case relative error in RCS with respect to the case where only QBS is used as temporal interpolator.

C. Microstrip patch antenna array

As the last example, to show the ability of the proposed variable-order and distance-dependent temporal interpolator scheme in increasing the accuracy and therefore the stability of the TDIE solvers, this scheme is incorporated into a recently developed TDIE solver based on the TDGFs of the layered media [15]. In this solver the direct convolution of the TDGFs with temporal interpolators are computed using a novel and highly efficient 2D finite difference scheme.

Consider a 2 by 1 array of microstrip patch antenna as shown in

Fig. 4 (a). The units in this figure are in millimeter. The patch antenna is located over a PEC backed dielectric substrate with relative permittivity of $\epsilon_r = 2.2$ and thickness of $h = 1.524$ mm. The antenna is fed by a modulated Gaussian voltage signal of,

$$V(t) = e^{-[(t-t_p)/\sqrt{2}\sigma]^2} \cos(2\pi f_0 t). \quad (26)$$

With the center frequency $f_0 = 4.5$ GHz, the delay $t_p = 0.5 \times 10^{-8}$ s, and $\sigma = 6 / (2\pi f_{BW})$ with the nominal bandwidth $f_{BW} = 2$ GHz. The surface of the antenna array is discretized using 468 triangular patches, resulting in $N_s = 614$ spatial RWG basis functions. The MOT time step is set to $\Delta t = 5 \times 10^{-12}$ s.

First, we only use QBS as temporal interpolator for all distances of the source to test quadrature points as is used in standard TDIE solvers.

For comparison we also run the solver when shifted B-Splines of order $m = 2, 3$, and 4 are used for $R < 1$ mm, $1 \text{ mm} \leq R < 1.6$ mm, and

$R \geq 1.6 \text{ mm}$, respectively as temporal interpolators in agreement with the condition of equation (24). The TDIE solver runs for $N_t=10000$ time steps. The stability of the TDIE solver is shown in

Fig. 4 (b) where the norm of current vector is plotted. As can be seen from this figure, the standard TDIE solver is unstable while the proposed TDIE solver based on variable order and distance-dependent temporal interpolators gives stable results.

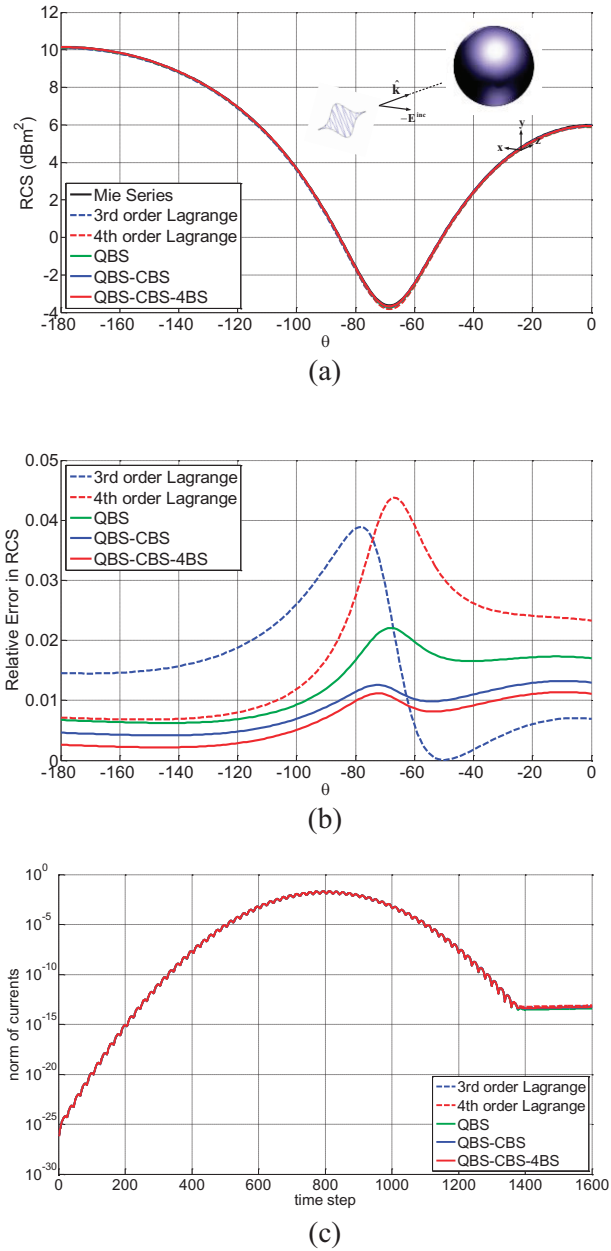


Fig. 2. Bistatic RCS of a unit PEC sphere at 43 MHz for different choices of temporal interpolators. The surface of the sphere is modeled using 48 curvilinear triangular patches. (a) Bistatic RCS, (b) relative error in the RCS with respect to Mei's series solution, and (c) norm of current vector at each time step.

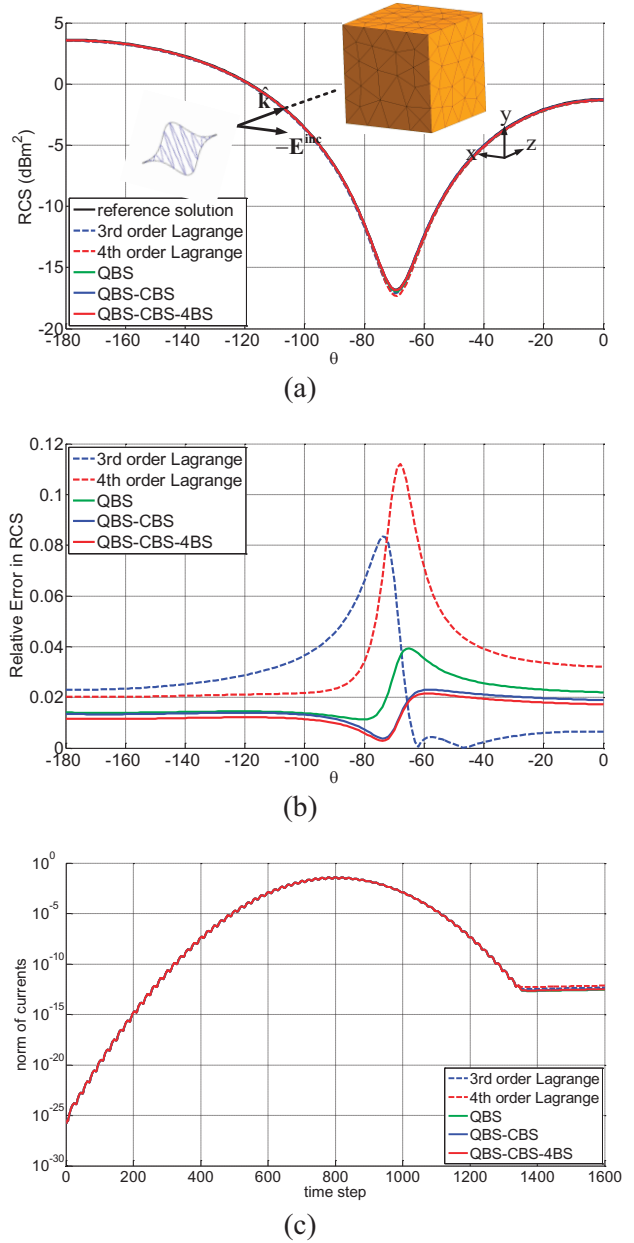


Fig. 3. Bistatic RCS of a PEC cube with side length of 1 m at 50 MHz for different choices of temporal interpolators. The surface of the cube is modeled using 256 flat triangular patches. (a) Bistatic RCS, (b) relative error in the RCS with respect to

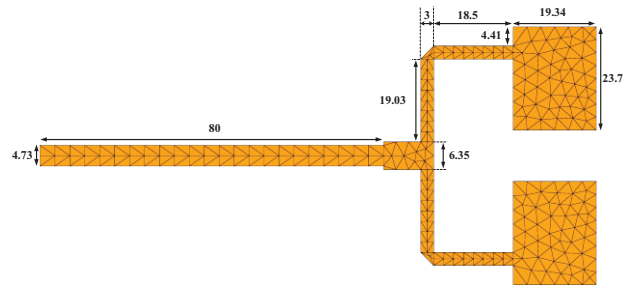
reference solution, and (c) norm of current vector at each time step.

It is worth mentioning that in the second run the only change with respect to the first run is that a fixed temporal interpolator i.e., QBS is replaced with the high-order and distance-dependent temporal interpolators. This replacement not only may increase the accuracy of the solver but also significantly decreases the cost of computing the convolution of temporal interpolators with the TDGFs of layered media by using much more smooth temporal interpolators for non-near pair of source-testquadrature points.

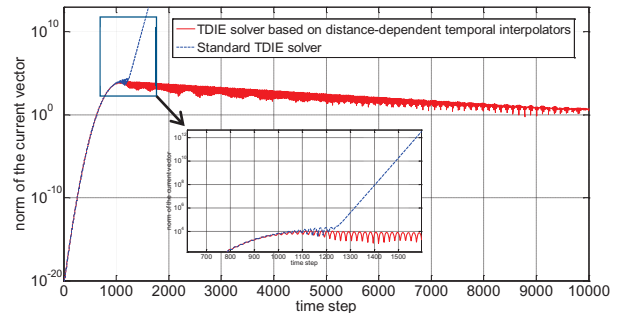
Fig. 4 (c) shows the reflection amplitude $|S_{11}|$ of the patch antenna achieved by using a proper post processing technique applied to the stable time domain surface current output of the proposed TDIE solver based on distance-dependent temporal interpolators. The results are being compared with that of the commercial software ADS-Momentum, which is based on frequency domain method of moments (MoM). A good agreement between the results of two methods is observed.

V. CONCLUSION

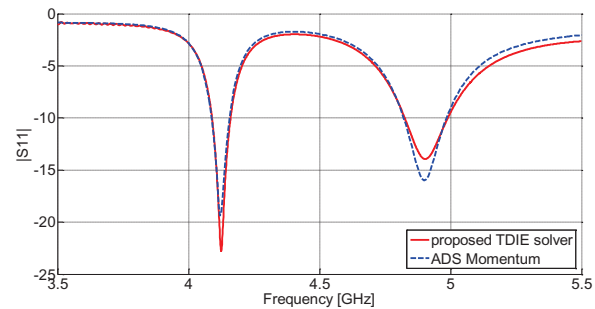
A new MOT-TDIE solver that uses distance-dependent high-order temporal interpolators was introduced. The solver tunes the basis functions' temporal support to the distance between source and observer points, maximizing temporal smoothness and avoiding non-causal excitations along the way. When compared to classically formulated MOT-TDIE schemes, the new method can markedly improve solution accuracy by suppressing high-frequency, out-of-band spurious solution components stemming from the use of temporal interpolators with spectral support far exceeding that of the excitation. The proposed distance-dependent interpolation scheme is also very advantageous in TDIE solvers for analyzing electromagnetic interactions with structures residing in layered media. In this case the proposed method not only may increase the solution accuracy but also can significantly decrease the cost of computing the convolution of temporal interpolators with the TDGFs.



(a)



(b)



(c)

Fig. 4. TDIE analysis of the patch antenna array (a) antenna layout (the units are in millimeter), (b) norm of current vector at each time step using proposed TDIE solver and standard TDIE solver, and (c) the amplitude of the reflection coefficient $|S_{11}|$ achieved using the proposed TDIE solver and its comparison with the results of ADS-Momentum.

REFERENCES

- [1] B. Shanker, A. Ergin, M. Lu, and E. Michielssen, "Fast analysis of transient electromagnetic scattering phenomena using the multilevel plane wave time domain algorithm," *IEEE Transactions on Antennas and Propagation*, vol. 51, pp. 628-641, 2003.
- [2] A. Yilmaz, J.-M. Jin, and E. Michielssen, "Time domain adaptive integral method for surface integral equations," *IEEE Transactions on*

- Antennas and Propagation*, vol. 52, pp. 2692-2708, 2004.
- [3] Y. Shi, M.-Y. Xia, R.-S. Chen, E. Michielssen, and M. Lu, "Stable electric field TDIE solvers via quasi-exact evaluation of MOT matrix elements," *IEEE Transactions on Antennas and Propagation*, vol. 59, pp. 574-585, 2011.
- [4] H. Bagci, A. Glaser, V. Rokhlin, and E. Michielssen, "A new marching-on-in-time scheme for solving the time-domain magnetic field integral equation," *26th Annual Review of Progress in Applied Computational Electromagnetics (ACES)*, pp. 136-141, Tampere, Finland, April 2010.
- [5] A. Pray, N. Nair, and B. Shanker, "A stable higher order time domain electric field integral equation solver," *28th Annual Review of Progress in Applied Computational Electromagnetics (ACES)*, pp. 1034-1039, Ohio, USA, April 2012.
- [6] R. Graglia, D. Wilton, and A. Peterson, "Higher order interpolatory vector bases for computational electromagnetics," *IEEE Transactions on Antennas and Propagation*, vol. 45, pp. 329-342, 1997.
- [7] F. Valdes, M. Ghaffari-Miab, F. Andriulli, K. Cools, and E. Michielssen, "High-order Calderon preconditioned time domain integral equation solvers," *IEEE Transactions on Antennas and Propagation*, vol. 61, pp. 2570-2588, 2013.
- [8] E. Jorgensen, J. Volakis, P. Meincke, and O. Breinbjerg, "Higher order hierarchical Legendre basis functions for electromagnetic modeling," *IEEE Transactions on Antennas and Propagation*, vol. 52, pp. 2985-2995, 2004.
- [9] J.-L. Hu, C. Chan, and Y. Xu, "A new temporal basis function for the time-domain integral equation method," *IEEE Microwave and Wireless Components Letters*, vol. 11, pp. 465-466, 2001.
- [10] M. Xia, G. Zhang, G. Dai, and C. Chan, "Stable solution of time domain integral equation methods using quadratic B-spline temporal basis functions," *Journal of Computational Mathematics*, vol. 25, pp. 374-384, 2007.
- [11] G. Manara, A. Monorchio, and R. Reggiannini, "A space-time discretization criterion for a stable time-marching solution of the electric field integral equation," *IEEE Transactions on Antennas and Propagation*, vol. 45, pp. 527-532, 1997.
- [12] M. Ghaffari-Miab, Z. Firouzeh, R. Faraji-Dana, R. Moini, S. Sadeghi, and G. Vandenbosch, "Time-domain MoM for the analysis of thin-wire structures above half-space media using complex-time Green's functions and band-limited quadratic B-spline temporal basis functions," *Engineering Analysis with Boundary Elements*, vol. 36, pp. 1116-1124, 2012.
- [13] M. Haddad, M. Ghaffari-Miab, and R. Faraji-Dana, "Transient analysis of thin-wire structures above a multilayer medium using complex-time Green's functions," *IET Microwaves, Antennas, and Propagation*, vol. 4, pp. 1937-1947, 2010.
- [14] M. Ghaffari-Miab, A. Farmahini-Farahani, R. Faraji-Dana, and C. Lucas, "An efficient hybrid swarm intelligence-gradient optimization method for complex time Green's functions of multilayer media," *Progress In Electromagnetics Research, PIER*, vol. 77, pp. 181-192, 2007.
- [15] M. Ghaffari-Miab, F. Valdes, R. Faraji-Dana, and E. Michielssen, "Time-domain integral equation solver for planar structures in layered media," in *IEEE International Symposium on Antennas and Propagation and USNC/URSI National Radio Science Meeting*, Lake Buena Vista, FL, 2013.
- [16] R. Wildman, G. Pisharody, D. Weile, S. Balasubramaniam, and E. Michielssen, "An accurate scheme for the solution of the time-domain Integral equations of electromagnetics using higher order vector bases and bandlimited extrapolation," *IEEE Transactions on Antennas and Propagation*, vol. 52, pp. 2973-2984, 2004.
- [17] F. Andriulli, H. Bagci, F. Vipiana, G. Vecchi, and E. Michielssen, "A marching-on-in-time hierarchical scheme for the solution of the time domain electric field integral equation," *IEEE Transactions on Antennas and Propagation*, vol. 55, pp. 3734-3738, 2007.
- [18] A. Ergin, B. Shanker, and E. Michielssen, "The plane-wave time-domain algorithm for the fast analysis of transient wave phenomena," *IEEE Antennas and Propagation Magazine*, vol. 41, pp. 39-52, 1999.
- [19] S. Rao, D. Wilton, and A. Glisson, "Electromagnetic scattering by surfaces of arbitrary shape," *IEEE Transactions on Antennas and Propagation*, vol. 30, pp. 409-418, 1982.
- [20] A. Geranmayeh, W. Ackermann, and T. Weiland, "Survey of temporal basis functions for integral equation methods," in *Computational Electromagnetics in Time-Domain, CEM-TD*, pp. 1-4, 2007.



Mohsen Ghaffari-Miab received the B.Sc., M.S., and Ph.D. degrees all in Electrical Engineering from the University of Tehran, Tehran, Iran, in 2005, 2007, and 2012, respectively. From 2010 to 2011, he was a Visiting Scholar at the University of Michigan, Ann Arbor, MI, USA. From 2012 to 2013 he was a Postdoctoral Fellow at the University of Tehran. His research interests include computational electromagnetics, with focus on frequency- and time-domain integral equation-based

methods, analysis of layered media, scattering and antenna analysis, and planar microwave circuits.



Felipe Valdés received the B.S. degree in Electrical Engineering from Pontificia Universidad Católica de Chile, Santiago, Chile, in 2004, and the Ph.D. degree in electrical engineering from the University of Michigan, Ann Arbor, MI, USA, in 2012. From

August 2006 to December 2011, he was a Research Assistant at the Radiation Laboratory, University of Michigan. Since 2012, he has been a Software Engineer at Nimbic Inc., Santiago, Chile. His main research interest is in computational electromagnetics, with focus on preconditioning, single source integral equations in time- and frequency-domain, and fast solvers for the analysis of signal and power integrity at printed circuit board and package levels. Dr. Valdés was the recipient of a Fulbright Doctoral Fellowship in 2006–2010.



Reza Faraji-Dana received the B.Sc. degree (with honors) from the University of Tehran, Tehran, Iran, in 1986 and the M.A.Sc. and Ph.D. degrees from the University of Waterloo, Waterloo, ON, Canada, in 1989 and 1993, respectively, all in electrical engineering. He was a

Postdoctoral Fellow with the University of Waterloo for one year. In 1994, he joined the School of Electrical and Computer Engineering, University of Tehran, where he is currently a Professor. He has been engaged in several academic and executive responsibilities, among which was his deanship of the Faculty of Engineering for more than four years, up until summer 2002, when he was elected as the University President by the university council. He was the President of the University of Tehran until December 2005. He is the author of several technical papers published in reputable international journals and refereed conference proceedings and received the Institution of Electrical Engineers Marconi Premium Award in 1995. He was the Chairman of the IEEE-Iran Section from 2007 until 2009. Prof. Faraji-Dana is an associate member of the Iran Academy of Sciences.



Eric Michielssen received the M.S. degree in Electrical Engineering (*summa cum laude*) from the Katholieke Universiteit Leuven (KUL), Leuven, Belgium, in 1987, and the Ph.D. degree in Electrical Engineering from the University of

Illinois, Urbana-Champaign (UIUC), IL, USA, in 1992. He joined the faculty of the UIUC Department of Electrical and Computer Engineering in 1993, reaching the rank of Full Professor in 2002. In 2005, he joined the University of Michigan (UM) as Professor of Electrical Engineering and Computer Science. Since 2009, he directs the University of Michigan Computational Science Certificate Program. His research interests include all aspects of theoretical and applied computational electromagnetics. His research focuses on the development of fast frequency and time domain integral-equation-based techniques for analyzing electromagnetic phenomena, and the development of robust optimizers for the synthesis of electromagnetic/optical devices.

Dr. Michielssen received a Belgian American Educational Foundation Fellowship in 1988 and a Schlumberger Fellowship in 1990. Furthermore, he was the recipient of a 1994 International Union of Radio Scientists (URSI) Young Scientist Fellowship, a 1995 National Science Foundation CAREER Award, and the 1998 Applied Computational Electromagnetics Society (ACES) Valued Service Award. In addition, he was named 1999 URSI United States National Committee Henry G. Booker Fellow and selected as the recipient of the 1999 URSI Koga Gold Medal. He also was awarded the UIUC's 2001 Xerox Award for Faculty Research, appointed 2002 Beckman Fellow in the UIUC Center for Advanced Studies, named 2003 Scholar in the Tel Aviv University Sackler Center for Advanced Studies, selected as UIUC 2003 University and Sony Scholar; in 2011 he received the UM College of Engineering David E. Liddle Research Excellence Award. He is a Fellow of the IEEE (elected 2002) and a member of URSI Commission B. He served as the Technical Chairman of the 1997 Applied Computational Electromagnetics Society (ACES) Symposium (Review of Progress in Applied Computational Electromagnetics, March 1997, Monterey, CA), and served on the ACES Board of Directors (1998–2001 and 2002–2003) and as ACES Vice-President (1998–2001). From 1997 to 1999, he was as an Associate Editor for *Radio Science*, and from 1998 to 2008 he served as Associate Editor for the IEEE Transactions on Antennas and Propagation. He authored or co-authored over 160 journal papers and book chapters and over 300 papers in conference proceedings.

Spherical Conformal Bow-Tie Antenna for Ultra-Wide Band Microwave Imaging of Breast Cancer Tumor

İ. Ünal¹, B. Türetken^{1,2}, and C. Canbay³

¹ Millimeter Wave and Terahertz Technologies Research Laboratories (MILTAL)
Material Institute, TUBITAK-MRC, Gebze, Kocaeli, 41470, Turkey
ilhami.unal@tubitak.gov.tr, bahattin.turetken@tubitak.gov.tr

² TUBITAK-BILGEM, Gebze, Kocaeli, 41470, Turkey

³ Department of Electrical and Electronics Engineering
Yeditepe University, İstanbul, 34755, Turkey
canbay@yeditepe.edu.tr

Abstract — In this paper, contribution of spherical conformal ultra-wide band (UWB) bow-tie antenna on enhancement of breast tumor detection capability of a radar-based microwave imaging system is investigated through simulation, demonstrating the potential of the novel antenna element used in a half-spherical antenna array surrounding the breast. The designed conformal antenna operates efficiently across the band from 1 GHz to 8 GHz, and it is immersed in a coupling medium in order to get a good impedance matching with the breast. Images are successfully formed by using delay-and-sum (DAS) algorithm for the detection of a spherical tumor model with 2 mm diameter. The tumor is located at 40 mm depth inside three different breast phantom models with homogeneous fatty breast tissue, quasi-heterogeneous mix of fibro-glandular and fatty breast tissues and homogeneous fibro-glandular tissue, respectively. Fidelity factor, indicating the maximum cross correlation between observed and excitation pulses, of the conformal bow-tie is found to be around 13% more than that of the planar bow-tie at 40 mm depth. The use of the spherical conformal antenna presents an excellent solution to increase tumor responses by at least 2.3 dB, as well as to decrease mutual coupling effects between array elements, compared to the same system with planar bow-tie antennas.

Index Terms - Breast cancer, conformal bow-tie antennas, and UWB microwave imaging.

I. INTRODUCTION

Early diagnosis and treatment are the hot keys to survive from breast cancer. The present “golden” standard screening technology for detecting early-stage breast cancer is X-ray mammography. However, it has several limitations, especially when dealing with younger women who have dense breast tissues. It also requires painful and uncomfortable breast compression and exposes the patient to ionizing radiation.

Electromagnetic waves and antennas have a huge application area, and one of the challenging areas is remote sensing systems and detection systems using microwaves, today. Increasing demand on non-destructive sensing or detecting breast tumor keeps this subject hot in this field. There are various passive and active microwave techniques, which have been proposed as an alternative especially to the most widely used X-ray mammography; such as microwave radiometry [1], hybrid microwave-induced acoustic imaging [2], microwave tomography [3], and UWB microwave radar technique [4-6].

Currently, there are two main active methods that involve illuminating the breast with microwaves and then measuring transmitted or backscattered signals, such as microwave

tomography and radar-based imaging. In microwave tomography, a nonlinear inverse scattering problem is solved to reconstruct an image of the spatial distribution of dielectric properties in the breast. On the other hand, UWB radar-based imaging approach deals with only to identify the presence and location of significant scattering obstacles such as malignant breast tumors [7].

There is a small contrast between healthy and diseased breast tissues at X-ray frequencies [4]. However, resolution in X-rays is absolutely better than in microwaves. On the other hand, the physical basis for microwave detection of breast tumor is the significant contrast in the electrical properties of the normal and the malignant breast tissues [4], which exists in the earliest stage of tumor development. Another advantage of the microwave imaging technique is that it would be nonionizing and it doesn't require painful breast compression. Other available screening techniques such as ultrasound and MRI are either less effective or are too costly.

Because of its excellent advantages, recent years have shown a dominant interest in UWB microwave imaging technique, for a particular technique to detect and locate a breast tumor [4-15]. This technique specifically involves transmitting and receiving short duration pulses for various locations of UWB probe antenna or alternatively by an antenna array controlled with switches. The UWB imaging technique offers creation of an image, which can be formed by combining all of the signals (S_{ii} and S_{ij} , $i \neq j$) coming from different antennas. Well-known DAS algorithm would be used to create microwave images of breast cancer tumors [4]. In order to enhance tumor detection capability, the radar-based technique requires the use of more sensitive antennas operating over a considerable UWB frequency range.

In this study, UWB microwave imaging technique is used in the 1 GHz – 8 GHz frequency range, which guarantees balance between reasonable contradictory needs of better spatial resolution, better penetration depth [11], less attenuation of electromagnetic waves through the breast and smaller dimensions of a multi-function active imaging system. The selected frequency range is expected to provide reasonable tumor detection capabilities. In particular, since the skin

reflections back to the antenna adversely affect imaging results, better penetration of electromagnetic waves into the breast tissue will be determined by operating the antenna in a coupling medium whose dielectric properties are close to the breast tissue. Antenna size would also be selected to be smaller since the wavelength in the coupling medium will be smaller than air.

Several different types of antennas have been considered and reported over the past decade by research groups involved in radar-based UWB breast imaging; such as ridged pyramidal horn [7], UWB planar bow-tie [8], cross-polarized types [9-10], U-slot [11-12], antipodal Vivaldi [13], stacked microstrip patch [12, 14], tapered slot [15], etc. These antennas were generally used and tested in planar, cylindrical or spherical scanning surfaces, as a single element or in an antenna array. There are also a lot of advantages of using circular or hemispherical antenna array configurations compared to planar ones; such as increased tumor detection sensitivity, enhancement on signal reception [16], increased illuminated coverage area inside the breast [17], better signal-to-clutter (S/C) ratio [18], etc. However, mutual coupling effects of array elements can negatively impact antenna performance and imaging results, too [19].

On the other hand, in order to detect the weak reflections from small tumors located in tissues ranging from fatty breast to glandular, a high sensitive antenna is required to send and receive electromagnetic waves with low pulse distortion and low mutual coupling effects in the array. Since antennas are assumed to be operating in the near field region in which spherical waves exist, antenna geometry and polarization should be appropriately selected to perfectly match with the spherical waves inside the breast, too [20].

This paper presents herein spherical conformal bow-tie antennas to improve tumor detection capability of the microwave imaging system. Conventional planar UWB bow-tie antennas are curved onto a hemi-sphere surface to investigate its effects on enhancement of tumor responses and signal energies [21].

Seven UWB spherical conformal bow-tie antennas are located 4.7 mm above different half-spherical breast phantoms that are modeled on the full-wave electromagnetic simulator (CST Microwave Studio®), which is based on the FIT

method, to calculate the performance of the antennas. All of the time-domain signals (S_{ii} and S_{ij} , $i \neq j$) coming from different antennas are obtained from the simulation model with and without 2 mm diameter tumor at 40 mm depth inside breast phantom models with homogeneous fatty breast tissue, quasi-heterogeneous mix of fibro-glandular and fatty breast tissues, and homogeneous fibro-glandular tissue, by feeding each antenna sequentially. Recorded data are processed on DAS algorithm, and then images of the computed backscattered signal energies for each pixel are created as a function of position. Imaging results of the microwave imaging system with the conformal bow-tie antennas are successfully compared to the same system with planar bow-tie antennas.

This paper is organized as follows: the layered half-spherical breast phantom model, antenna design results and antenna array structure are introduced with comparative antenna simulations in section 2, followed by pulse distortion analysis. In section 3, after briefly outlining the DAS imaging algorithm, imaging results and discussions are given for different breast phantom models. Section 3 also presents tumor responses for the novel antenna and mutual coupling effects of array elements with comparative results in details. Finally, the findings of the study are briefly given in section 4.

II. SIMULATION STUDY

A. Layered half-spherical breast phantom models

Layered breast phantom model consists of a skin tissue layer with thickness of 2 mm and three different half-spherical tissues with radius of 58 mm under the skin, such as homogeneous fatty breast, quasi-heterogeneous mix of fibro-glandular

and fatty breast, and homogeneous fibro-glandular tissues (Fig. 1). The homogeneous fatty breast, quasi-heterogeneous and homogeneous fibro-glandular phantom models represent “mostly fatty”, “heterogeneously dense” and “very dense” phantom models, respectively.

The breast phantom is surrounded by a coupling medium in which antennas are placed, to reduce adverse effects of signal reflections at the antenna-air-breast interface [15]. Non-dispersive relative dielectric permittivity ϵ_r and conductivity σ values of skin, ducts, fatty breast, fibro-glandular and tumor tissues are selected, as in Table I. Dielectric properties of the coupling medium are selected as $\epsilon_r = 9$, $\sigma = 0$ S/m [18].

Table I: Dielectric properties of the tissues.

Tissue	ϵ_r	σ (S/m)
Skin [15]	36	4
Ducts [11]	37.96	4.5
Fatty Breast Tissue [7]	9	0.4
Glandular Tissue [11]	21.5	1.7
Tumor [18]	50	7

Differently sized glands of spherical (radius 8.5 mm $< r < 12.5$ mm) shape [22] are embedded in the fatty breast tissue for the quasi-heterogeneous phantom model, as shown in Fig. 1 (b).

B. Antenna design

Use of the spherical conformal antenna structure is presented here for breast cancer imaging, and it is aimed to be used as an element of a microwave imaging system operating between 1 GHz and 8 GHz. The intended use of conformal antenna is expected to increase the dynamic range of the system as well as to diminish mutual

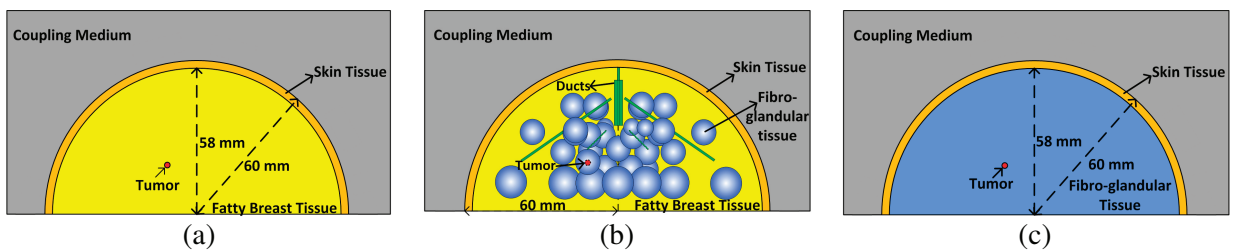


Fig. 1. Schematic illustration of layered half-spherical breast phantom models with (a) homogeneous fatty breast tissue, (b) quasi-heterogeneous mix of fibro-glandular and fatty breast tissues, and (c) homogeneous fibro-glandular tissue.

coupling effects between array elements and pulse signal distortion through the breast.

The planar bow-tie antenna (26 mm × 40 mm), which is curved onto a hemi-sphere surface is aimed to be used as an UWB probe element of a half-spherical antenna array (Fig. 2 (a)). The wavelength at the center frequency (4.5 GHz) is 22 mm inside the coupling medium. The antenna-skin distance has been obtained as 4.7 mm, by optimizing the distance with parametric sweep for the purpose of best matching over the bandwidth. This value is close to the expected theoretical distance, which is approximately quarter-wavelength at the center frequency [23, 24]. If the antennas are not located at this optimal distance, the antenna gain is reduced.

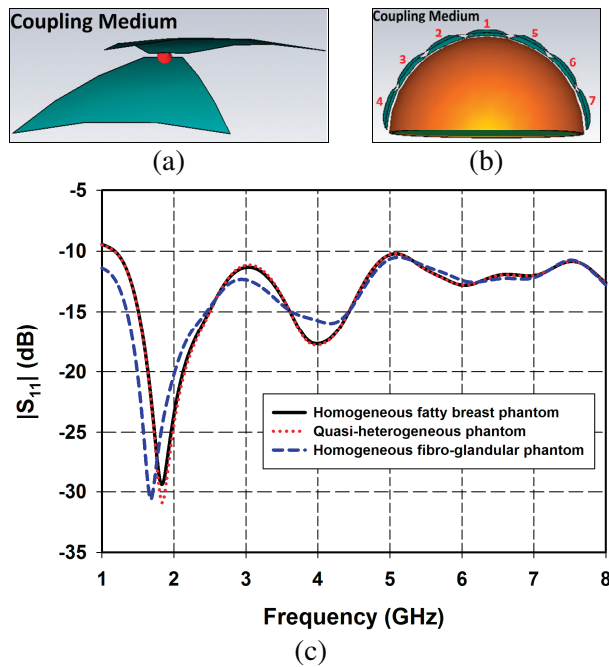


Fig. 2. (a) Spherical conformal bow-tie antenna, (b) simulation model of spherical conformal bow-tie antenna array in front of the breast phantom, and (c) return loss of the spherical conformal bow-tie antenna in the half-spherical antenna array encircling different breast phantoms.

The conformal bow-tie antenna is designed for operating with other antenna elements in the half-spherical antenna array and also in front of the breast phantom model (Fig. 2 (b)). Comparative results of return loss of the conformal bow-tie antenna encircling different breast phantom models

are shown in (Fig. 2 (c)). The simulation results are obtained for the 1st antenna located at the center of the half-spherical antenna array, as shown in Fig. 2 (b). The results show that the -10 dB bandwidth of the antenna, which is operating in the half-spherical antenna array surrounding the breast phantom extends from nearly 1 GHz to above 8 GHz.

As the UWB microwave imaging system operates in the time domain by sending a narrow pulse to penetrate the breast and measures the scattered pulses, it is important to study distortion when the radiated pulse propagates through especially the quasi-heterogeneous breast phantom [15]. For this purpose, the transmitted pulse from the 1st antenna located at the center of the half-spherical antenna array is monitored at different distances normal from the antenna aperture. The time domain performance of the conformal bow-tie antenna will be compared to that of the planar bow-tie antenna, as in Fig. 3.

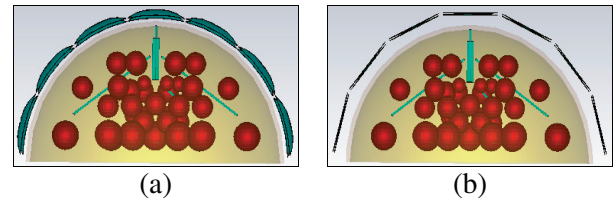


Fig. 3. (a) Spherical conformal bow-tie antennas and (b) planar bow-tie antennas, in the presence of quasi-heterogeneous breast phantom model.

In order to find out the distortion level in the transmitted pulses inside the breast phantom model, the fidelity factor is calculated at different locations within the breast. The fidelity factor is defined as the maximum magnitude of the cross correlation between the observed pulse ($s_R(t)$) at a certain distance and the excitation pulse ($s_T(t)$) [12],

$$F = \max_{\tau^d} \frac{\int_{-\infty}^{\infty} s_T(t) s_R(t - \tau^d) dt}{\sqrt{\int_{-\infty}^{\infty} |s_T(t)|^2 dt \cdot \int_{-\infty}^{\infty} |s_R(t)|^2 dt}}, \quad (1)$$

where τ^d is the required time delay for obtaining maximum magnitude of the cross correlation.

The results indicate an increasing pulse distortion as the signal propagates through the

heterogeneous breast phantom due to the multiple reflections inside the phantom model [15]. For the case with planar bow-tie antenna, the fidelity factor decreases more and it becomes 45.2 % at 40 mm depth inside the breast (Fig. 4). On the other hand, the fidelity factor is kept at higher values in overall when the antenna is spherical conformal bow-tie. That is around 58.2 % at 40 mm depth inside the breast. Moreover, for the conformal bow-tie antenna presented in this paper, the fidelity factor is within reasonable values (around more than 60 %) even inside the breast phantom [25].

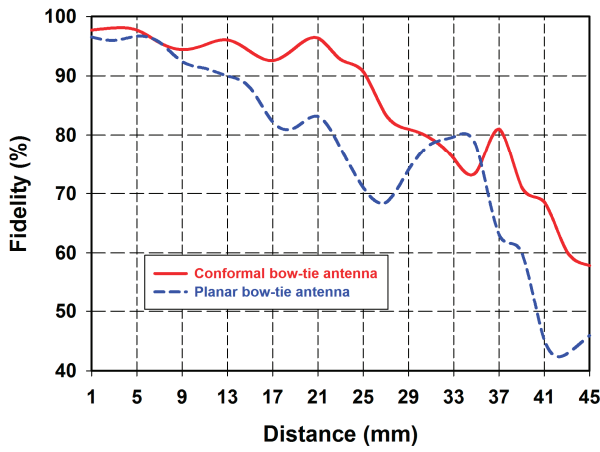


Fig. 4. Calculated fidelity factors with respect to distance from the antenna, in the presence of quasi-heterogeneous breast phantom model.

In order to find out mutual coupling effects of array elements in Fig. 3, conformal and planar bow-tie antennas are compared to each other for S_{21} characteristics between the 1st and 2nd antennas, as shown in Fig. 5. It is observed that the overall S_{21} characteristics of the conformal antenna show less mutual coupling effects, with the exception of higher coupling effects in around 1 GHz -1.3 GHz and 3.6 GHz - 5 GHz frequency bands. However, these bands correspond to 24 % of the whole band. Moreover, the areas under the curves of S_{21} characteristics versus frequency for the conformal antenna are less than that of the planar antenna, indicating lower mutual coupling effects in the overall.

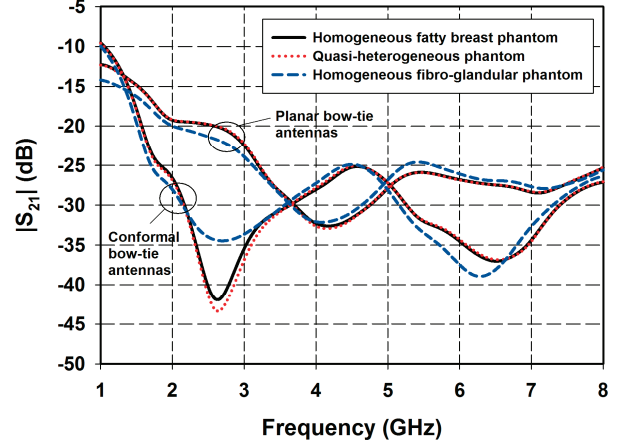


Fig. 5. S_{21} characteristics of conformal and planar bow-tie antennas in the half-spherical antenna array encircling different breast phantoms.

III. IMAGING RESULTS AND DISCUSSION

When one of the seven UWB bow-tie antennas in the array is excited by Gaussian pulse, backscattered time-domain signals (S_{ii} and S_{ij} , $i \neq j$) are recorded. This procedure is repeated by feeding each antenna sequentially, for cases with and without 2 mm diameter tumor. Therefore, 49 time-domain signals (including 28 independent time-domain signals) coming from different antennas are recorded for each case. Tumor response signals S_{ij}^T are obtained by calibrating the recorded signals as in equation (2),

$$S_{ij}^T = S_{ij} \Big|_{\text{with tumor}} - S_{ij} \Big|_{\text{without tumor}}. \quad (2)$$

The tumor response signals are additionally compensated for $1/r$ attenuation of electric fields inside the breast. When the 1st antenna is fed and signal is received from 3rd antenna, one can easily compute time delay for the possible tumor location depicted in Fig. 6. Accordingly, time delay between the transmitted signals from 1st antenna and the received signal by 3rd antenna can be computed as in equation (3), regarding velocities of electromagnetic fields in different media, individually,

$$\tau_{31}^d(\vec{r}) = \frac{d_1^{31}(\vec{r})}{v_{\text{coupling}}} + \frac{d_2^{31}(\vec{r})}{v_{\text{skin}}} + \frac{d_3^{31}(\vec{r})}{v_{\text{breast}}} + \frac{d_4^{31}(\vec{r})}{v_{\text{breast}}} + \frac{d_5^{31}(\vec{r})}{v_{\text{skin}}} + \frac{d_6^{31}(\vec{r})}{v_{\text{coupling}}}. \quad (3)$$

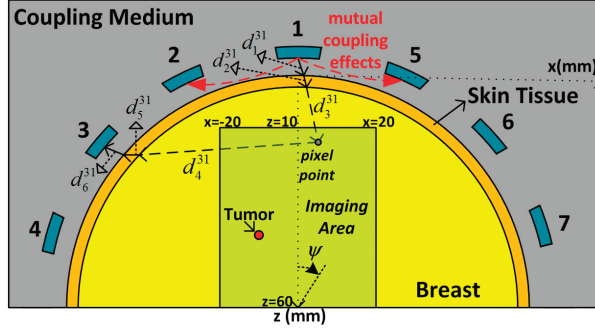


Fig. 6. Illustration of mutual coupling effects (red paths) and signal path, when 1st antenna is fed and 3rd antenna is in receiving mode (black path).

In fact, the heterogeneity of the breast would change the velocities inside the breast. As the antenna positions with respect to each other are known, the mean velocities inside three different breast phantom models are successfully obtained by using time-delay differences between arbitrarily selected S_{54} and S_{74} time-domain signals, as shown in Fig. 7. Although, the DAS algorithm is known as unsuitable for the frequency dispersive tissues, the same practical method can also be successfully used with the DAS algorithm for both heterogeneous and dispersive breast phantom models without any detected tumor location error [21]. However, only non-dispersive case is considered for simplicity, in this paper.

Total tumor response for each pixel is obtained, as in equation (4), regarding computed time delays between each antenna and pixel points, one by one [4]. Then, images of the computed scattered signal energies for each pixel are created as a function of position,

$$T(\vec{r}) = \left[\sum_{i=1}^7 \sum_{j=1}^7 S_{ij}^T(\tau_{ij}^d(\vec{r})) \right]^2. \quad (4)$$

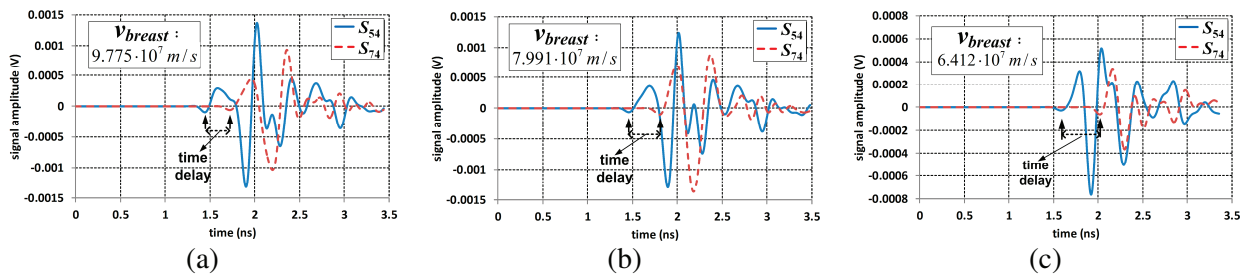


Fig. 7. Velocities obtained by using time delays between S_{54} and S_{74} signals for (a) homogeneous fatty, (b) quasi-heterogeneous, and (c) homogeneous fibro-glandular breast phantom models.

Firstly, the effect of spherical conformal antenna structure on the tumor response will be compared to that of the planar bow-tie antenna. Three different breast phantom models are used in the simulations. Since the peak-to-peak voltage of the excitation pulse ($s_T(t)$) is 1.7 V, the tumor response (in dB) is calculated using the “uncompensated” time-domain tumor response signals S_{ij}^T , as follows [8],

$$Tumor\ Response(dB) = 20 \cdot \log \left(\frac{(S_{ij}^T)_{peak-peak}}{1.7} \right). \quad (5)$$

Tumor responses (in dB) corresponding to highest signal levels S_{12}^T and lowest signal levels S_{17}^T , are given in Fig. 8, with comparable results for conformal and planar bow-tie antennas operating in the presence of different breast phantom models. Each neighbor antenna is separated by 25° with respect to the bottom center of the breast phantom (0, 0, 60 mm). As an example, in the case of S_{42}^T , S_{12}^T , and S_{72}^T tumor response signals, ψ is equal to -75°, 0°, and 75°, respectively (See Fig. 6).

Comparing the calculated tumor response levels of the conformal bow-tie antenna with those of the planar bow-tie antenna, they increase when the conformal antennas are used (Fig. 8). Signal enhancement is observed between 2.3 dB and 5.7 dB in overall for the conformal antenna case. The reduction of tumor responses in the planar bow-tie antenna case is possibly related with worse pulse distortion and mutual coupling effects (Fig. 7). The conformal structure also achieves good polarization matching with spherical waves inside the breast, because of its spherical conformal geometry, too [20]. The tumor response levels of

S_{67}^T and S_{77}^T show unexpected increment for the case of antennas operating in the presence of homogeneous fibro-glandular breast phantom, as shown in Fig. 8 (b). Obtained S_{67}^T and S_{77}^T signals are found to be lower than the minimum detectable signal level in the simulation software, resulting wrong computation of tumor responses.

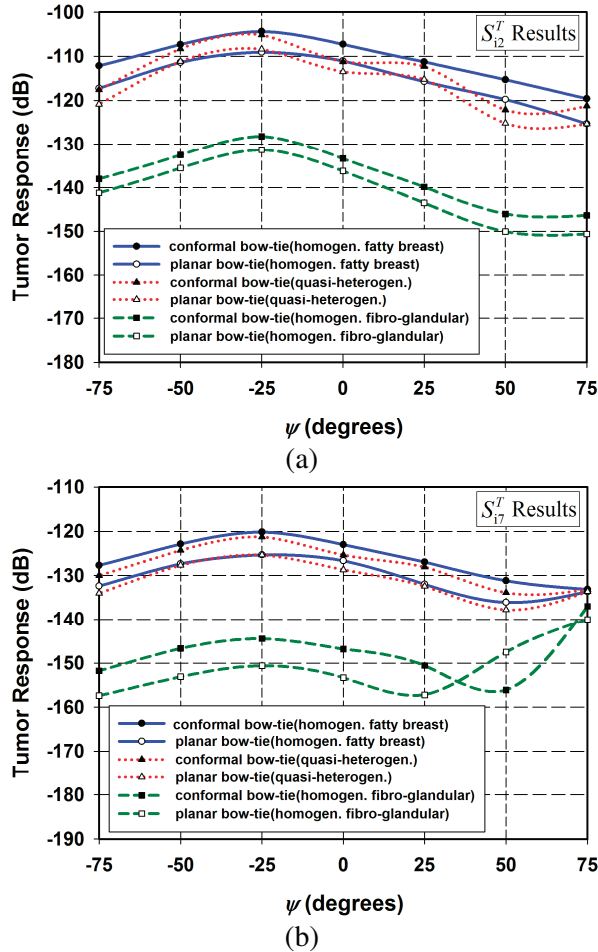


Fig. 8. Results of tumor responses (dB) corresponding to (a) S_{12}^T and (b) S_{17}^T , with respect to ψ .

On the other hand, the peak tumor responses of the conformal antenna for both S_{12}^T or S_{17}^T are found about 1 dB and 23 dB larger when the antenna is operated in the presence of homogeneous fatty breast and quasi-heterogeneous phantoms, respectively, than when it's operated in the presence of homogeneous fibro-glandular breast phantom. The tumor response results, in

Fig. 8, also show dynamic range requirements for the detection of the tumor with 2 mm diameter at 40 mm depth. Since dynamic range of a vector network analyzer can reach down to -140 dB for experimental measurements [26], the tumor responses are not high enough to detect the tumor embedded in the homogeneous fibro-glandular breast, mimicking very dense breast tissue.

Moreover, the area under the curves of tumor responses versus different ψ angles decreases as the breast becomes denser with fibro-glandular tissues. As expected, these results also show that detecting tumor in homogeneous fatty breast tissue is easier than in quasi-heterogeneous and homogeneous fibro-glandular tissues, respectively.

Normalized imaging results of breast cancer tumor with 2 mm diameter are presented in logarithmic scale, as shown in Fig. 9. Normalization is done within each breast phantom case, separately. Comparing the calculated signal energies of the conformal bow-tie antenna with the planar bow-tie antenna, signal levels increase when spherical conformal antennas are used. The increment is 4.8 dB, 6.9 dB, and 3.1 dB in the presence of homogeneous fatty breast, quasi-heterogeneous, and homogeneous fibro-glandular breast phantoms, respectively.

On the other hand, the 50 cm \times 40 cm imaging area in Fig. 7 is sampled with 1-mm pixel resolution and the DAS algorithm was performed on a single core of an Intel i5-2410M @ 2.30 GHz. In this case, the computation time is too long (i.e., more than half of a day) to obtain only one 2-D microwave image. Therefore, parallel computing tools on graphics processing units of a workstation with multicores as well as computationally efficient algorithms should be used to speed up the computation time for imaging [29].

The calibration measurements over the breast without tumor (equation (2)) cannot be used in clinic applications. Because differential imaging method [6] does not require a background measurement, it can be used in clinical scenarios. The first measurement should be performed with the array in a given position, then the array is rotated (in a horizontal plane, around its central vertical axis) and a second measurement is recorded. Those two measurements are then subtracted, resulting in a differential signal, which is used as an input into imaging algorithm. A

detailed description of this method can be found in [6]. More anatomically realistic breast phantom models with dispersive dielectric properties [27-28] should be included to observe the feasibility of the spherical conformal bow-tie antennas better for use in the microwave imaging system. However, obtained results are encouraging that an improvement could be also achieved by adding more and smaller conformal antennas to the array encircling the breast, to enhance detection capability of the microwave imaging system more [6].

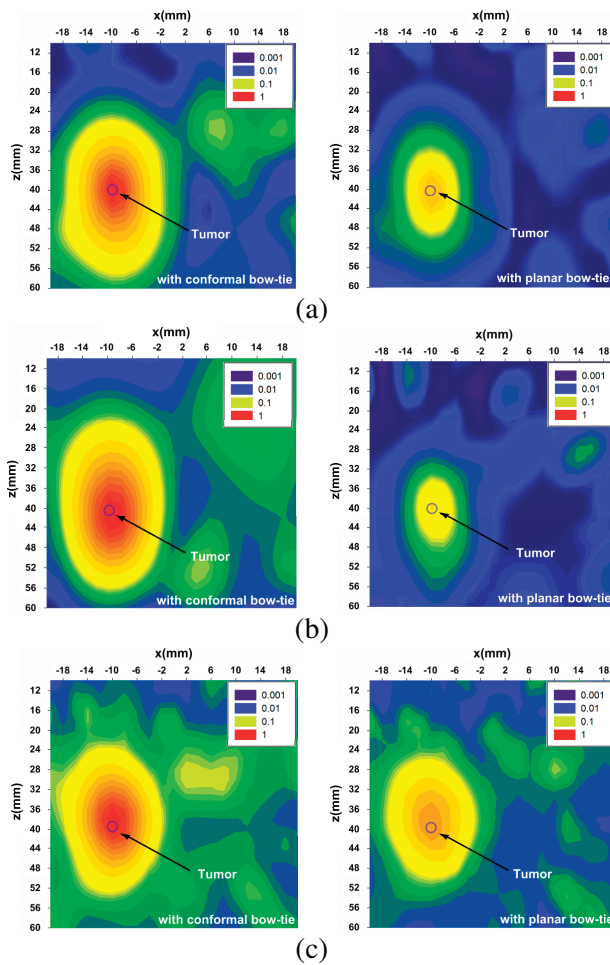


Fig. 9. Images of breast cancer tumor with 2 mm diameter embedded in (a) homogeneous fatty breast, (b) quasi-heterogeneous, and (c) homogeneous fibro-glandular breast phantoms.

IV. CONCLUSION

An UWB spherical conformal bow-tie antenna array surrounding the breast has been designed

and tested on the full-wave electromagnetic simulator, in order to investigate the effects of conformal structure on tumor detection capability of the microwave radar-based imaging system. The proposed bow-tie antenna with spherical curvature would be an attractive candidate element for radar-based breast cancer detection to achieve good polarization matching with spherical waves inside the breast as well as low pulse distortion and low mutual effects between array elements.

Time domain behavior of the conformal antenna has indicated better pulse distortion performance through the breast, comparing with the planar bow-tie. The mutual coupling effects of the conformal antenna have been reduced in overall compared to that of the planar antenna, too. Images of the spherical tumor with 2 mm diameter have been successfully formed by using the DAS algorithm. Tumor responses have been increased in between 2.3 dB and 5.7 dB with the use of the spherical conformal antenna. Obtained simulation results are reasonably reliable and promising; however, experimental work based on microwave radar-based differential imaging technique is required with anatomically realistic breast phantom models.

REFERENCES

- [1] S. Iudicello and F. Bardati, "Functional imaging of compressed breast by microwave radiometry," *Applied Computational Electromagnetics Society (ACES) Journal*, vol. 24, no.1, pp. 64-71, 2009.
- [2] L. Wang, X. Zhao, H. Sun, and G. Ku, "Microwave-induced acoustic imaging for biological tissues," *Rev. Sci. Instrum.*, vol. 70, no. 9, pp. 3744-3748, 1999.
- [3] A. Bulyshev, S. Semenov, A. Souvorov, R. Svenson, A. Nazarov, Y. Sizov, and G. Tatsis "Computational modelling of three-dimensional microwave tomography of breast cancer," *IEEE Trans. Biomed. Eng.*, vol. 48, no. 9, pp. 1053-1056, 2001.
- [4] E. Fear, X. Li, S. Hagness, and M. Stuchly, "Confocal microwave imaging for breast tumor detection: Localization in three dimensions," *IEEE Trans. Antennas Propag.*, vol. 49, no. 8, pp. 812-822, 2002.
- [5] E. J. Bond, X. Li, S. C. Hagness, and B. D. Van Veen, "Microwave imaging via space-time beamforming for early detection of breast cancer," *IEEE Trans. Antennas Propag.*, vol. 51, no.8, pp. 1690-1705, 2003.

- [6] M. Klemm, J. Leendertz, D. Gibbins, I. Craddock, A. Preece, and R. Benjamin, "Microwave radar-based differential breast cancer imaging: Imaging in homogeneous breast phantoms and low contrast scenarios," *IEEE Trans. Antennas Propag.*, vol. 58, pp. 2337-2344, 2010.
- [7] X. Li, S. Davis, S. Hagness, D. Van der Weide, and B. Van Veen, "Microwave imaging via space-time beamforming: Experimental investigation of tumor detection in multilayer breast phantoms," *IEEE Trans. Microw. Theory Tech.*, vol. 52, no. 8, pp. 1856-1865, 2004.
- [8] S. Hagness, A. Taflove, and J. Bridges, "Wideband ultralow reverberation antenna for biological sensing," *Electronics Letters*, vol. 33, no. 19, pp. 1594-1595, 1997.
- [9] X. Yun, E. Fear, and R. Johnston, "Compact antenna for radar-based breast cancer detection," *IEEE Trans. Antennas Propag.*, vol. 53, no. 8, pp. 2374-2380, 2005.
- [10] H. Kanj and M. Popovic, "Two-element T-array for cross-polarized breast tumor detection," *Applied Computational Electromagnetics Society (ACES) Journal*, vol. 23, no. 3, pp. 249-254, 2008.
- [11] N. Tavassolian, S. Nikolaou, and M. Tentzeris, "A flexible UWB elliptical slot antenna with a tuning uneven U-shape stub on LCP for microwave tumor detection," *Asia-Pacific Microwave Conference*, Bangkok, Thailand, pp. 1-4, Dec. 2007.
- [12] D. Gibbins, M. Klemm, I. Craddock, J. Leendertz, A. Preece, and R. Benjamin, "A comparison of a wide-slot and a stacked patch antenna for the purpose of breast cancer detection," *IEEE Trans. Antennas Propag.*, vol. 58, no. 3, pp. 665-674, 2010.
- [13] J. Bourqui, M. Okoniewski, and E. Fear, "Balanced antipodal vivaldi antenna for breast cancer detection," *The Second European Conference on Antennas and Propagation*, Edinburgh, UK, pp. 1-5, Nov. 2007.
- [14] İ. Ünal, B. Türetken, K. Sürmeli, and C. Canbay, "An experimental microwave imaging system for breast tumor detection on layered phantom model," *URSI GASS 2011*, İstanbul, Turkey, pp. 1-4, Aug. 2011.
- [15] B. Mohammed, A. Abbosh, and M. Bialkowski, "Design of tapered slot antenna operating in coupling liquid for ultrawideband microwave imaging systems," *APSURSI*, Washington, USA, pp. 145-148, July 2011.
- [16] Z. Šipuš, S. Škokić, and N. Burum, "Performance analysis of spherical stacked-patch antennas," *18th Int. Conference on Applied Electromagnetics and Communications*, Dubrovnik, Croatia, pp. 1-4, Oct. 2005.
- [17] R. Conceição, M. O'Halloran, M. Glavin, and E. Jones, "Comparison of planar and circular antenna configurations for breast cancer detection using microwave imaging," *Progress In Electromagnetics Research*, PIER 99, pp. 1-20, 2009.
- [18] X. Yun, R. Johnston, and E. Fear, "Radar-based microwave imaging for breast cancer detection: Tumor sensing with cross-polarized reflections," *Antennas and Propagation Society Int. Symposium*, California, USA, pp. 2432-2435, June 2004.
- [19] J. Stang, W. Joines, Q. Liu, G. Ybarra, R. George, M. Yuan, and I. Leonhardt, "A tapered microstrip patch antenna array for use in breast cancer screening via 3D active microwave imaging," *Antennas and Propagation Society Int. Symposium*, Charleston, SC, USA, pp. 1-4, June 2009.
- [20] İ. Ünal, B. Türetken, U. Buluş, and C. Canbay, "Analysis of the electromagnetic field scattered by a spherical breast tumour model," *URSI-EMTS 2013*, Hiroshima, Japan, pp. 574-577, May 2013.
- [21] İ. Ünal, *A New Ultrawide-Band (UWB) Microwave Imaging System with Minimized Mutual Coupling Effects for Breast Tumor Detection*, Ph.D. Thesis, Yeditepe University, Department of Electrical and Electronics Engineering, İstanbul, Turkey, March 2013.
- [22] N. Tavassolian, H. Kanj, and M. Popović, "The effect of breast glands on microwave tumor sensing with "Dark Eyes" antenna," *Antennas and Propagation Society Int. Symposium*, Albuquerque, NM, USA, pp. 291-294, July 2006.
- [23] İ. Ünal, B. Türetken, U. Buluş, and C. Canbay, "Analysis of dispersive effects of breast phantom model on ultra wideband microwave imaging of breast cancer tumor," *IASTED International Conference on Biomedical Engineering*, Innsbruck, Austria, pp. 1-6, Feb. 2013.
- [24] C. Canbay, *Antennas and Propagation I*, Yeditepe University Press, İstanbul, 1997.
- [25] A. Abbosh and M. Bialkowski, "Compact directional antenna for ultra wideband microwave imaging systems," *Antennas and Propagation Society Int. Symposium*, Charleston, SC, USA, pp. 1-4, June 2009.
- [26] Rohde & Schwarz GmbH & Co. KG, ZNB 8 Vector Network Analyzer, Product Data Sheet.
- [27] M. Lazebnik, M. Okoniewski, J. Booske, and S. Hagness, "Highly accurate debye models for normal and malignant breast tissue dielectric properties at microwave frequencies," *IEEE Microwave and Wireless Components Letters*, vol. 17, no. 12, pp. 822-824, 2007.
- [28] D. Winters, J. Shea, P. Kosmas, B. Van Veen, and S. Hagness, "Three-dimensional microwave breast imaging: Dispersive dielectric properties

estimation using patient-specific basis functions,” *IEEE Trans. Medical Imag.*, vol. 28, no. 7, pp. 969-981, 2009.

- [29] A. Capozzoli, C. Curcio, A. Di Vico, and A. Liseno, “NUFFT- & GPU-based fast imaging of vegetation,” *IEICE Trans. Commun.*, vol. E94-B, no. 7, pp. 2092-2103, 2011.



İlhami Ünal received his B.Sc., M.Sc., and Ph.D. degrees from Yeditepe University, Istanbul, Turkey in 2002, 2005 and 2013, respectively, in Electrical and Electronics Engineering. Since Sept. 2013, he has been working as a chief senior researcher at Millimeter and Terahertz Technologies Research Laboratories (MILTAL) at the Material Institute of TUBITAK-MRC. His research interests include antennas and propagation, scattering of electromagnetic fields, microwave imaging and bioelectromagnetics. He is also the Associate Editor of the Turkish Journal of Electrical & Computer Sciences.



Bahattin Türetken has received M.Sc. and Ph.D. degrees from Istanbul Technical University, Istanbul, Turkey in 1998 and 2002, respectively. He received Associate Professor title in 2008. He has been working as chief researcher at TUBITAK-UEKAE (National Research Institute of Electronics and Cryptology) EMC & TEMPEST Test Center. He managed Electromagnetic and Research Group (EMARG) and the project of Antenna Test and Research Center between 2009 and 2012. He has been the director of “Millimeter and Terahertz Technologies Research Laboratories (MILTAL)” since 2012. He was awarded “Young Scientist Award” by URSI in 1999 and “Young Scientist Paper” by MMET in 2000. His research topics are radar, antenna design and testing, computational electromagnetic, diffraction & scattering EM Problems, civilian and military EMC/EMI problems, terahertz applications, radiometry, biomedical Imaging, implant devices.



Cahit Canbay received the B.Sc. degree from Physics Department of Istanbul University, Turkey. He received his Ph.D. degree in Electronics and Communications Engineering from Yıldız Technical University, Turkey. His research interests include electromagnetic fields, antennas and propagation, biological effects of electromagnetic fields on human health, optical fiber systems and their problems, optoelectronics, smart antennas and propagation for wireless systems, numerical methods in electromagnetic problems and electromagnetic compatibility.

A CPW-Fed Band-Notched UWB Antenna with T-shape Construct and Matching Branches

A. Chen¹, C. Yang¹, Z. Chen², K. AN¹, J. Fang¹, and W. Jiang¹

¹School of Electronic and Information Engineering
Beihang University, Beijing 100191, China
axchen@buaa.edu.cn, ych1987520@163.com, annking1986@163.com, fangjian2006@yahoo.cn,
jiangweiwei1969@126.com

²Department of Electrical and Computer Engineering
Dalhousie University, Halifax, NS B3J 2X4, Canada
z.chen@dal.ca

Abstract — A compact coplanar waveguide (CPW) fed ultra-wideband (UWB) antenna with a band-notched performance is presented in this paper. The band-notched UWB antenna is designed on a $26 \times 34 \times 1.6$ mm³ substrate. It consists of a circle ring with a T-shape construct, three rectangular matching branches, a rectangular transition branch, and a CPW feed line. The antenna is simulated and the geometrical parameters of the antenna selected with Ansoft HFSS. The simulated results show the impedance bandwidth covers from 3.0 GHz to 11.0 GHz with the notched rejection band of 5.1 GHz - 5.8 GHz. A prototype was fabricated and tested. The measured and simulated results show that the proposed antenna gives bidirectional radiation pattern in the E-plane and omnidirectional radiation pattern in the H-plane with relatively flat gains in the pass-band. Due to its compact configuration, the antenna can find good UWB applications.

Index Terms - Antenna, band notching, coplanar waveguide (CPW), impedance matching, and ultra-wideband (UWB).

I. INTRODUCTION

In February 2002, the Federal Communication Commission (FCC) allocated a frequency band 3.1 GHz-10.6 GHz for ultra-wideband (UWB) applications [1]. Since then, designs of the ultra-wideband (UWB) wireless systems have garnered

great attention. The UWB systems have many advantages, such as excellent immunity to multipath interference, large bandwidth and high speed data rate. One of the most important components in an UWB wireless system is the antenna. Designing such an antenna faces many challenges, because the antenna has to have the special properties such as omni-directional pattern, ultra-wideband impedance bandwidth, constant gain, low profile, and easiness for manufacture [2].

Many antennas have been explored and developed for UWB wireless systems, such as monopole patch antenna [3], slot antenna [4], and fractal antenna [5]. By using optimization method, good characteristics of radiation, transmission, and impedance bandwidth can be achieved [6].

Many existing wireless communication and radio systems operate in a frequency band that overlaps with the UWB band, such as IEEE 802.11a in USA (5.15 GHz-5.35 GHz and 5.725 GHz-5.825 GHz), HIPERLAN/2 in Europe (5.15 GHz-5.35 GHz and 5.47 GHz -5.725 GHz) [7]. As a result, an existing system should not cause any interference to an UWB system and vice versa. One of the approaches to achieve the objective is to embed filters into UWB circuits, but it will increase the UWB system complexities. A much better way is to design UWB antennas with band-notched characteristics. To this end, many band-notched antennas have been designed and developed.

Among the band-notched UWB antennas reported so far, the most popular are those with resonance structures added on radiators or feeding structures; they include U-shape slots [8-11], T-shape construct [12-14], π -shape strip [13], SRR and CSRR structures [15], stepped impedance stub [16]. All of them can have good performance in rejection or notched bands, and some of them even have multiple notched bands [8-10, 15-17].

On the other hand, planar monopole antennas have many advantages for UWB applications because of their compact size and stable radiation [18]. An UWB antenna fed by a coplanar waveguide (CPW) has the properties of low profile, wide bandwidth, low loss, and easy integration with electronic circuits; therefore, it is widely used in communication systems.

In this paper, a planar monopole band-notched UWB antenna fed by CPW is proposed. The band-notched characteristic is achieved by embedding a T-shape structure in the antenna's radiator and using three matching branches to adjust high frequency characteristic of the antenna.

The remainder of the paper is organized as follows. First, the geometry of the proposed antenna is described in section II. Analysis and simulation of the effects of the antenna parameters on impedance bandwidth are presented in section III. After that, the experimental results are presented to compare with the simulation results in section IV. Finally, in section V, conclusions are drawn.

II. THE PROPOSED ANTENNA

Figure 1 shows the geometry of the proposed antenna with a band-notched characteristic. The antenna is symmetrical about the x -axis. It consists of a circle ring radiation patch, three rectangular matching branches, a rectangular transition branch and a CPW. The band rejection characteristic is mainly achieved by embedding a T-shape construct in the circle ring radiation patch. The width of the T-shape construct is W_5 and W_6 . The length is L_5 and L_6 . The width and length of the two matching branches on the left side and on the top side are W_2 and L_2 , W_4 and L_4 , respectively. The thickness of the antenna is h . The physical dimensions of the antenna are shown in Table I.

III. ANTENNA DESIGN AND ANALYSIS

In this section, analysis and simulation results

are presented. The Ansoft HFSS was used to carry out all the simulations.

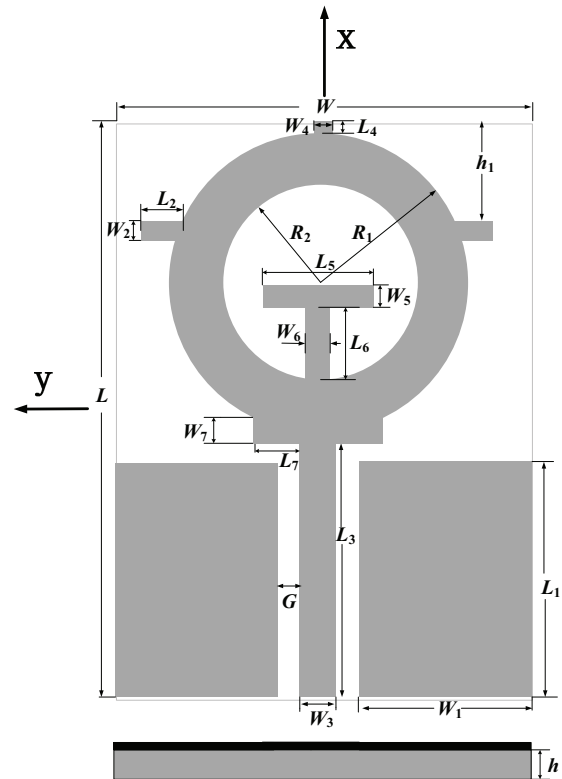


Fig. 1. Geometry of the proposed antenna.

Table I: Physical dimensions of the proposed UWB antenna (unit: millimeters).

Parameter	Value	Parameter	Value
L	34.00	W	26.00
L_1	13.46	W_1	11.15
L_2	3.31	W_2	1.00
L_3	14.55	W_3	2.00
L_4	0.58	W_4	1.00
L_5	5.00	W_5	0.50
L_6	3.54	W_6	0.50
L_7	3.00	W_7	0.82
h	1.60	h_1	6.00
R_1	9.50	R_2	5.91
G	0.85		

In the proposed antenna, the circular ring patch and the T-shape construct are equivalent to an inductor and a capacitor. The T-shape construct as a band-notched structure was analyzed in [12, 13]. At the resonant frequency, the construct can cause an impedance change that leads to

impedance mismatching near the notched band. The matching branches and the circle ring are then introduced to compensate for the change as well as to adjust the width of the notched band. As a result, L_5 , L_6 , R_2 , and L_2 are considered as main design variables that determine the performances of the antenna.

In general, the T-shape construct mainly affect the notched band, and have a slight influence on the pass band. Considering possible coupling between the T-shape construct and the circle ring patch, length L_5 and L_6 should not be too large. Because the length of the T-shape is measured collectively by L_5 and L_6 , $L_5 + L_6$ is chosen as the analysis parameter. Figure 2 shows the simulated VSWR with various lengths of the T-shape construct. It is clearly seen from the figure that length $L_5 + L_6$ has a significant effect on the notched frequency. The rejection or notched frequency band shifts from around 5.6 GHz to 4.3 GHz when the length $L_5 + L_6$ increases from 7.9 mm to 9.9 mm, while the pass band is only affected slightly.

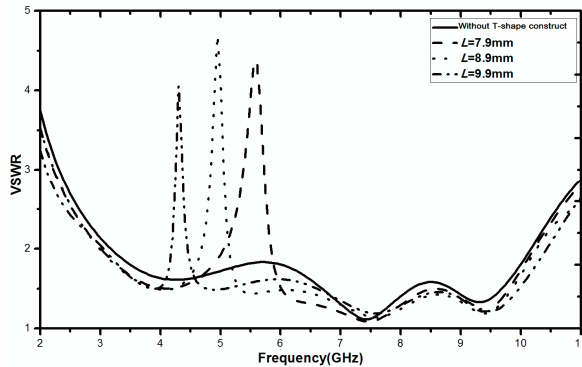


Fig. 2. Simulated frequency response of VSWRs with various $L_5 + L_6$.

Figure 3 shows the variations of the notched band with respect to R_2 . It is obvious that the longer R_2 , the wider notched bandwidth. VSWR increases from 4.3 to 8.0 as R_2 increases from 5.2 mm to 7.2 mm, while the notched frequency only decreases slightly with the R_2 .

Figure 4 shows the simulated VSWRs with L_2 varying from 1.9 mm to 3.5 mm. It can be seen that the upper-end frequency decreases as L_2 increases. When L_2 changes from 1.9 mm to 3.5 mm, the upper frequency decreases to 10.5 GHz, while the lower frequency hardly changes. This is

because increasing the branches L_2 is equal to increasing the equivalent current length and decrease the resonant frequency [13]. After a detailed simulation analysis, the physical parameters are set as shown in Table I.

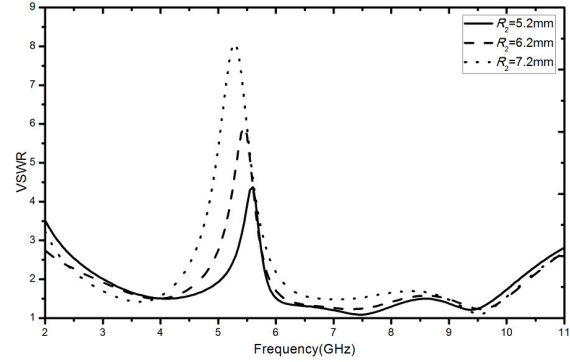


Fig. 3. Simulated frequency response of VSWRs with various R_2 .

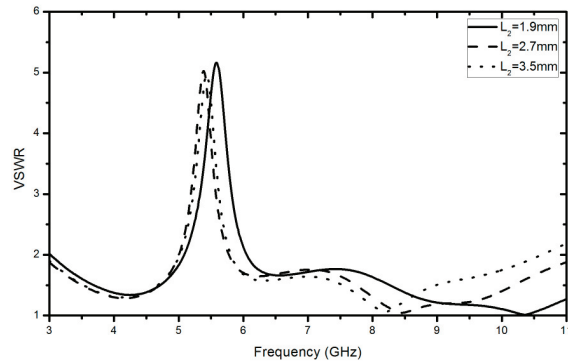


Fig. 4. Simulated frequency response of VSWRs with various L_2 .

IV. EXPERIMENTAL RESULTS

The proposed antenna was fabricated and tested. Its photographs are shown in Fig. 5. The dielectric substrate used in the antenna was FR-4 with dielectric constant of 4.4, loss tangent of 0.02, and substrate thickness of 1.6 mm. SMA connector was used for transition between the CPW and coaxial cable for the measurement purpose.

VSWR was measured using Agilent E8362B PNA. The measured and simulated VSWRs are shown in Fig. 6. It can be seen that the simulated VSWR is less than 2.0 from 3.0 GHz to 11 GHz with a notched rejection band of 5.1 GHz-5.8 GHz, while the measured antenna bandwidth covers the

range of 3.5 GHz - 10.6 GHz with a notched rejection band of 4.8 GHz - 5.8 GHz. The discrepancy between the simulated and measured VSWR can be attributed to fabrication errors and differences between the electrical properties used in the simulations and those of the actual materials.

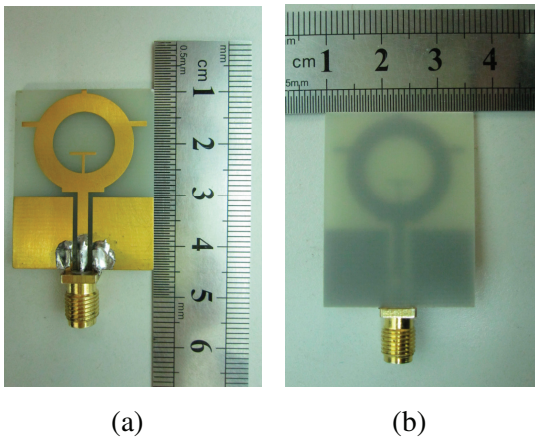


Fig. 5. Photographs of the proposed antenna; (a) front view and (b) rear view.

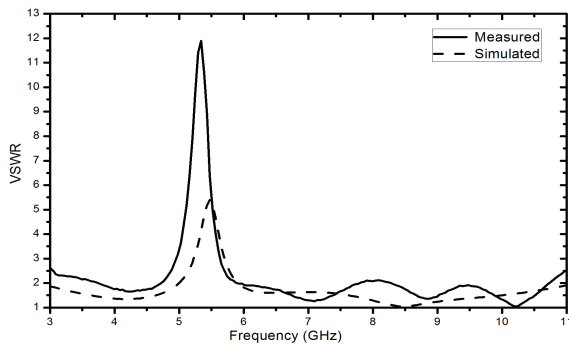
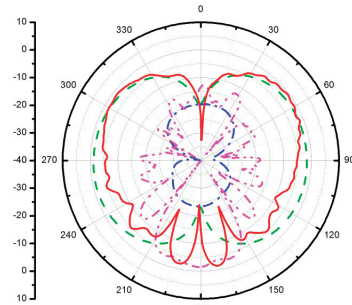


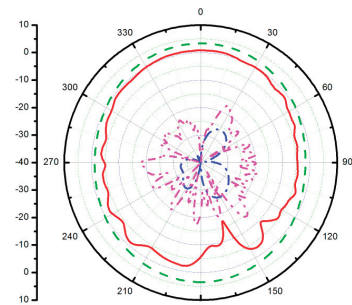
Fig. 6. Measured and simulated VSWR.

Figure 7 shows the far-field radiation patterns of the E-plane and H-plane at 5 GHz, 5.4 GHz, 6 GHz, and 7 GHz, respectively. 5.4 GHz is within the notched band. It can be seen that the patterns of the antenna at these frequencies are roughly omnidirectional in the H-plane. In the E-plane, they remain roughly bidirectional patterns. Figure 7 (b) indicates that the antenna has much lower gains in the notched band than those at other passband frequencies. The cross-polarization in the negative x -direction is much higher than that in other directions, which could be mainly due to the

SMA connector that alters the distribution of the current.

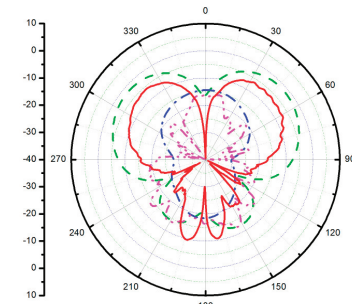


E-plane

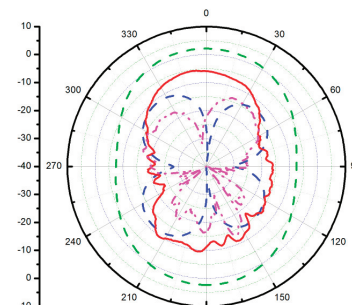


H-plane

(a)



E-plane



H-plane

(b)

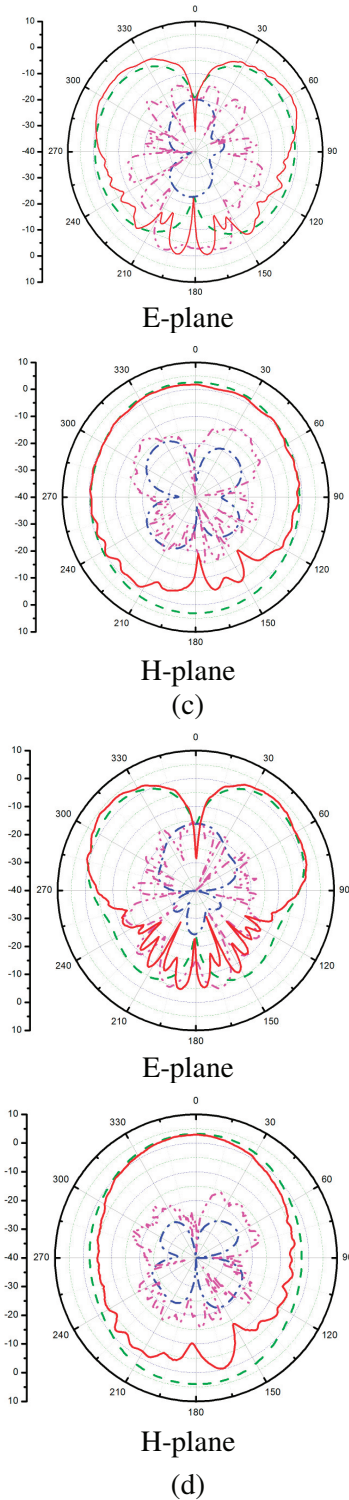


Fig. 7. Measured and simulated radiation patterns of the proposed antenna at (a) 5 GHz, (b) 5.4 GHz, (c) 6 GHz, and (d) 7 GHz (— Measured Co-polarization; - - - Simulated Co-polarization; ····· Measured Cross-polarization; - · - · Simulated Cross-polarization).

Figure 8 shows the measured and simulated gains of the proposed antenna from 3 GHz to 11 GHz. The figure indicates that the proposed antenna has good gain flatness except that in the notched band. Sharp gain decreases occur in the vicinity of 5.4 GHz, thus clearly indicating the band-notched effect of the T-shape construct.

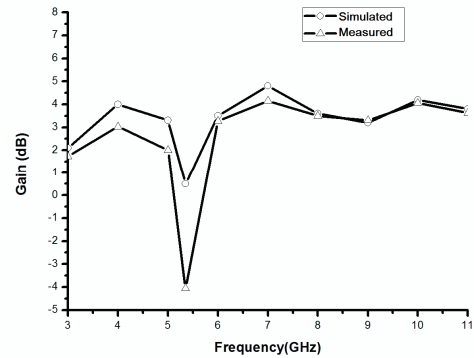


Fig. 8. The measured and simulated gains of the proposed antenna.

V. CONCLUSION

In this paper, a CPW-fed band-notched UWB antenna is presented. The circle ring radiation patch is used to give a wide bandwidth for UWB applications while three rectangular branches are employed to improve impedance conditions at high frequencies. The notched band, covering the WLAN band, is achieved by a T-shaped construct embedded inside the circle ring patch. The measured VSWR shows that the proposed antenna achieves a bandwidth ranging from 3.5 GHz-10.6 GHz with the notched band of 4.8 GHz-5.8 GHz. The proposed antenna has simple structure and presents omnidirectional patterns across the whole operating band in H-plane. The antenna has a compact size of $26 \times 34 \times 1.6 \text{ mm}^3$. Measurement results show that the antenna is suitable for UWB applications.

ACKNOWLEDGMENT

This work was supported in part by the National Science Foundation of China under Grant 61371006 and NSAF under Grant 11076031.

REFERENCES

- [1] First Report and Order, "Revision of Part 15 of the Commission's Rule Regarding Ultra-Wideband

- Transmission systems FCC 02-48," Federal Communication Commission, 2002.
- [2] M. Ghavami, L. Michael, and R. Kohno, *IEEE Ultra Wideband Signals and Systems in Communication Engineering*, New York: John Wiley and Sons, USA, 2004.
- [3] K. Lau, P. Li, and K. Man, "A monopolar patch antenna with very wide impedance bandwidth," *IEEE Trans. Antennas Propag.*, vol. 53, no. 3, pp. 1004-1010, Mar. 2005.
- [4] T. Ma and S. Jeng, "Planar miniature tapered-slot-fed annular slot antennas for ultrawide-band radios," *IEEE Trans. Antennas Propag.*, vol. 53, no. 3, pp. 1194-1202, Mar. 2005.
- [5] H. Oraizi and S. Hedayti, "Miniaturized UWB monopole microstrip antenna design by the combination of Giuseppe Peano and Sierpinski Carpet fractals," *IEEE Antennas Wireless Propag. Lett.*, vol. 10, pp. 67-70, 2011.
- [6] W. Weng, "Optimal design of an ultra-wideband antenna with the irregular shape on radiator using particle swarm optimization," *Applied Computational Electromagnetics Society Journal*, vol. 27, no. 5, pp. 427-434, May 2012.
- [7] H. Schantz, G. Wolynec, and E. Myszka, "Frequency notched UWB antennas," *Ultra Wideband Systems and Technologies*, pp. 214-218, 2003.
- [8] C. Yu, W. Hong, L. Chiu, G. Zhai, C. Yu, W. Qin, and Z. Kuai, "Ultra wideband printed log-periodic dipole antenna with multiple notched bands," *IEEE Trans. Antennas Propag.*, vol. 59, no. 3, pp. 725-732, Mar. 2011.
- [9] C. Li and L. Ye, "Improved dual band-notched UWB slot antenna with controllable notched bandwidths," *Progress In Electromagnetics Research*, vol. 115, pp. 477-493, 2011.
- [10] M. Xie, Q. Guo, and Y. Wu, "Design of a miniaturized UWB antenna with band-notched and high frequency rejection capability," *J. of Electromagn. Wave and Appl.*, vol. 25, pp. 1103-1112, 2011.
- [11] J. William and R. Nakkeeran, "A new UWB slot antenna with rejection of WiMax and WLAN bands," *Applied Computational Electromagnetics Society Journal*, vol. 25, no. 9, pp. 787-793, Sept. 2010.
- [12] C. Hong, C. Ling, I. Tarn, and S. Chung, "Design of a planar ultra wideband antenna with a new-notch structure," *IEEE Trans. Antennas Propag.*, vol. 55, no. 12, pp. 3391-3397, Dec. 2007.
- [13] M. Ojaroudi, Sh. Yazdanifard, N. Ojaroudi, and R. Sadeghzadeh, "Band-notched small square-ring antenna with a pair of T-shaped strips protruded inside the square ring for UWB applications," *IEEE Antennas Wireless Propag. Lett.*, vol. 10, pp. 227-230, 2011.
- [14] M. Ojaroudi, N. Ojaroudi, and Y. Ebazadeh, "Dual Band-notch small square monopole antenna with enhanced bandwidth characteristics for UWB applications," *Applied Computational Electromagnetics Society Journal*, vol. 27, no. 5, pp. 420-426, May 2012.
- [15] D. Kim, N. Jo, H. Jang, and C. Kim, "Design of the ultra wideband antenna with a quadruple-band rejection characteristics using a combination of the complementary split ring resonators," *Progress In Electromagnetics Research*, vol. 112, pp. 93-107, 2011.
- [16] Y. Li, W. Li, and W. Yu, "A switchable UWB slot antenna using SIS-HSIR and SIS-SIR for multi-mode wireless communications applications," *Applied Computational Electromagnetics Society Journal*, vol. 27, no. 4, pp. 340-351, Apr. 2012.
- [17] W. Li, X. Shi, and Y. Hei, "Novel planar UWB monopole antenna with triple band-notched characteristics," *IEEE Antennas Wireless Propag. Lett.*, vol. 8, pp. 1094-1098, 2009.
- [18] Tz. Ma and S. Wu, "Ultrawideband band-notched folded strip monopole antenna," *IEEE Trans. Antennas Propag.*, vol. 55, no. 9, pp. 2473-2479, Sept. 2007.

Modal Analysis for a Waveguide of Nanorods Using the Field Computation for a Chain of Finite Length

Y. Rahbarihagh, F. Kalhor, J. Rashed-Mohassel, and M. Shahabadi

Photonics Research Lab, Center of Excellence on Applied Electromagnetic Systems, School of ECE, College of Engineering, University of Tehran, North Kargar Ave, Tehran, Iran
yrahbari@ut.ac.ir, f.kalhor@ut.ac.ir, jrashed@ut.ac.ir, shahabad@ut.ac.ir

Abstract — The propagation of light along an infinite 2D chain of silver nanorods is analyzed and the dispersion for this waveguide is computed using field computation for a finite chain of nanorods. In this work, generalized multipole technique is used for the analysis. This method calculates the imaginary and real parts of the propagation constant by exciting the chain in one end and observing propagation of modes along the chain far enough from the excitation. It is shown that a short chain of finite length is sufficient for the calculation of the phase constant while the attenuation constant requires a longer chain. Field distribution is depicted for even and odd modes and it is shown that in the simulated frequency range only two modes can be excited and can propagate along the waveguide.

Index Terms — Generalized multipole technique, Modal analysis, surface plasmon polariton, and waveguide.

I. INTRODUCTION

The ability of confining electromagnetic fields below the diffraction limit has made plasmonic waveguides a promising candidate for integrated optics. After Takahara et al. [1] demonstrated the possibility of guiding electromagnetic energy below the diffraction limit, various structures have been proposed as plasmonic waveguides. Quinten et al. [2] were the first to introduce a chain of metallic nanoparticles as a waveguide. Since then, this waveguide has been studied in many researches [3-15].

Several computational methods have been used for the analysis of nanoparticle-chain

waveguides. Dipole approximation (DA), finite-element method (FEM), and finite-difference time-domain (FDTD) are commonly used methods. Dipole approximation is easy to implement and accurate for structures in which spacing of nanoparticles is significantly larger than particle dimensions. This method cannot be used for structures in which $L / r < 3$, where L is the separation between particles and r is the radius of the particle [16, 17]. Moreover, for particles of an arbitrary shape, calculation of polarizability demands additional numerical efforts. Improvements to DA like considering retardation effect [18], quadrupole, and higher-order multipoles effect [16, 19] and adding the effect of layered background [20-22] have been proposed, yet it is not commonly used for a waveguide comprising arbitrary shaped nanoparticles with small inter-particle distance. FDTD and FEM are also common tools for analyzing plasmonic waveguides [4, 23]. However, in plasmonic structures, at frequencies near the plasma resonant frequency, electromagnetic (EM) fields are mainly confined around particles. Therefore, for domain discretization methods, such as FDTD and FEM, a very fine mesh is needed to achieve acceptable accuracy. A comparison between domain discretization and boundary discretization methods can be found in [24]. According to [24], boundary discretization methods show higher precision and are less time consuming for 2D plasmonic structures.

Generalized multipole technique (GMT) is a boundary discretization method, which has already been used for the modal analysis of nanoparticle-chain waveguides [8, 11]. This method is applicable to structures with $L / r < 3$. Also, GMT

is capable of analysis of a waveguide comprising arbitrary shaped nanoparticles. Nevertheless, GMT works with smaller matrices, which leads to less physical memory consumption compared with the domain discretization methods. Dispersion diagram for a 2D and 3D waveguide of nanoparticles is calculated in [8, 11] using GMT. In these researches, the propagation constant is calculated by finding the extrema of a cost function, like error or field intensity. Finding extrema of this function requires calculation of the cost function at different frequencies, which can be time consuming. However, the extrema of the function can be affected by changes in the field distribution of the modes or coupling among modes for different frequencies. Moreover, finding the attenuation constant needs extra calculation.

An improved modal analysis is presented in this work. The EM field distribution in a finite chain of nanorods is analyzed and the complex wavenumber using the complex value of the EM field at certain sampling points is calculated. The propagation of the EM field in a finite chain of nanorods is computed using GMT formulation.

II. GENERALIZED MULTIPOLE TECHNIQUE FORMULATION FOR 2D NANOSTRUCTURES

Generalized multipole technique is a frequency-domain method for solving Maxwell's equations after subdividing the solution domain into homogeneous subdomains [25]. The EM field in each subdomain is expanded in terms of the EM field generated by a number of multipoles placed outside the subdomain. The unknown amplitude of

the multipoles are calculated satisfying boundary conditions with minimum error.

For a two-dimensional z-invariant problem, the z-components of the electric and magnetic field at a given point \vec{r} generated by N_l clusters of multipoles can be expanded as,

$$E_z(\vec{r}) = \sum_{l=1}^{N_l} \sum_{n=-N}^N \frac{k^2 C_{ln}}{j\omega\epsilon} H_n^{(2)}(k|\vec{r}_l|) e^{jn\varphi_l}, \quad (1a)$$

$$H_z(\vec{r}) = \sum_{l=1}^{N_l} \sum_{n=-N}^N \frac{k^2 D_{ln}}{j\omega\mu} H_n^{(2)}(k|\vec{r}_l|) e^{jn\varphi_l}, \quad (1b)$$

in which the l -th cluster containing N multipoles is located at \vec{r}_l . The coefficients C_{ln} and D_{ln} are the amplitudes of TE_z and TM_z multipoles, respectively, k is the wave-number of the subdomain in question and φ_l is the angle at which location \vec{r} is seen by the multipoles placed at \vec{r}_l . There are a total of $2N_l(2N+1)$ multipoles.

In a finite chain composed of m nanorods, as shown in Fig. 1, there are $m+1$ subdomains. For each subdomain, the z-components of the EM field can be expanded using equations (1a) and (1b) with clusters placed outside of the subdomain. Fields of the subdomain D_1 are expanded by all the clusters represented by (+) and fields inside each nanorod are expanded by a set of clusters placed around it. Excitations can be placed at arbitrary positions and are represented by (*).

Matching of the tangential field components on the boundaries is ensured by means of generalized point matching (GPM). Matching tangential magnetic and electric fields at matching points leads to the following system of equations,

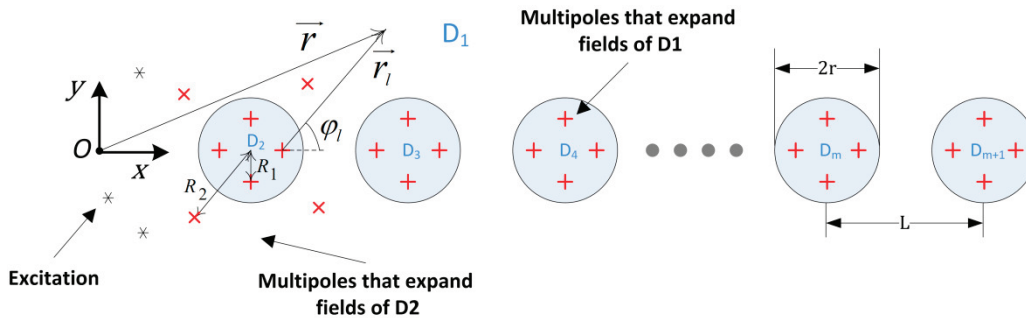


Fig. 1. Schematic of a finite chain containing m nanoparticles.

$$[A]_1 \begin{bmatrix} C \\ D \end{bmatrix}_1 + [B]_{exc} = \begin{bmatrix} [A]_2 & 0 & \dots & 0 \\ 0 & [A]_3 & \dots & 0 \\ \vdots & \vdots & \ddots & \vdots \\ 0 & 0 & \dots & [A]_{m+1} \end{bmatrix} \begin{bmatrix} \begin{bmatrix} C \\ D \end{bmatrix}_2 \\ \begin{bmatrix} C \\ D \end{bmatrix}_3 \\ \vdots \\ \begin{bmatrix} C \\ D \end{bmatrix}_{m+1} \end{bmatrix}, \quad (2)$$

where $\begin{bmatrix} C \\ D \end{bmatrix}_i$ are the unknown amplitudes of the multipoles expanding the EM field in the i -th subdomain, $[B]_{exc}$ is the tangential excitation fields at the matching points with the excitation placed in the first subdomain at (*) locations in Fig. 1 and the matrices $[A]_i$ relate the unknown coefficients to the tangential fields at the matching points of the i -th subdomain.

Equation 2 presents an over-specified system.

It can be reshaped to yield $[A] \begin{bmatrix} C \\ D \end{bmatrix} = [B]$, which may not have an exact solution. This equation is solved after computation of the pseudo-inverse of the $[A]$ matrix, which minimizes the error defined by,

$$Error = \frac{\left\| [A] \begin{bmatrix} C \\ D \end{bmatrix} - [B] \right\|}{\|[B]\|}. \quad (3)$$

III. MODAL ANALYSIS

In general, a metallic nanorod waveguide has various modes with different propagation constants. By its arbitrary excitation, a group of waveguide modes are excited and will propagate along the nanorods. If there is a dominant mode at each given frequency, other modes are attenuated according to a larger attenuation constant. Hence, by moving away from the excitation point, the amplitudes of the non-dominant modes decay faster than the amplitude of the dominant mode.

In a periodic structure for which only one mode propagates along the x -direction, the mode fields satisfy the Bloch condition,

$$\vec{f}(x+L, y) = \vec{f}(x, y)e^{-jkL}, \quad (4)$$

where \vec{f} denotes the electric or magnetic field, x represents the propagation direction, L is the period of the structure, and $k = (\beta - j\alpha)$ is the propagation constant. In principle, by sampling the function \vec{f} at various x , values one can determine the propagation constant, k .

For a finite but long waveguide and far from the excitation end, one may assume single-mode propagation of the dominant mode. Taking both the forward and backward propagating dominant mode into account, we may express $\vec{f}(x, y)$ as,

$$\vec{f}(x, y) = (Ae^{-jkx} + Be^{jkx})\vec{u}(x, y), \quad (5)$$

where \vec{u} is a periodic function in x , A , and B represent the amplitudes of the forward and backward propagating dominant mode, respectively. To determine A , B , and k , the total field must be sampled at least at three different locations. As a result of which, a system of three complex equations is obtained. Note that the three sampling points have a spacing of L in the x -direction and have identical y -values, so the function $\vec{u}(x, y)$ has no influence on determination of the unknowns A , B , and k . Note that depending on the polarization of the excitation field, TE_z or TM_z modes are excited. Therefore, the function \vec{f} is given either by equation (1a) or (1b).

For a symmetric waveguide with respect to the propagation direction, i.e., the x -direction, modes can be classified as even or odd in terms of the electric or magnetic field component. If the waveguide is excited with even (odd) excitation, only even (odd) modes will be present along the finite chain. Thus, using an appropriate excitation, even (odd) dominant mode can be characterized.

Furthermore, taking symmetry along the x and y -axis into consideration, we decrease the number of unknown coefficients and thus the boundary points.

Figure 2 shows a finite chain excited symmetrically. MN represents the symmetry plane of the structure. Because of this symmetry, it will be adequate to solve Maxwell's equations only in one half of the structure. Other advantage of a symmetric excitation is that the amplitudes of forward and backward modes have to be equal in

the middle of the structure. This eliminates one equation and one unknown coefficient.

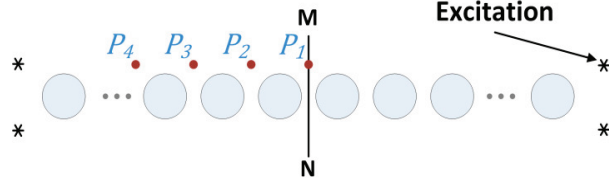


Fig. 2. A finite chain excited symmetrically.

There are two ways to verify the single-mode approximation discussed above. First, one can compare the field of the calculated mode and the total field at other points. Second, one can consider two existing modes in the waveguide. If the amplitude of the second mode is negligible compared to the first one, then the single-mode approximation leads to appropriate results. The following system of equations must be solved if two modes are propagating along the waveguide,

$$\begin{aligned} f_{P_1} &= 2A + 2B, \\ f_{P_2} &= A(e^{-jk_1L} + e^{jk_1L}) + B(e^{-jk_2L} + e^{jk_2L}), \\ f_{P_3} &= A(e^{-j2k_1L} + e^{j2k_1L}) + B(e^{-j2k_2L} + e^{j2k_2L}), \\ f_{P_4} &= A(e^{-j3k_1L} + e^{j3k_1L}) + B(e^{-j3k_2L} + e^{j3k_2L}), \end{aligned} \quad (6)$$

where A and B are the amplitude of the first and second modes in the middle of the chain, respectively, whereas k_1 and k_2 are the propagation constants of these modes. The points P_1 , P_2 , P_3 , and P_4 are shown in Fig. 2.

IV. CONVERGENCE

Before we present the numerical results, we must investigate the convergence of our method. Convergence of wavenumber can be checked with respect to the defined error (equation (3)) and the number of nanorods of the chain. Existence of a propagating mode, in a given frequency, is an essential prerequisite for convergence of the wavenumber. The next section shows (Fig. 6) in the simulated waveguide modes propagated in the $0.1 < L/\lambda < 0.13$ frequency range. Hence, we investigate the convergence in this frequency range.

Figure 3 shows convergence of the computed wavenumber with respect to error. As shown in Fig. 3 (a), increasing the number of unknown coefficients decreases error. As error decreases, the propagation constant converges to its actual value (Fig. 3 (b)). Increasing the number of unknown coefficients increases computational cost and time exponentially. Hence, a compromise should be made between accuracy and computational time.

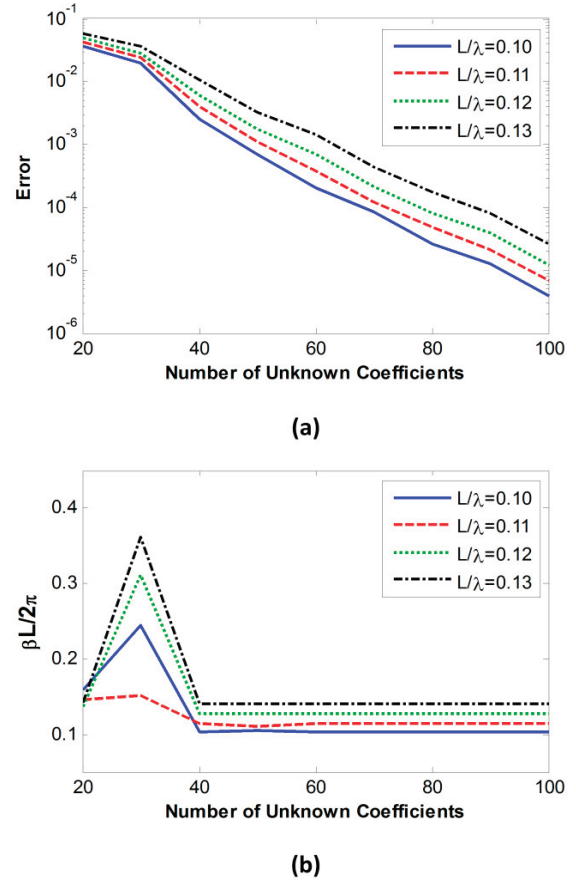


Fig. 3. Convergence of the wavenumber with respect to the number of unknown coefficients.

The second factor affecting convergence of the wavenumber is the number of nanorods in the chain. Increasing the chain length reduces the unwanted effects of the source and the non-dominant modes. Figure 4 shows effects of the chain length on β and α . It shows that β converges for a shorter chain whereas this is not the case for α . It should be noted that the convergence at higher frequencies is faster.

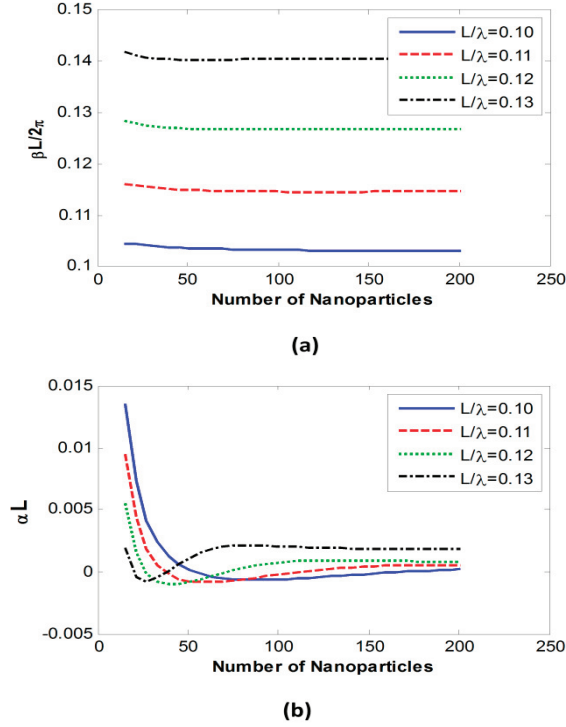


Fig. 4. Convergence of the wavenumber with respect to the number of nanorods. The geometrical and electrical parameters used for obtaining these diagrams are given in section V.

V. RESULTS

Using the method explained above, propagation of the EM field is calculated for a

waveguide of nanorods. The waveguide comprises 100 silver nanorods with $r = 25 \text{ nm}$ and $d = 55 \text{ nm}$ (Fig. 1). Experimental data of [26] are used for the electrical permittivity of silver. The EM fields of both inside and outside of nanorods are expanded using six clusters of multipoles ($N_l = 6$) with $N = 2$ for even modes and nine clusters of multipoles ($N_l = 9$) with $N = 6$ for odd modes. The clusters of multipoles, which expand the EM field outside and inside of the rods are placed at $R_1 = r/4$ and $R_2 = 2r$, respectively. This set of order and location of the multipoles leads to an error of less than 0.7 % in the entire frequency range.

A typical EM field calculation showing propagation of the EM field along the chain is illustrated in Fig. 5. The inset of the Fig. 5 shows the amplitude of the magnetic field generated by the sources in free space. Note that an array with a null in the x -direction is used for the excitation of TE modes. Figure 5 shows the propagation of the EM field along the chain for the same excitation. This figure clearly shows that the EM field is guided along the chain.

In order to calculate the dispersion diagram, the waveguide is stimulated by two sets of excitations; even excitation, which only generates longitudinal modes and odd excitation for generating transverse modes. Figure 6 shows the normalized amplitudes, $|A_e|, |A_o|$, of the dominant

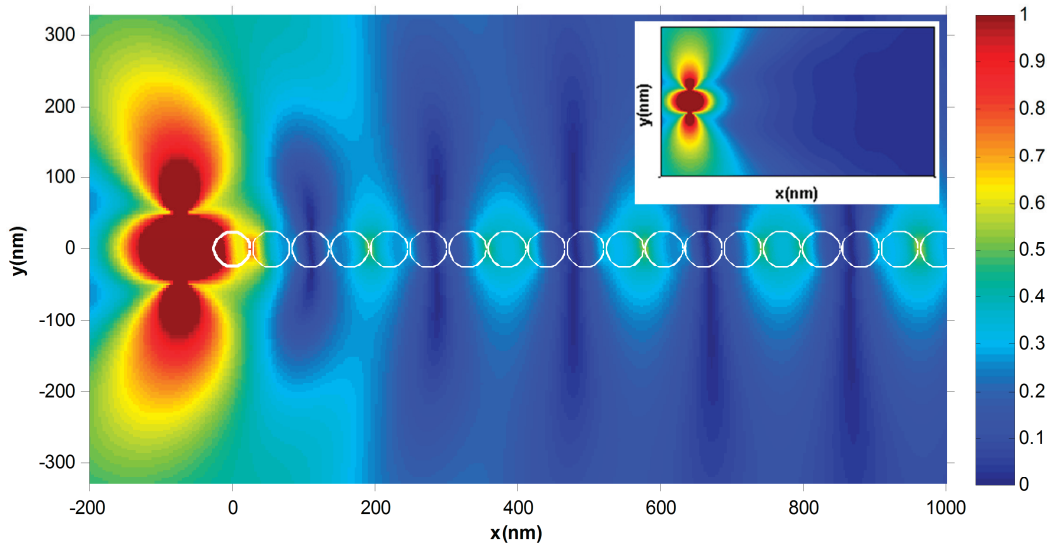


Fig. 5. Propagation of the EM field along the chain. This figure shows the normalized amplitude of the magnetic field for an even excitation. The inset shows the magnetic field of the sources in free space.

mode for even (longitudinal) and odd (transverse) modes, respectively. As is shown in Fig. 6 (a), the even mode propagates along the chain in normalized frequencies below 0.145. In this figure, solid and dash lines show the amplitudes of the first ($|A|$) and the second ($|B|$) modes of equation (6), respectively. As the amplitude of the second mode is negligible in comparison with the first one, the single-mode approximation is acceptable in the normalized frequency range $0.06 < L/\lambda < 0.145$; thus, the non-propagating or the higher-order modes do not highly affect the results.

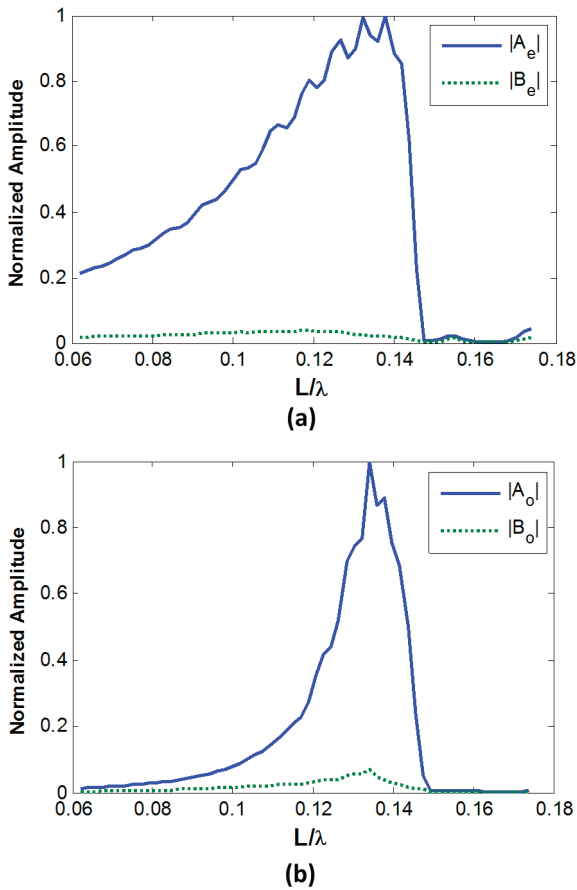


Fig. 6. Amplitudes of the first and second modes; (a) even modes and (b) odd modes.

Such as the even mode, the odd mode shows similar behavior in this frequency range. The higher normalized cutoff frequency is about 0.145. At this frequency the attenuation increases considerably. The lower normalized cutoff

frequency for the odd mode is about 0.12, as will be discussed further in what follows.

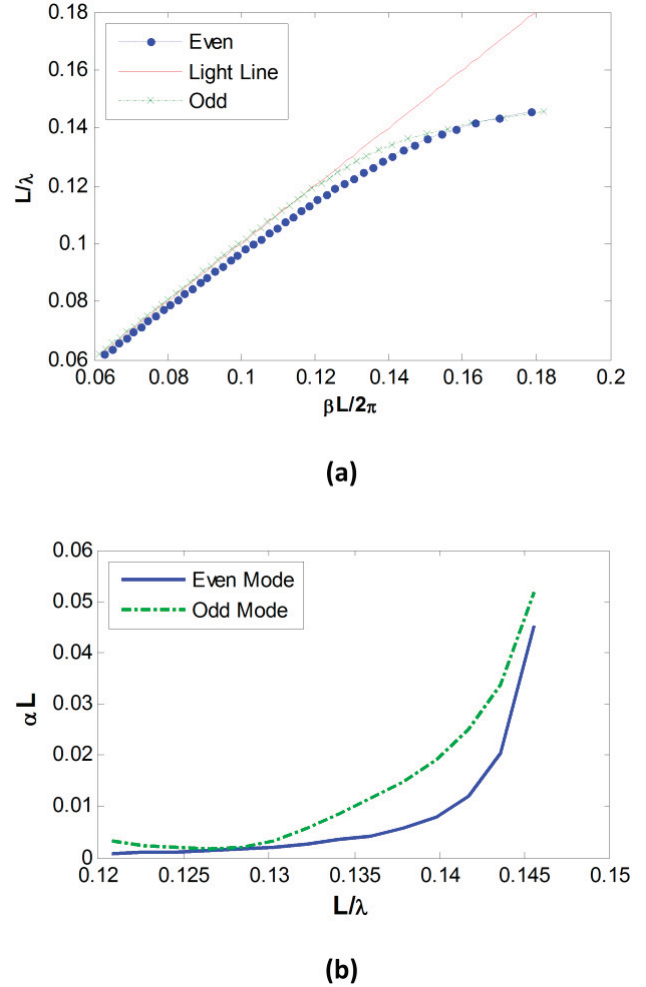


Fig. 7. Propagation (a) and attenuation (b) constants for the even and odd modes.

The propagation constant for the even and odd modes is calculated and depicted in Fig. 7 (a). The results are in agreement with the results reported by Talebi and Shahabadi [8] for the first even and odd modes. Also, the accuracy of the GMT results is compared and validated with other techniques in [11, 24]. There is no higher-order modes or their extinction length is smaller than the length of the simulated chain. Note that α and β are calculated simultaneously as a complex wave-number. Figure 7 (b) shows the attenuation constant α for even and odd modes. According to Fig. 4 (b), at lower frequencies, a longer chain is needed for the attenuation constant to converge.

For a chain of 100 nanorods results for the normalized frequencies below 0.12 are not accurate, but follow the well-known behavior of the attenuation constant. The field distributions for these modes at a normalized frequency of $L/\lambda = 0.14$ are depicted in Fig. 8.

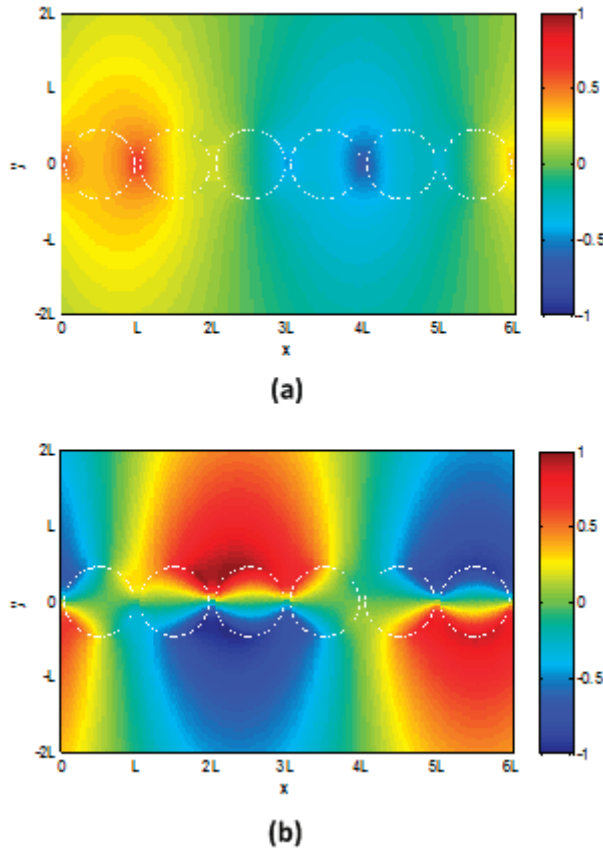


Fig. 8. Distribution of the normalized amplitude of the magnetic field at $L/\lambda=0.14$ (a) even mode and (b) odd mode.

The confinement of the EM wave is an important characteristic of nanorod-chain waveguides. Let us define R/r as the normalized spacing from the waveguide axis at which the longitudinal component of the poynting vector drops to half of its maximum value. Figure 9 shows this normalized spacing R/r as a function of the normalized frequency. The inset of this figure shows the normalized poynting vector (P/P_{\max}) in the propagation direction for different distances from the chain axis at the normalized frequency, $L/\lambda = 0.132$. This figure

reveals that the even mode is more confined in comparison to the odd mode. Also, it shows that as the frequency increases, the EM field becomes more confined by the chain.

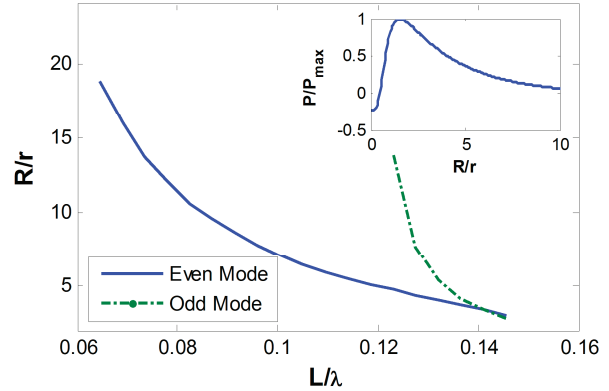


Fig. 9. Confinement of the EM fields for the even and odd modes.

VI. CONCLUSION

In this paper, we calculated the dispersion diagram of a nanorod-chain waveguide using GMT and demonstrated that the propagation and attenuation constants can be obtained directly by observing propagation of modes along a finite chain. Using GMT, it is observed that a short chain of finite length is sufficient for the calculation of the phase constant. However, the attenuation constant, α , requires a longer chain. These parameters are calculated for two propagating modes in the normalized frequency range of $0.06 < L/\lambda < 0.18$. This method is more effective for calculation of the propagation and attenuation constants for modes with higher attenuation in comparison with previous report [8].

Although, we have demonstrated this method for the modal analysis of a 2D waveguide of nanorods, it can be used for the analysis of 3D waveguide structures containing nanoparticles of an arbitrary shape.

REFERENCES

- [1] J. Takahara, S. Yamagishi, H. Taki, A. Morimoto, and T. Kobayashi, "Guiding of a one-dimensional optical beam with nanometer diameter," *Opt. Lett.*, vol. 22, pp. 475-477, 1997.
- [2] M. Quinten, A. Leitner, J. Krenn, and F. Aussenegg, "Electromagnetic energy transport via

- linear chains of silver nanoparticles,” *Opt. Lett.*, vol. 23, pp. 1331-1333, 1998.
- [3] M. Brongersma, J. Hartman, and H. Atwater, “Electromagnetic energy transfer and switching in nanoparticle chain arrays below the diffraction limit,” *Physical Review B* vol. 62, pp. R16356-R16359, 2000.
- [4] S. Maier, P. Kik, and H. Atwater, “Optical pulse propagation in metal nanoparticle chain waveguides,” *Physical Review B* vol. 67, 2003.
- [5] R. Shore and A. Yaghjian, “Travelling electromagnetic waves on linear periodic arrays of lossless spheres,” *Electronics Letters*, vol. 41, pp. 578-580, 2005.
- [6] A. Alù and N. Engheta, “Theory of linear chains of metamaterial/plasmonic particles as sub diffraction optical nano transmission lines,” *Departmental Papers*, (ESE), 2006.
- [7] M. Sukharev and T. Seideman, “Coherent control of light propagation via nanoparticle arrays,” *Journal of Physics B: Atomic, Molecular and Optical Physics*, vol. 40, pp. S283-S298, 2007.
- [8] N. Talebi and M. Shahabadi, “Analysis of the propagation of light along an array of nanorods using the generalized multipole techniques,” *Journal of Computational and Theoretical Nanoscience*, vol. 5, pp. 711-716, 2008.
- [9] A. Hochman and Y. Leviatan, “Rigorous modal analysis of metallic nanowire chains,” *Optics Express*, vol. 17, p. 13561, 2009.
- [10] Y. Hadad and B. Steinberg, “Green’s function theory for infinite and semi-infinite particle chains,” *Phys. Rev. B*, vol. 84, p. 125402, 2011.
- [11] S. Bajestani, M. Shahabadi, and N. Talebi, “Analysis of plasmon propagation along a chain of metal nanospheres using the generalized multipole technique,” *J. Opt. Soc. Am. B*, vol. 28, pp. 937-943, 2011.
- [12] D. Szafranek and Y. Leviatan, “A source-model technique for analysis of wave guiding along chains of metallic nanowires in layered media,” *Optics Express*, vol. 19, p. 25397, 2011.
- [13] I. Udagedara, I. Rukhlenko, and M. Premaratne, “Complex- ω approach versus complex- k approach in description of gain-assisted surface plasmon-polariton propagation along linear chains of metallic nanospheres,” *Phys. Rev. B*, vol. 83, p. 115451, 2011.
- [14] B. Rolly, N. Bonod, and B. Stout, “Dispersion relations in metal nanoparticle chains: necessity of the multipole approach,” *J. Opt. Soc. Am. B*, vol. 29, pp. 1012-1019, 2012.
- [15] K. Sendur, “Optical aspects of the interaction of focused beams with plasmonic nanoparticles,” *Applied Computational Electromagnetics Society (ACES) Journal*, vol. 27, no. 2, pp. 181-188, Feb. 2012.
- [16] S. Park and D. Stroud, “Surface-plasmon dispersion relations in chains of metallic nanoparticles: An exact quasistatic calculation,” *Phys. Rev. B*, vol. 69, p. 125418, 2004.
- [17] C. Tserkezis and N. Stefanou, “Calculation of waveguide modes in linear chains of metallic nanorods,” *J. Opt. Soc. Am. B*, vol. 29, pp. 827-832, 2012.
- [18] W. Weber and G. Ford, “Propagation of optical excitations by dipolar interactions in metal nanoparticle chains,” *Phys. Rev. B*, vol. 70, p. 125429, 2004.
- [19] D. Han, Y. Lai, K. Fung, Z.-Q. Zhang, and C. Chan, “Negative group velocity from quadrupole resonance of plasmonic spheres,” *Phys. Rev. B*, vol. 79, p. 195444, 2009.
- [20] E. Simsek, “On the surface plasmon resonance modes of metal nanoparticle chains and arrays,” *Plasmonics* vol. 4, pp. 223-230, 2009.
- [21] D. Van Orden, Y. Fainman, and V. Lomakin, “Optical waves on nanoparticle chains coupled with surfaces,” *Opt. Lett.* vol. 34, pp. 422-424, 2009.
- [22] E. Simsek, “Full analytical model for obtaining surface plasmon resonance modes of metal nanoparticle structures embedded in layered media,” *Opt. Express*, vol. 18, pp. 1722-1733, 2010.
- [23] I. Tsukerman, “A new computational method for plasmon resonances of nanoparticles and for wave propagation,” *IEEE/ACES International Conference on Wireless Communications and Applied Computational Electromagnetics*, pp. 909-912, Honolulu, Hi, April 2005.
- [24] J. Smajic, C. Hafner, L. Raguin, K. Tavzarashvili, and M. Mishrikey, “Comparison of numerical methods for the analysis of plasmonic structures,” *Journal of Computational and Theoretical Nanoscience*, vol. 6, pp. 763-774, 2009.
- [25] C. Hafner, *The Generalized Multipole Technique for Computational Electromagnetics*, Artech House Publishers, 1990.
- [26] P. Johnson and R. Christy, “Optical constants of the noble metals,” *Phys. Rev. B*, vol. 6, pp. 4370-4379, 1972.



Yaghoob Rahbarihagh received the B.S. degree in Electrical Engineering from the University of Tehran, Iran, in 2009, and the M.S. degree in Communications Engineering (Fields and Waves) from the University of Tehran, Iran, in 2012. He was an engineering research associate at the Microwave and Photonic Research Labs at the University of Tehran. His research interests include photonics, plasmonics, and electromagnetics.



Farid Kalhor received the B.S. degree in Electrical Engineering from the University of Tehran, Iran, in 2009, and the M.S. degree in Communications Engineering (Fields and Waves) from the University of Tehran, Iran, in 2012. He was an engineering research associate at the Microwave and Photonic Research Labs at the University of Tehran. His research interests include photonics, plasmonics, and electromagnetics.



Jalil Rashed-Mohassel received the M.Sc. degree in Electronics Engineering from the University of Tehran, Tehran, Iran, in 1976 and the Ph.D. degree in Electrical Engineering from the University of Michigan, Ann Arbor, in 1982. Previously, he was with the University of Sistan and Baluchestan, Zahedan, Iran. In 1994, he joined University of Tehran where he is teaching and performing research as a Professor in antennas, EM theory and applied mathematics. He served as the academic Vice-Dean, College of Engineering, General Director of Academic Affairs, University of Tehran and Chairman of the school of ECE, Principal member of Center of Excellence on Applied Electromagnetic Systems and the Director of the Microwave Laboratory.

Prof. Rashed-Mohassel was selected as the Brilliant National Researcher by the Iranian Association of Electrical and Electronics Engineers in 2007, and was the Distinguished Professor (2008–2009) in the 1st Education Festival, University of Tehran.



Mahmoud Shahabadi received the B.Sc. and MSc degrees from the University of Tehran, Tehran, Iran, and the Ph.D. degree from Technische University at Hamburg-Harburg, Germany, in 1988, 1991, and 1998, respectively, all in Electrical Engineering.

Since 1998, he has been an Assistant Professor, Associate Professor and then a Professor with the School of Electrical and Computer Engineering, University of Tehran. From 2001 to 2004, he was a Visiting Professor with the Department of Electrical and Computer Engineering, University of Waterloo, Canada.

His research interests and activities encompass various areas of microwave and millimeter-wave engineering, as well as photonics. Computational electromagnetics for microwave engineering and photonics are his special interests.

Single Feed Dual-Polarization Dual-Band Transmitarray for Satellite Applications

S. Zainud-Deen, S. Gaber, H. Malhat, and K. Awadalla

Department of Electronics and Electrical Communications Engineering,
Faculty of Electronic Engineering, Menoufiya University, Egypt
anssaber@yahoo.com, er_honida1@yahoo.com

Abstract—In this paper, two transmitarrays are designed, analyzed, and simulated for satellite applications. The first transmitarray is designed for dual linear polarization at a center frequency of 12 GHz. The second transmitarray is designed for two frequency bands: 17.15 GHz to 17.9 GHz for vertical polarization and 11.5 GHz to 12.4 GHz for horizontal polarization. The dual polarization is obtained by an independent adjustment of the dimensions of two orthogonal slots in the transmitarray unit cell. The design is carried out independently for each polarization. The transmitarray unit cell uses two dielectric substrate layers arranged to be one on each side of a conducting plane. On each substrate, one face has metallization containing the patches, and the other face has metallization containing the ground plane. The two patches are coupled by two cross slots of lengths L_V and L_H in the ground plane and each patch is loaded with two cross slots of lengths $L_V/2$ and $L_H/2$. The unit cell achieves 360° of phase agility with less than 3.8 dB of variation in the transmission magnitude in the tuning range. The transmitarray consisted of 17×17 elements with the unit cell size were set at 13 mm. A circular feed horn is located on the central normal to the transmitarray and the configuration looks like a lens antenna. Two separate feeding pins are used to excite the horn antenna for horizontal and vertical polarizations. The results are worked out using two basically different numerical techniques, the finite element method, FEM, and the finite integration technique, FIT. Good agreement was obtained.

Index Terms — DRA, dual-band, Polarization, and Transmitarray.

I. INTRODUCTION

Transmitarray antenna is a good candidate for high-gain and broadband performance. It also has the privileges of light-weight, simple to fabricate, and inexpensive to manufacture [1]. As a high gain antenna, it is suitable for applications, such as radar, satellite communications, and remote sensing. The transmitarray performance is related to lens techniques. Its size and weight are advantages relative to shaped dielectric lenses. Furthermore, its feed can be placed directly in front of the aperture without causing blockage losses or affecting the radiation patterns that are inherent in a reflectarray configuration [1]. The objective of the transmitarray unit cell is to add a phase shift to the waves passing it, such that the phase shift should become adjustable in the range of 0 to 360° . The main drawback of the transmitarray is its limited bandwidth, which is mainly due to the limited bandwidth of the element itself [2]. A number of different transmitarray configurations have been reported in the literature. These configurations can be classified according to the techniques that were used to adjust the phase of the incoming wave. Transmitarrays were designed using stub-loaded microstrip patches [3], and others using elements connected through multiple layers by a delay line [4]. A broadband four-layer transmitarray using double square printed ring elements is illustrated in [1].

A design of multilayer dielectric resonator transmitarray for near-field and far-field fixed RFID reader application at 5.8 GHz is presented in [5]. A three-layer printed reflectarray for dual polarization with different coverage in each polarization for space applications has been designed and tested in [6]. Also, a new application

of aperture coupled dielectric resonator as a cell element in design of a dual linear polarized reflectarray at X-band is investigated in [7]. A dual linear polarized printed reflectarray using slot loaded patch elements is investigated in [8]. The goal of this paper is to design a dual-polarization dual-band transmitarray. Two transmitarrays are simulated. The first transmitarray is designed for dual polarization at 12 GHz. The second transmitarray is designed for two frequency bands: 17.15 GHz to 17.9 GHz for vertical polarization and 11.5 GHz to 12.4 GHz for the horizontal polarization. The results are developed using finite element method [9] and compared with that determined using the basically different finite integration technique [10]. In this work a single feed horn is used for horizontal and vertical polarization at different frequency bands instead of dual feeds used in [7, 8]. The two orthogonal linear polarizations can be controlled independently by using two orthogonal slots in the cell element. The slot lengths are used to control the transmission phase. For dual band operation, each of the orthogonal slots is designed to resonant at one of the two considered frequency bands.

II. THE CELL ELEMENT

The cell element in a transmitarray is the crucial part, which determines most of the parameters of the array. The cell is that, which controls the bandwidth, the polarization, and the transmission coefficient of the array. The cell should provide the amplitude and phase shift needed at each location in the array to produce the specific radiation in the specific direction. To reach full flexibility in getting the radiation in any specific direction, the cell element should be able to add any needed phase shift in the range from 0° to 360° . The unit cell is designed for having transmission phase variation from 0° to 360° with corresponding transmission magnitude variation from 0 to nearly -3 dB. The unit cell design process is go for this goal.

A thin dielectric slab will produce a constant phase shift of the order of several degrees (around 2 or 3 degrees). A slotted ground plane between two dielectric slabs will produce a phase shift ranging from 0° to about 175° depending upon the length of the slot as given in Fig. 1. To increase the phase shift of the transmitted wave a conducting square

patch is added on one side face of the slab and centered with the ground slot. This actually made things worse and reduced the phase shift by about 20° . Then adding a slot on the patch parallel to the ground slot and centered with it but of half its length has improved the phase shift by adding 100° to that of the ground slot to reach about 280° maximum as shown in Fig. 2. This structure can be represented as two sections of waveguides connected in tandem to produce a delay of 280° for a travelling wave. To achieve the 360° needed, a third section of a waveguide is added in tandem. This is done by adding a similar slotted patch on the opposite face of the composite dielectric to end up with the cell element shown in Fig. 3. This completes the cell structure with three slotted elements on top of each other (in tandem) and in a symmetrical way on the same axis to add the phase shift of each section to end up with the needed 360° as shown in Fig. 3. Thus, by changing the length of the slots, the needed phase shift at each location in the array is obtained. The length of the ground slot is changed but with keeping the length of the slots on the patches to be half the accompanying ground slot length. The total response of the complete cell becomes similar to critical coupling in inductive coupled tuned circuits.

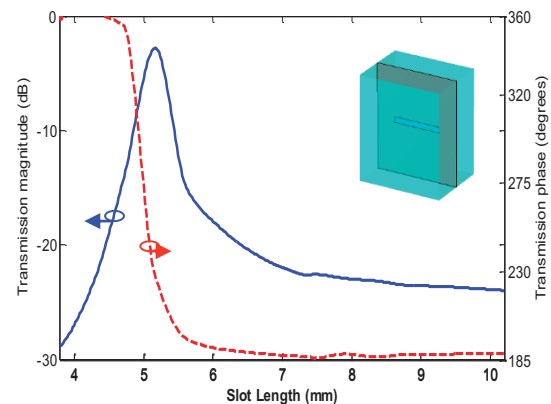


Fig. 1. A slotted ground plane sandwiched between two dielectric slabs.

To get the cell responding in a similar way to two orthogonal linearly polarized waves, identical slots orthogonal to the first ones is added on both patches on the two outer faces as well as on the ground plane to end up with the cell structure shown in Fig. 4. As expected, due to the

orthogonality of the slots, there is no mutual effect has been noticed between the orthogonal groups of slots sharing the same cell.

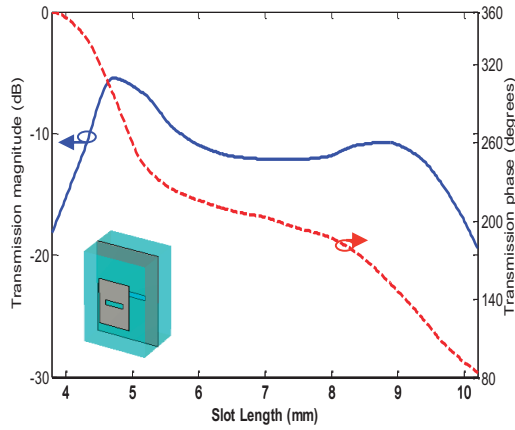


Fig. 2. The transmission coefficient after adding the slotted patch.

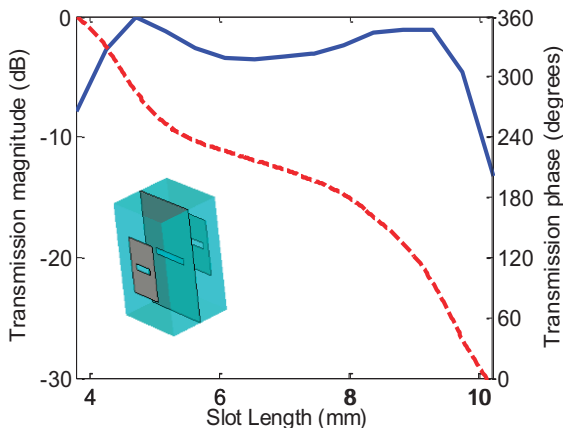


Fig. 3. The complete cell structure for one polarization.

III. STRUCTURE, SIMULATION, AND NUMERICAL RESULTS

A. Case A: Dual-polarization transmitarray at 12 GHz

Figure 4 depicts the layer distribution and materials employed in the transmitarray unit cell. It consists of two patches on either side of a ground plane, coupled by two cross slots of lengths L_V and L_H in the ground plane. Each patch is loaded with two cross slots of lengths $L_V/2$ and $L_H/2$. The slot widths were set at $W_V = W_H = 0.7$ mm. The transmitarray unit cell uses two substrate layers with $\epsilon_r = 4$ (Eccostock HIK500F). The unit cell size (L) was set at 13 mm. The cell dimensions are

summarized in Table I. these dimensions are optimized to give transmission phase of 360° at the center frequency with maximum transmission magnitude.

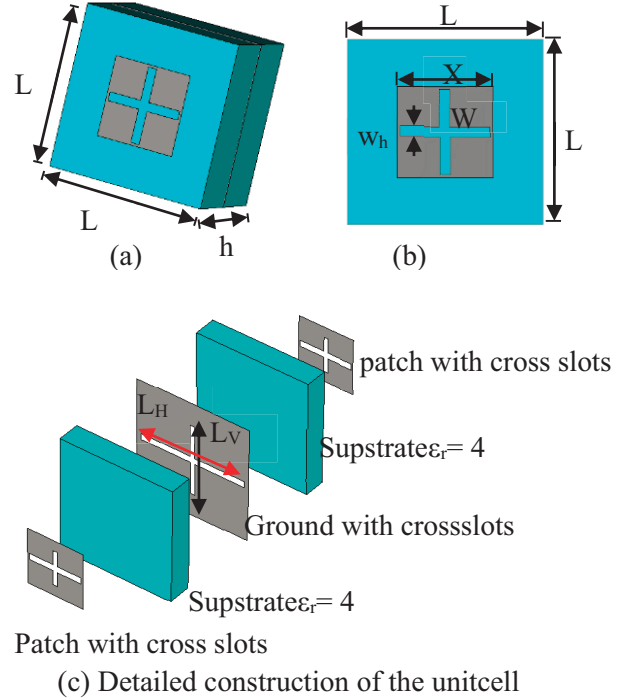


Fig. 4. Reconfigurable transmitarray element structure.

Table I: The unit cell dimensions

L	X	h	Slot width $W_V = W_H$
13 mm	6 mm	2.5 mm	0.7 mm

The transmission magnitude and phase are determined using the finite element method based simulator. The software was used to model an infinite array of elements. This procedure assumes that the transmission from each individual element surrounded by elements of different sizes can be approximated by the transmission of an infinite array of identical elements. An infinite array was modeled to simulate a single element enclosed within the appropriate magnetic and electric waveguide boundary conditions, as shown in Fig.5. A plane wave was used as the excitation of a two-dimensional infinite array of similar elements. In this simulation, lossless materials were assumed and only normal incidence was considered for a

linearly polarized incident wave. The simulation results have achieved a 360° of phase agility with less than 3.8 dB of variation in transmission magnitude throughout the tuning range as shown in Fig. 6. The results are validated by a good agreement compared with that calculated by the finite integration technique.

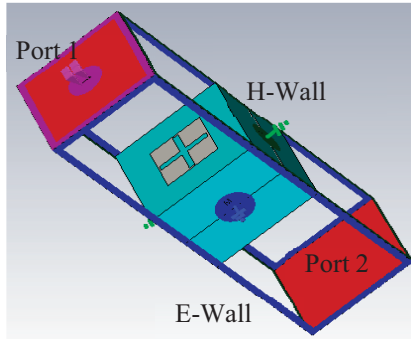


Fig. 5. Structure of waveguide simulator.

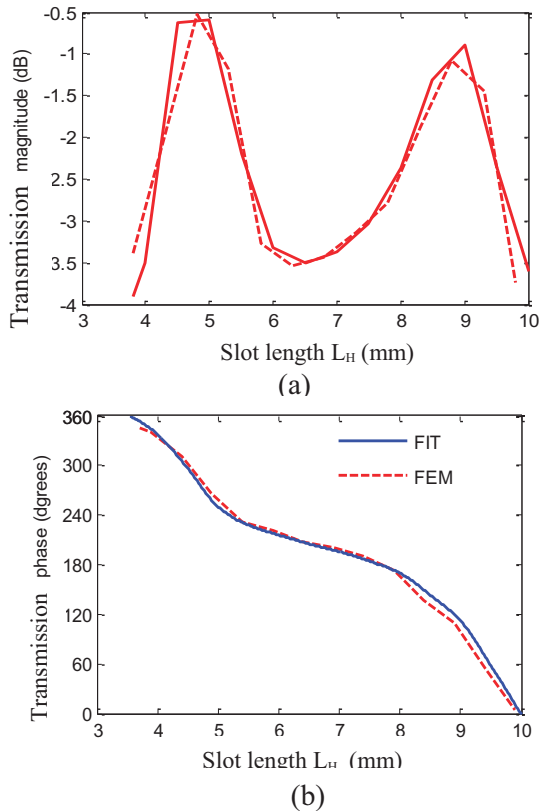


Fig. 6. Transmission (a) magnitude and (b) phase versus slot length L_H with $L_V = 0$, at $f = 12$ GHz.

Figure 7 illustrates the transmission coefficient magnitude and phase for different values of the slot length L_V . It shows that the transmission coefficient can be tuned by varying the slot length L_H without being really affected by the cross slot length L_V . This behavior demonstrates that two orthogonal linear polarizations can be controlled independently by the two orthogonal slots. A transmitarray composed of 17×17 elements with fixed dimension (L) of 13 mm and covering an area of $221 \text{ mm} \times 221 \text{ mm}$ was designed and simulated.

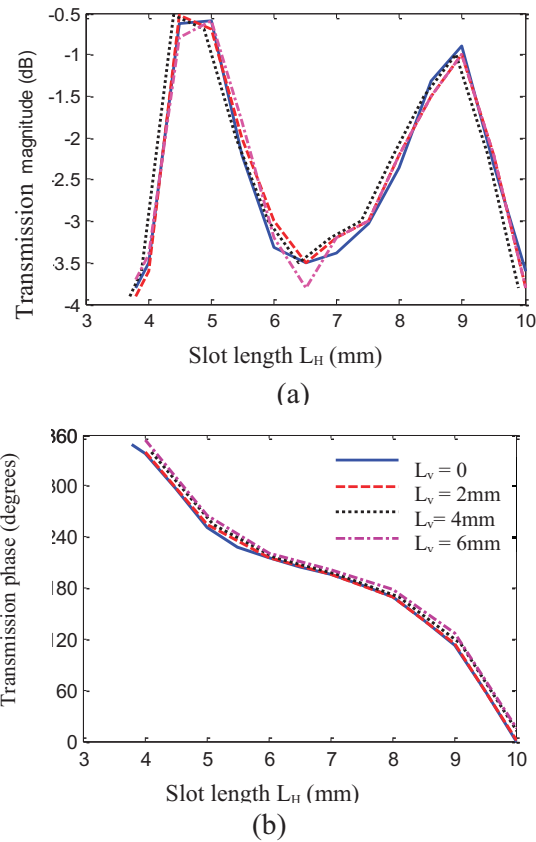


Fig. 7. Transmission (a) magnitude and (b) phase versus slot length L_H with several L_V at $f = 12$ GHz.

A circular horn was used as the feed, with focal length to diameter ratio, F/D , set to 1.0 to decrease the level of the sidelobes in the radiation pattern. The transmitting horn antenna illuminates one side of the transmitarray. The feed horn was positioned such that the transmitarray was prime-focus fed. This feed position provides an illumination level at the transmitarray edges of -10 dB for E-plane and -9 dB for H-plane at 12 GHz. The feed horn was 60 mm long, with an aperture radius of 25mm. Two

separate feeding pins are used to excite the horn antenna for V and H polarizations. A schematic of the transmitarray configuration showing the feed is shown in Fig. 8.

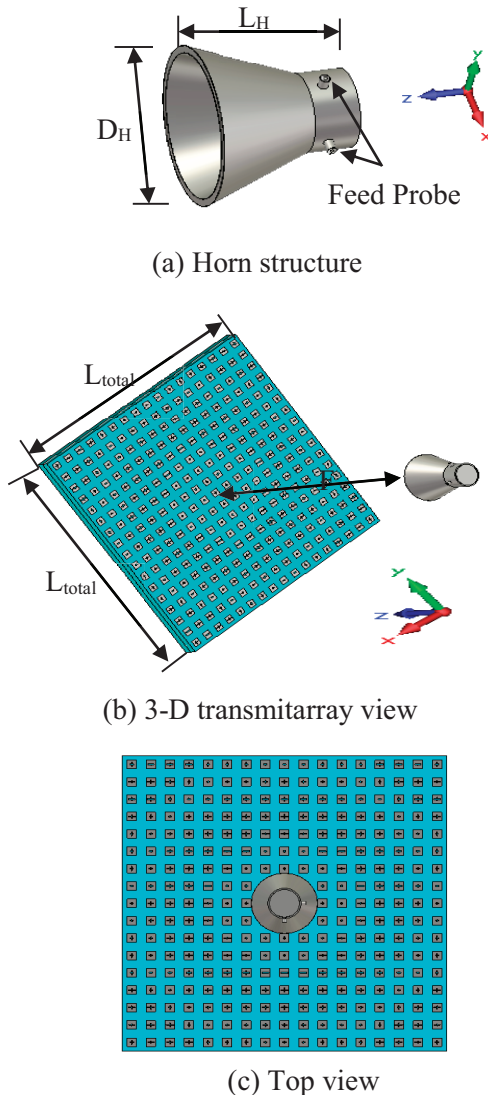


Fig. 8. Transmitarray layout fed with circular horn antenna.

To design transmitarray elements; the phase of the transmitted wave should have a progressive variation over the whole surface. This implies that phases in the whole range from 0° to 360° should be used for the transmission coefficient with minimum insertion loss through the structure. The transmitarray is designed for linear polarization in the two cases of H-polarization (with the electric field on the direction of x axis) and V-polarization

(with the electric field on the direction of the y-axis). The beam shaping for each polarization is achieved by adjusting the phase of the transmitted coefficient at each element independently for each linear polarization. The required phase shift for each polarization was realized by adjusting the slot length that is either L_V or L_H . Figure 9 (a) shows the distribution of the slot length L_V for horizontal polarization while Fig.9 (b) shows the distribution of the slot length L_H for the vertical polarization. Figure 9 (c) shows the variation of the cross slot lengths for vertical and horizontal polarizations along the transmitarray elements.

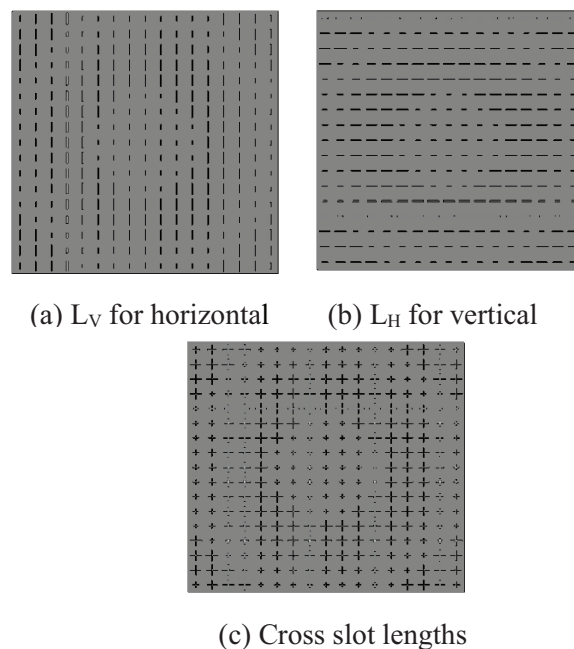
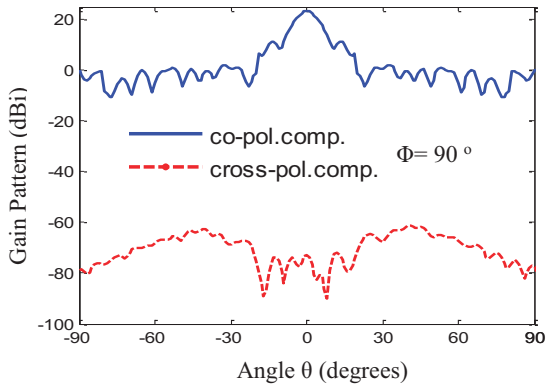


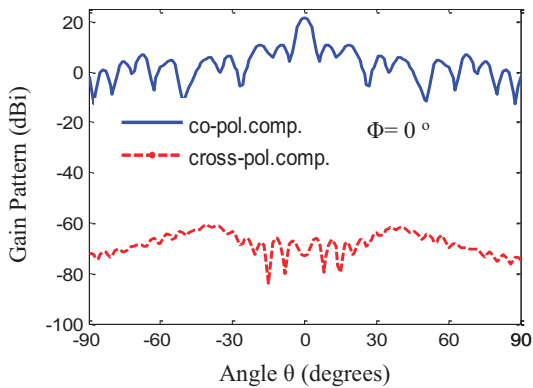
Fig. 9. Slot lengths for vertical and horizontal polarization.

As the total structure of the transmitarray is very large, simulation with the FEM requires a huge memory size, which is difficult. Consequently, the transmitarray was modeled and simulated only by FIT method. For V-polarization, computed radiation patterns components (co-polar and cross-polar) are shown in Fig. 10 at the operating frequency 12 GHz. Very high isolation between polarizations is achieved. The first sidelobe levels in the E- and H-planes are approximately 12 dB and 11.2 dB below the main peaks, respectively. The gain as a function of frequency is shown in Fig. 11. A 7.5 % bandwidth (0.9 GHz) is achieved with 1 dB gain variations. The simulated results for the H-

polarization are shown in Fig. 12. The gain as a function of frequency is depicted in Fig. 13. The performances for the V and H polarizations are almost identical.



(a) E- plane



(b) H-plane

Fig. 10. E-plane and H-plane pattern plot for a boresight 17×17 transmitarray at 12 GHz for V-polarization.

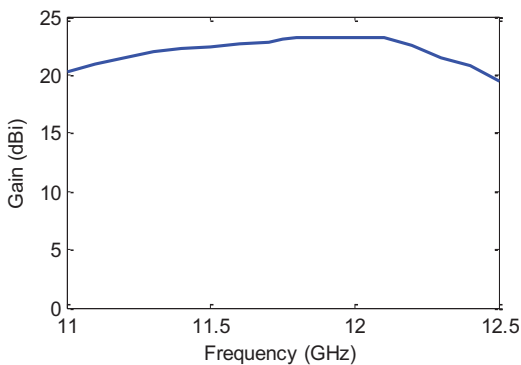
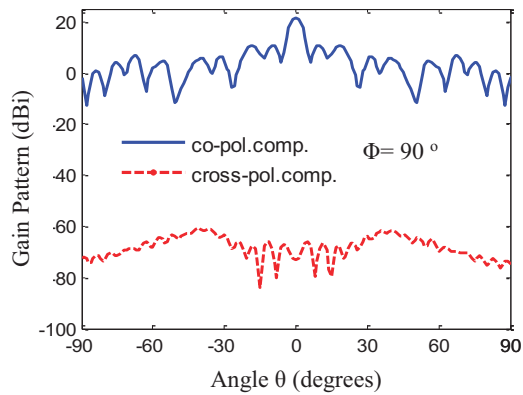


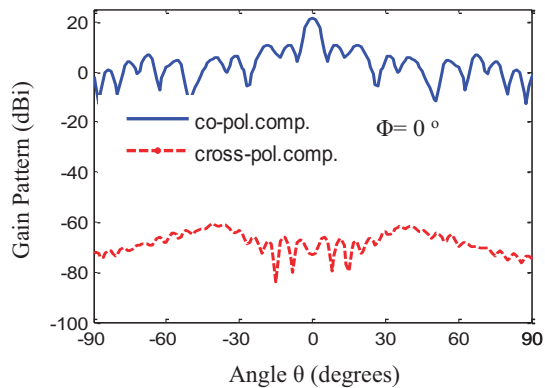
Fig. 11. 17×17 Transmitarray peak gain versus frequency for V-polarization.

B. Case B: Dual-polarization dual-band transmitarray

In this case, the transmitarray has been designed to produce a focused beam at 17.5 GHz for V-polarization and also at 12 GHz for H-polarization for satellite applications. Each polarization is controlled by adjusting the cross slots lengths, L_V and L_H , respectively according to the frequency of operation for each polarization. The range of the slot length L_V is changed as shown in Fig. 14. The slot width $W_V = 0.5$ mm and $W_H = 0.7$ mm in this case are used to get the phase transmission curve covering the range of 360° phase shift. The cross slots lengths for vertical and horizontal polarizations for each array element are shown in Fig.15. E-plane and H-plane far-field patterns of the transmitarray at 12 GHz and 17.5 GHz are depicted in Fig.16. The gains versus frequency in the two bands are illustrated in Fig. 17.



(a) E- plane



(b) H-plane

Fig. 12. E-plane and H-plane pattern plot for a boresight 17×17 transmitarray at 12 GHz for H-polarization.

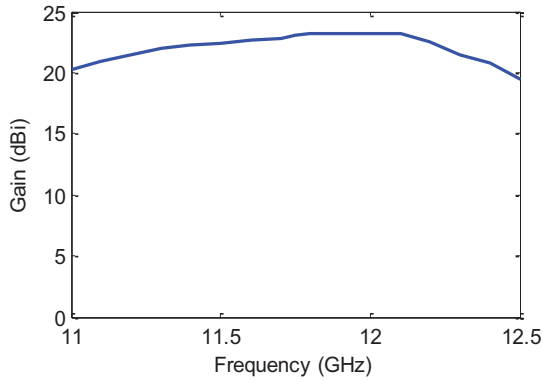


Fig. 13. 17×17 Transmittarray peak gain versus the frequency for H-polarization.

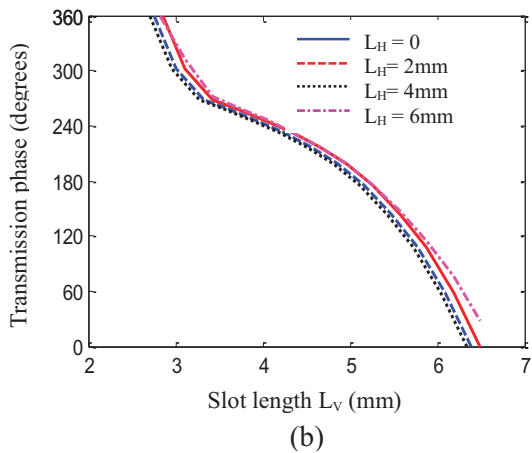
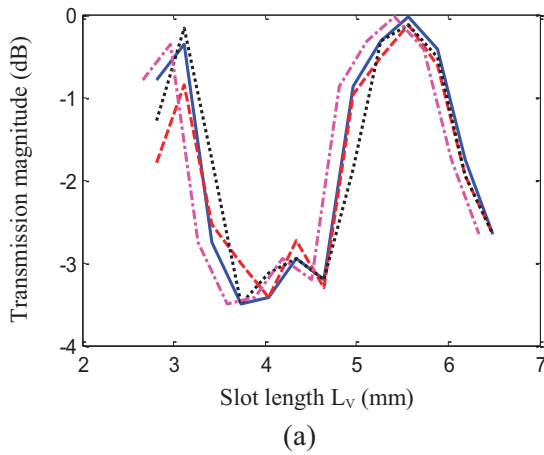


Fig. 14. Transmission (a) magnitude and (b) phase versus slot length L_V with several L_H at $f = 17.5$ GHz.

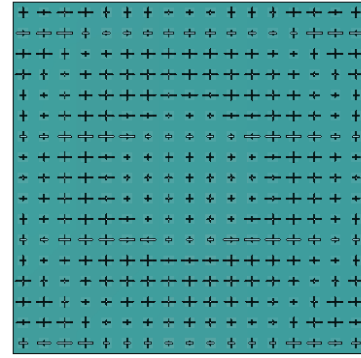
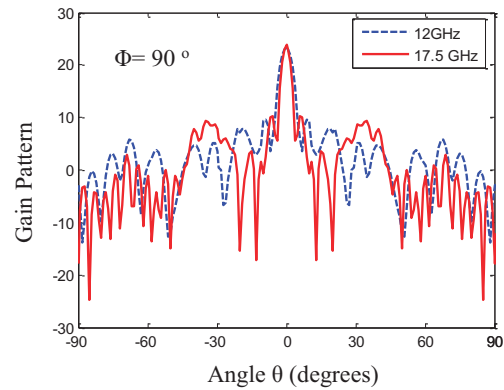
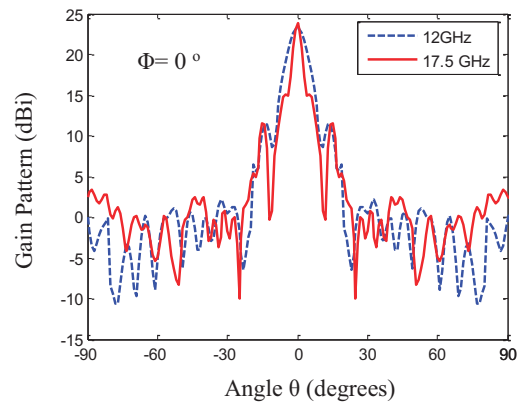


Fig. 15. Cross slots lengths for vertical and horizontal polarizations.



(a) E-plane



(b) H-plane

Fig.16. E-plane pattern plot for a boresight 17 × 17 transmitarray.

The vertical polarization here is operating at a higher frequency relative to that for the horizontal polarization. Thus, using the same overall dimensions of the array the beamwidth for the higher operating frequency (V-polarization) is narrower than that for the lower frequency (H-polarization). Also, the width of the slots for the

higher operating frequency has been selected narrower than that for the lower operating frequency. This variation in slot width resulted in a narrower bandwidth as shown in Table II.

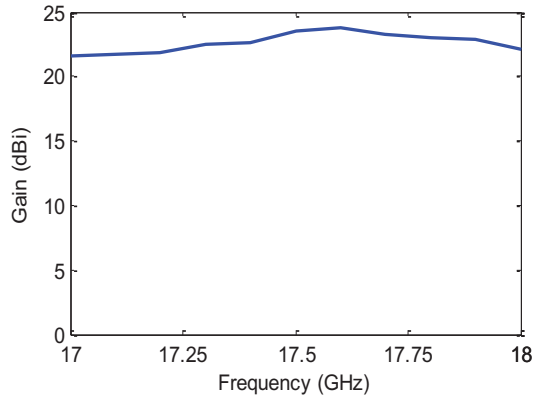


Fig. 17. 17×17 Transmittarray peak gain versus frequency.

Table II: compare the radiation characteristics for H-polarization and V-polarization.

	Gain (dB)	BW (GHz)	Beam width
Horizontal polarization (x-polarized)	23.2	0.9 (7.5%)	5°
Vertical polarization (y-polarized)	23.9	0.75 (4.28%)	4°

IV. CONCLUSION

The design and analysis of a dual-polarization dual-band transmitarray were presented in this paper. Two cases are considered, transmitarray, for vertical and horizontal linear polarization at 12 GHz for case A, while another one designed at two center frequencies, 17.5 GHz for vertical polarization and 12 GHz for horizontal polarization in case B. The transmitarray consists of 17×17 elements. The radiation patterns for each polarization are achieved by adjusting the phase of the transmission coefficient at each transmitarray unit cell independently for each polarization. The slot lengths are used to control the transmission phase. Full-wave analysis using the finite element method is applied. The results are validated by comparing with that calculated by the finite integration technique. Good agreement was shown.

REFERENCES

- [1] C. Ryan, J. Bray, and Y. Antar, "A broadband transmitarray using double square ring elements," *13th International Symposium on Antenna Technology and Applied Electromagnetics and the Canadian Radio Science Meeting (ANTEM/URSI)*, Toronto, Canada, pp. 1-4, 2009.
- [2] J. Huang and J. Encinar, *Reflectarray Antennas*, John Wiley and Sons, Inc., Hoboken, NJ, USA, 2007.
- [3] K. Lam, S. Kwok, Y. Hwang, and I. Lo, "Implementation of transmitarray antenna concept by using aperture coupled microstrip patches," *Asia Pacific Microwave Conference, APMC*, Hong Kong, pp.433- 436, 1997.
- [4] H. Son and W. Zhang, "Design of broadband element of transmitarray with polarization transform," *International Workshop on Small and Smart Antennas, Metamaterials and Applications (IWAT '07)*, pp. 287-290, Cambridge, UK, 2007.
- [5] S. Zainud-Deen, S. Gaber, H. Malhat, and K. Awadalla, "Multilayer dielectric resonator antenna transmitarray for near-field and far-field fixed RFID reader," *Progress In Electromagnetics Research C, PIER C*, vol. 27, pp. 129-142, 2012.
- [6] J. Encinar, L. Datashvili, J. Zornoza, M. Arrebola, M. Sierra-Castaner, J. Besada-Sanmartin, H. Baier, and H. Legay, "Dual-polarization dual-coverage reflectarray for space applications," *IEEE Transaction on Antennas and Propagation*, vol.54, no.10, pp.2827-2836, Oct. 2006.
- [7] A. Abd-Elhady, S. Zainud-Deen, A. Mitkees, and A. Kishk, "Dual polarized dual feed aperture-coupled DRA reflectarray," *29th National Radio Science Conference (NRSC 2012)*, Faculty of Engineering, Cairo University, Cairo, Egypt, pp. 97-102, 2012.
- [8] D. Cadoret, L. Marnat, R. Loison, R. Gillard, H. Legay, and B. Salome, "A dual linear polarized printed reflectarray using slot loaded patch elements," *The second European Conference Antenna and Propagation (EUCAP 2007)*, pp. 1-5, 2007.
- [9] D. Hutton, *Fundamentals of Finite Element Analysis*, McGraw-Hills Companies, USA, 2004.
- [10] S. Cooke, R. Shtokhamer, A. Mondelli, and B. Levush, "A finite integration method for conformal, structure-grid, electromagnetic simulation," *Journal of computational physics*, vol.215, pp. 321-347, 2006.

Broad-Band Power Divider Based on the Novel Split Ring Resonators

D. Jiang¹, Y. Xu², R. Xu², and Z. Shao¹

¹ School of Communication and Information Engineering
University of Electronic Science and Technology of China, Chengdu, 611731, P. R. China
merryjiangdi@163.com, shao_zh@uestc.edu.cn

² School of Electronic Engineering
University of Electronic Science and Technology of China, Chengdu, 611731, P. R. China
yhxu@uestc.edu.cn, rmxu@uestc.edu.cn

Abstract — A broad-band power divider, based on proposed novel split ring resonators, with the use of surface-mount components, is presented in this paper. This paper is focused on the design of generalized novel split ring resonators in a fully planar configuration. This novel split ring resonator exhibits multiple, alternating backward and forward-transmission bands, and is therefore promising for the synthesis of wideband microwave components. The equivalent circuit models, including parasitic parameters, of the structures is presented (based on electrically small planar resonators), the detailed procedure for the synthesis of these resonators by using the proposed circuit model, is illustrated. It is shown that excellent results in both performance and size can be obtained through the proposed approach, fully compatible with planar technology.

Index Terms - Equivalent circuit models, power divider, and split-ring resonators (SRRs).

I. INTRODUCTION

In the past several years, the feasibility to take advantage of the unusual properties of the so-called metamaterial technology has led to a great deal of research activity [1-5]. At microwave frequency bands, the propagation medium is generally fabricated from transmission lines, loaded by split-ring resonators (SRRs) or implemented in a dual configuration with respect to a conventional one, namely with lumped series

capacitances and shunt inductances [6-7]. The intense work carried out in the research group of Barcelona, Spain, is particularly representative of the SRR technology with several proposals, notably in terms of configurations on the basis of split-ring resonator and complementary split-ring resonator schemes [8].

On the other hand, the power divider and combiner are very important components for microwave power amplifiers [9]. Recent years, there has seen a worldwide effort to develop broadband power dividers due to the trend of wideband mobile systems [10-11]. Several power dividers based on the SRRs have been proposed. However, they are either high insertion loss or narrow band between output ports. To address this issue, this paper presents a novel broad-band power divider based on the SRRs but with improved performance compared with those previously mentioned work.

II. SYNTHESSES OF BULK METAMATERIAS

Among much geometry proposed to date, edge-coupled split ring resonators (EC-SRR) has been studied in great detail for the design of such artificial media. The split ring structure can support resonant wavelengths much larger than the diameter of the ring [12]. The EC-SRR structure changes the real part of magnetic permeability from positive to negative values, when signals with frequencies higher than the resonance frequency propagate through it. This negative

permeability can be employed with negative dielectric constant originating from another structure to produce negative refractive index materials [13]. In other words, the physical dimension is much smaller than the resonant wavelength, thus offering a quasi-static resonant effect and allowing very compact components designs.

When the EC-SRR shown in Fig. 1 (a) is excited by a time-varying external magnetic field directed along the z-axis, the cuts on each ring (which are placed on the opposite side of the EC-SRR) force the electric current to flow from one ring to another across the slots between them, in a form of a strong displacement current. The slots between the rings therefore behave as a distributed capacitance, and the whole EC-SRR has the equivalent circuit. EC-SRRs can be modeled as an LC resonant tank by virtue of the distributed capacitance (denoted as C) between concentric rings and inductance (denoted as L) of overall rings, as shown in Fig. 1 (b). The L is the SRR self-inductance and C is the capacitance associated with each EC-SRR half. The capacitance is $C = \pi r C_{pul}$, where r is the mean radius of the EC-SRR, and C_{pul} is the per unit length capacitance along the slot between the rings. The total capacitance of this circuit is $C/2$ considering taking into account the series connection of the capacitances of both EC-SRR halves. R is the actual electromagnetic loss of the microstrip. Taking into account the circuit model, its resonance frequency can be expressed as,

$$\omega_0 = 1/\sqrt{LC} . \quad (1)$$

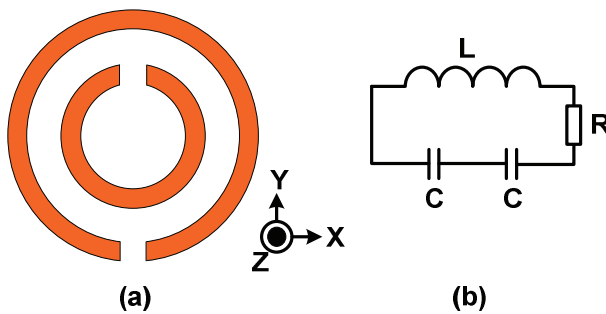


Fig. 1. (a) The typical edge-coupled split ring resonator (EC-SRR) and (b) its equivalent circuit model.

Spirals are well-known resonators in planar microwave circuitry. They can be used for the design of negative magnetic permeability and left-handed media [14]. This design also provides a strong magnetic dipole at resonance, thus being useful for metamaterial design. The electrical size can still be reduced by increasing the number of turns. This property is a clear advantage, as it implies a smaller electrical size at resonance. We have found that the printed circuit in Fig. 2 (a) has the same size as the one in Fig. 1 (a), but its resonant frequency is approximately one-half lower, which is shown in equation (2). From the equivalent circuit in Fig. 2 (b), it indicates that the resonance frequency of the 2-SR $\omega_{0[2-SR]}$ would be half of the resonance frequency of the EC-SRR $\omega_{0[EC-SRR]}$ with the same size [15]. Thus, the 2-SR is much easier to design and implement in RF and microwave circuits,

$$\omega_{0[2-SR]} = \frac{1}{2} \omega_{0[EC-SRR]} . \quad (2)$$

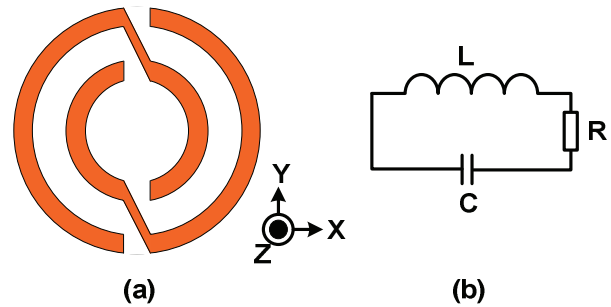


Fig. 2. (a) Typical two-turns spiral resonator (2-SR) and (b) its equivalent circuit model.

Based on microstrip technology, the layout and the canonical lumped circuit model corresponding to the proposed new 2-SR unit cell are characterized in Fig. 3 (losses have been excluded). Figure 3 (b) depicts the circuit model of the symmetrical unit cells shown in Fig. 3 (a). The LH contribution capacitance across the slot between the rings has been introduced into the model as C_L . The LH contribution, L_L represents the inductance generated by the 2-SR self-inductance. Similarly, the right-handed (RH) contribution contains the distributed shunt capacitance C_R and series inductance L_R , which are made by distribution parameters effect from the transmission line. To validate the use of the

proposed new 2-SR unit cell for compact circuit design, a power divider implemented by means of an impedance inverter is designed and tested [16]. Apart from power dividers, this unit cell will find applications in the designs of compact impedance matching, filter and many other passive circuits [17].

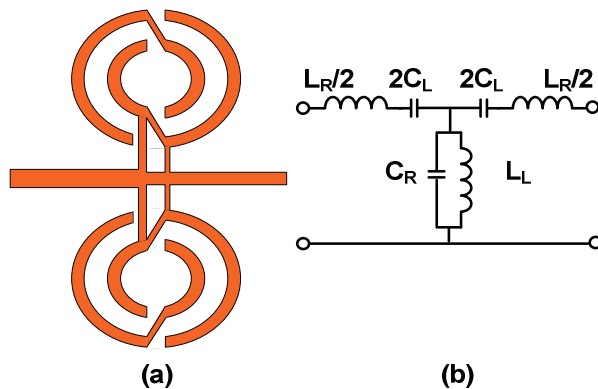


Fig. 3. Layout and canonical lumped circuit models of the new 2-SR unit cell; (a) the new 2-SR unit cell and (b) its equivalent circuit.

III. POWER DIVIDER DESIGN

The geometry of the proposed novel wideband power divider is shown in Fig. 4. This power divider printed is on a 0.254 mm thick RT5880 (substrate with dielectric constant $\epsilon_r = 2.2$ and loss tangent $\tan\delta = 0.0009$) with overall dimension of $15 \times 14.97 \text{ mm}^2$. The size of inner-square (R_1 , R_2) should be adjusted to determine the central frequency of power divider as shown in Fig. 5. For fixed R_1 and R_2 , the resonance frequency could be increased by decreasing length of branch (h), as shown in Fig. 6. It can also be obtained from Fig. 6 that the return loss of the power divider increases with increasing the branch length. These optimization works were managed by using commercial 3-D electromagnetic software high frequency structure simulator (HFSS) [18].

IV. RESULTS DISCUSSION

To validate the proposed design, the novel two-turns spiral SRR unit cell based power divider was fabricated. The photograph of the fabricated component is shown in Fig. 7. The prototype has been characterized and its relevant measured

scattering parameters (return losses and transmission coefficients) are shown in Fig. 8. By comparing the measured and simulated scattering parameters in Fig. 8, well agreement between simulated and measured results is obtained for the novel wideband microstrip power divider. However, the measured central frequency (5.4 GHz) is slightly higher than the simulated one (5.25 GHz). This shift is attributed to fabrication tolerances, connectors, and the substrate properties [19-21]. The measured return loss is below -20 dB, and the measured insertion loss, at each branch, is approximately -3.2 dB at the central frequency. The slightly higher loss of approximately 0.2 dB is due to inaccuracies in fabrication of the structure. Figure 9 shows simulated electric field distribution at simulated central frequency (5.25 GHz) on the proposed broad-band power divider. It can be seen that the proposed power divider achieves equal power dividing performance at the operating frequency. The measured results show that this novel unit cell can be used in the design and fabrication of miniaturized RF and microwave circuits [22, 23].

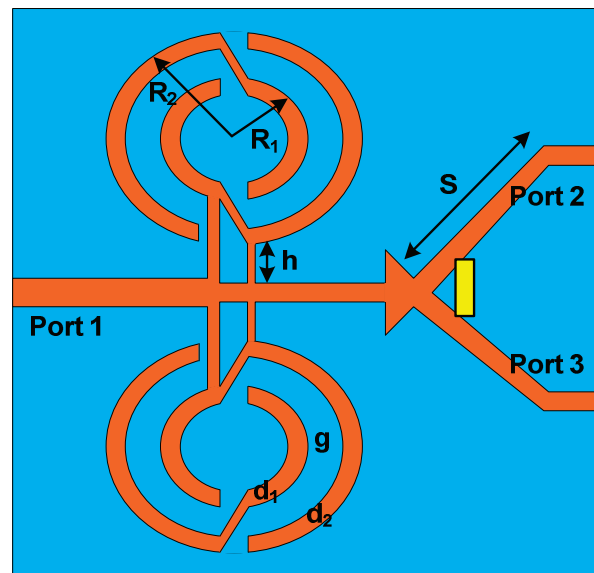
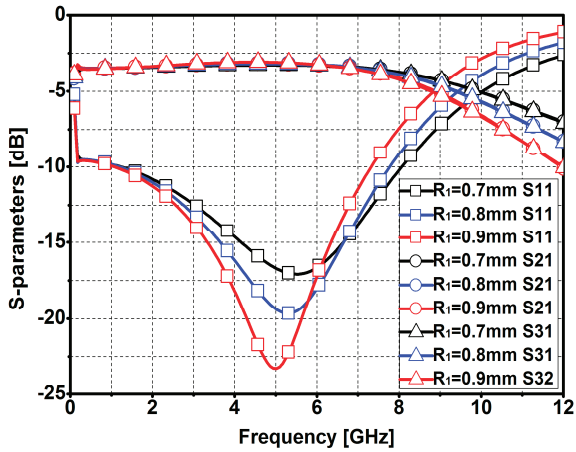
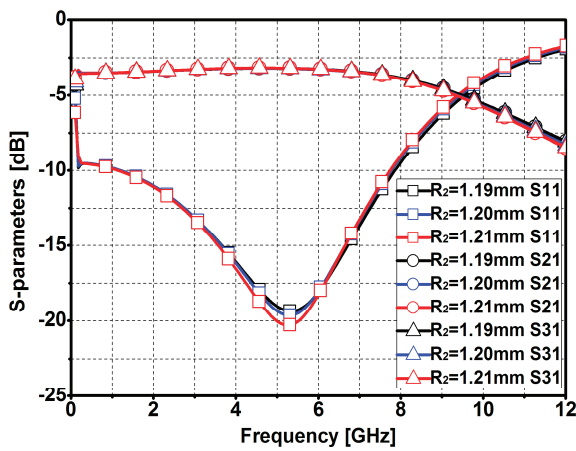


Fig. 4. Geometry of compact power divider, dimensions are $R_1 = 0.9 \text{ mm}$, $R_2 = 1.29 \text{ mm}$, $d_1 = 0.2 \text{ mm}$, $d_2 = 0.2 \text{ mm}$, $g = 0.19 \text{ mm}$, $h = 1.02 \text{ mm}$, $S = 10.9 \text{ mm}$, $W = 15 \text{ mm}$, and $L = 14.97 \text{ mm}$.



(a)



(b)

Fig. 5. S-parameters of (a) different radius of R1 and (b) different radius of R2.

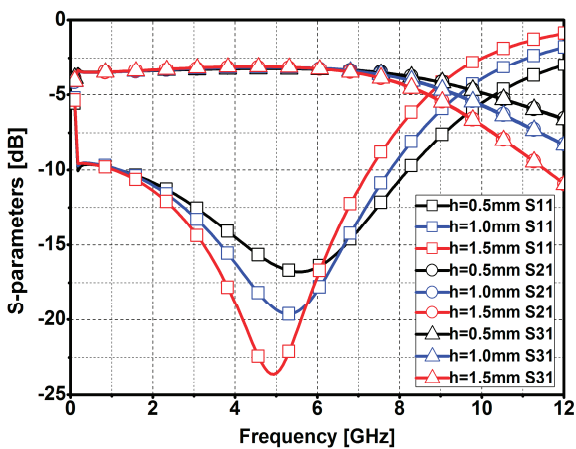


Fig. 6. S-parameters of different height of squares (h).

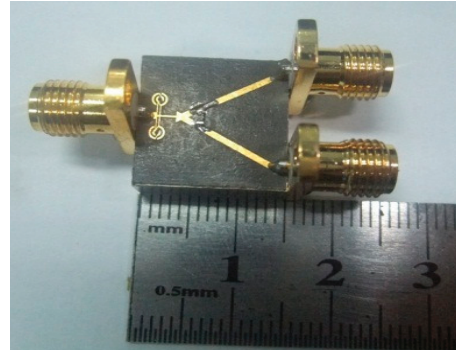


Fig. 7. Photograph of the proposed power divider.

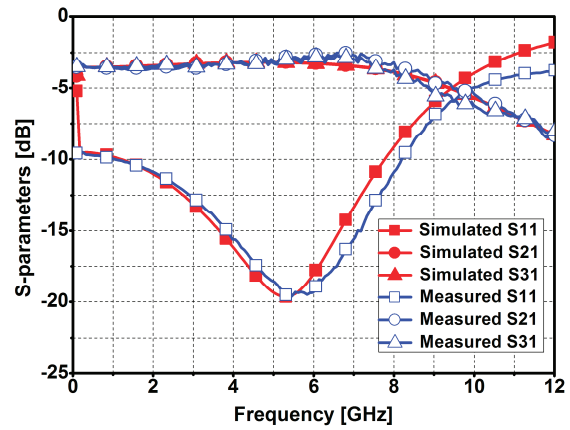


Fig. 8. Measured and simulated frequency responses for the thru (S21 and S31), and the return loss (S11) of the wideband power divider.

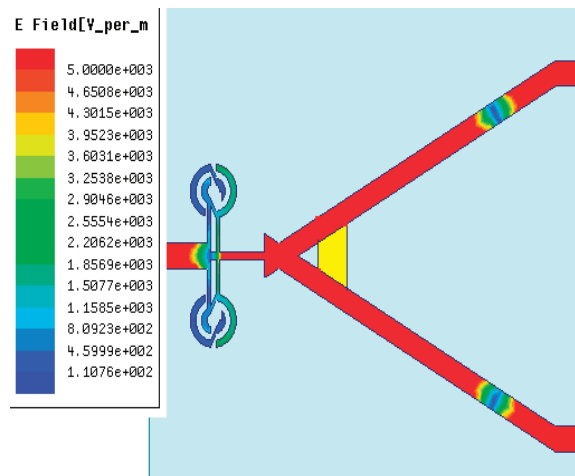


Fig. 9. Simulated electric field distribution at simulated central frequency (5.25 GHz) on the proposed wideband power divider.

V. CONCLUSION

A novel Wilkinson power divider using novel two-turns spiral resonator (2-SR) was proposed. The power divider not only shows excellent performance in a wide band, but also has compact size due to the use of proposed two-turns spiral SRRs cells. The new model developed is suitable for the design of compact broad-band microwave components, as has been demonstrated through the design and fabrication of a power divider. It can be easily implemented in microwave integrated circuit.

ACKNOWLEDGMENT

This work is supported by National Natural Science Foundation of China under Grant 61106115, the Fundamental Research Funds for the Central Universities under Grant ZYGX2011J018, and Excellent Ph.D. Candidate Academic Funds under Grant YBXSZC2013054.

REFERENCES

- [1] J. Pendry, A. Holden, W. Stewart, and I. Youngs, "Extremely low frequency plasmons in metallic mesostructures," *Phys. Rev. Lett.*, vol. 76, no. 25, pp. 4773-4776, June 1996.
- [2] D. Smith, W. Padilla, D. Vier, S. Nemat-Nasser, and S. Schultz, "Composite medium with simultaneously negative permeability and permittivity," *Phys. Rev. Lett.*, vol. 84, no. 18, pp. 4184-4187, May 2000.
- [3] V. Eleftheriades, A. Iyer, and P. Kremer, "Planar negative refractive index media using periodically L-C loaded transmission lines," *IEEE Trans. Microw. Theory Tech.*, vol. 50, no. 12, pp. 2702-2712, December 2002.
- [4] A. Oliner, "A planar negative-refractive-index medium without resonant elements," *IEEE MTT-S Int. Microw. Symp. Dig.*, Philadelphia, PA, vol. 1, pp. 191-194, June 2003.
- [5] A. Grbic and G. Eleftheriades, "Dispersion analysis of a microstrip-based negative refractive index periodic structure," *IEEE Microw. Wireless Compon. Lett.*, vol. 3, no. 4, pp. 155-157, Apr. 2003.
- [6] R. Marqués, F. Mesa, J. Martel, and F. Medina "Comparative analysis of edge and broad-side coupled split ring resonators for metamaterial design: Theory and experiment," *IEEE Trans. Antennas Propag.*, vol. 51, pp. 2572-2581, 2003.
- [7] C. Caloz and T. Itoh, "Novel microwave devices and structures based on the transmission line approach of meta-materials," *IEEE MTT-S Int. Microw. Symp. Dig.*, Philadelphia, PA, vol. 1, pp. 195-198, June 2003.
- [8] J. Baena, R. Marqués, F. Medina, and J. Martel "Artificial magnetic metamaterial design by using spiral resonators," *Phys. Rev. B*, vol. 69, p. 014402, 2004.
- [9] F. Ven Den Bogaat and R. Pyndian, "A 10-14 GHz linear MMIC vector modulator with less than 0.1 dB and 0.8 amplitude and phase error," *IEEE MTT-S Int. Symp. Dig.*, pp. 465-468, 1990.
- [10] H. Kamitsuna and H. Ogawa, "Ultra-wideband MMIC active power splitters with arbitrary phase relationships," *IEEE Trans. Microw. Theory Tech.*, vol. 41, no. 9, pp. 1519-1523, Sep. 1993.
- [11] H. Simon and R. Périchon, "A MMIC broad-band 90 power divider using a new all-pass active filter," *Proc. 30th Euro. Microw. Conf.*, pp. 344-347, 2000.
- [12] P. Gay-Balmaz and O. Martin, "Electromagnetic resonances in individual and coupled split ring resonators," *J. Appl. Phys.*, vol. 92, pp. 29-36, 2002.
- [13] J. Baena, R. Marqués, F. Medina, and J. Martel, "Artificial magnetic metamaterial design by using spiral resonators," *Phys. Rev. B*, vol. 69, p. 014402, 2004.
- [14] R. Marqués, F. Medina, and R. Rafii-El-Idrissi, "Role of bi-anisotropy in negative permeability and left handed metamaterials," *Phys. Rev. B*, vol. 65, p. 144441, 2002.
- [15] M. Shamonin, E. Shamonina, V. Kalinin, and L. Solymar, "Resonant frequencies of a split-ring resonator: analytical solutions and numerical simulations," *Microw. Opt. Tech. Lett.*, vol. 44, pp. 133-137, 2005.
- [16] R. Marqués, J. Baena, J. Martel, F. Medina, F. Falcone, M. Sorolla, and F. Martin, "Novel small resonant electromagnetic particles for metamaterial and filter design," *Proc. ICEAA*, Torino, Italy, pp. 439-442, 2003.
- [17] D. Wang, H. Zhang, T. Xu, H. Wang, and G. Zhang, "Design and optimization of equal split broadband microstrip Wilkinson power divider using enhanced particle swarm optimization algorithm," *Progress In Electromagnetics Research*, vol. 118, pp. 321-334, 2011.
- [18] Ansoft High Frequency Structure Simulation (HFSS), ver. 10 Ansoft Corp., 2005.
- [19] M. Abessolo, N. Akin, and A. El Moussaoui, "A new left-handed metamaterial structure based on split-triangle resonators (STRs)," *Applied Computational Electromagnetics Society (ACES) Journal*, vol. 26, no. 11, pp. 945-952, Nov. 2011.
- [20] Z. Lin, and Q.-X. Chu, "A novel approach to the design of dual-band power divider with variable power dividing ratio based on coupled-lines,"

Progress In Electromagnetics Research, PIER 103, pp. 271-284, 2010.

- [21] F. Falcone, E. Jarauta, J. Illescas, I. Arnedo, M. Beruete, T. Lopetegi, M. G.-Laso, J. Marcotegui, and M. Sorolla, "Use of MW studio in the implementation of metamaterial configurations in planar circuit technology," *23th Annual Review of Progress in Applied Computational Electromagnetics (ACES)*, Verona, Italy, pp. 835-840, Mar. 2007.
- [22] D. Jiang, Y. Xu, R. Xu, and W. Lin, "Compact dual-band-notched UWB planar monopole antenna with modified CSRR," *Electronics Letters*, vol. 48, no. 20, pp. 1250-1252, Sep. 2012.
- [23] V. Demir, D. Elsherbeni, D. Kajfez, and A. Elsherbeni, "Efficient wideband power divider for planar antenna arrays," *Applied Computational Electromagnetics Society (ACES) Journal*, vol. 21, no. 3, pp. 318-324, Nov. 2006.



Di Jiang received the B.S. degree in Communication Engineering from the GuiLin University of Electronic Technology (GLIET), China, in 2004, and is currently pursuing the Ph.D. degree in Electromagnetic Field and Microwave Technology at the University of Electronic Science and Technology of China (UESTC), Chengdu, China. His research interest includes miniature antenna, RF circuit, and metamaterial design and its application.



Yuechang Xu received the B.S., M.S., and Ph.D. degree in electromagnetic field and microwave technology from the University of Electronic Science and Technology of China (UESTC), in 2004, 2007, and 2010, respectively. He was a visiting scholar in Columbia University working on graphene RF devices during Sep. 2009 to Sep. 2010. He has been associate professor in UESTC since 2011. His research interests include wide band-gap semiconductor material and graphene based RF devices.



Ruimin Xu received the Ph.D. degree in electrical engineering from the University of Electronic Science and Technology of China (UESTC), Chengdu, China. He is currently a professor and serves as the deputy director of the national defense key discipline laboratory of UESTC. His research interests include microwave and millimeter-wave circuits and systems, microwave monolithic integrated circuit.



Zhenhai Shao was born in Jiangsu Province, China, in December, 1971. He received the B. E. degree from the Nanjing Normal University, Nanjing, China, in 1994, and received the M. S. and Ph. D. degrees from the Southeast University, Nanjing, China, in 1997 and 2000, respectively.

From 2000 to 2001, he was with National University of Singapore as research fellow. From 2001 to 2003, he was with Nanyang Technological University as research fellow. From 2003 to 2006, he was a manager and research scientist in NICT Singapore Wireless Communications Laboratory. From 2006 to 2007, he was Chief Technical officer in Cubic Micro Design Pte Ltd. Currently, he is a professor in University of Electronic Science Technology of China. His research interests include microwave/millimeter-wave subsystem, passive devices and circuits, numerical procedures of FDTD, TLM, TDFEM and DSC method for passive microwave components, software design. He authored about over 100 paper published in international journals and conference proceedings. He is a senior member of IEEE, and has been a reviewer for the IEEE, IET and IEICE.

An Efficient 2D Rough Surface Scattering Analysis Using Strong Harmonics Extraction and the Kirchhoff Approach

A. Torabi and A. A. Shishegar

Department of Electrical Engineering,
Sharif University of Technology, Tehran, Iran
torabi@ee.sharif.edu, shishegar@sharif.edu

Abstract — An efficient method for scattering analysis from slightly rough surfaces is introduced. This method can be used in ray tracing algorithm where the computational efficiency is important due to the complexity and size of problems. In this method, the Kirchhoff approach is used for a periodic extension of the finite surface, which is approximated by strong harmonics of its Fourier series. Typical asphalt surfaces are analyzed by this method in millimeter-wave band and validated with the method of moments. The dominant scattering angles and ray widths of the scattered field can be easily used in ray tracing algorithm. The computation time and accuracy of results show that this method can be used for rough surface scattering analysis in ray tracing algorithm efficiently.

Index Terms - Electromagnetic scattering by rough surfaces, Fourier series, Kirchhoff approach, method of moments, and Ray tracing.

I. INTRODUCTION

The problem of scattering from rough surfaces has been the subject of intensive researches over the past decades. Scattering consideration from these surfaces in ray tracing algorithm is another challenging problem. The existent empirical models have no enough accuracy [1, 2]. Furthermore, accurate numerical analysis of scattering from these surfaces [3, 4], is not practical for use in ray tracing algorithm due to the computational costs.

The Kirchhoff approach is a classical scattering analysis solution based on the tangent plane approximation and is valid for surfaces with

large radii of curvature [5]. This method has an analytical closed-form solution for finite length of a periodic rough surface (finite periodic surface, like $f(x) = \cos(\alpha x)$ for $-L \leq x \leq L$, $L = \pi m / \alpha$, $m = 2, 3, \dots$) [6].

In this paper a novel method is introduced for plane wave scattering analysis from slightly rough surfaces using strong harmonics extraction and the Kirchhoff. The rough surfaces are assumed to be in the validity region of the Kirchhoff approach. The Kirchhoff approach is utilized for the finite periodic surface, which is composed of different harmonics. First, a given rough surface is considered as a period of a periodic surface and is represented by its Fourier series. Then the surface is approximated by its strong harmonics. At last, the Kirchhoff approach is used for computation of scattering from the approximated surface. An important parameter is the number of extracted harmonics, N . Small N makes a big deviation from original rough surface when big N increases the computation time. Typical asphalt surfaces in millimeter-wave band are simulated using this method. Results are compared to the method of moments' results for plane wave incidence using the resistive sheet tapering method [7]. It is shown that extracting enough harmonics leads to a good global conformity to the accurate answer. Closed-form scattering coefficient can efficiently represent the scattered field as a sum of rays, directed to dominant scattering angles. This method can be easily integrated to ray tracing algorithm.

In the next section, Kirchhoff approach for finite periodic surfaces is presented. Section III is about the strong harmonics extraction. In section

IV, numerical results of the scattering computation for slightly rough Gaussian surfaces are shown. The paper is concluded in section V.

II. KIRCHHOFF APPROACH FOR PERIODIC SURFACES

Consider a one dimensional rough surface $z = f(x)$ of length $2L$ as shown in Fig. 1. The normalized scattering coefficient for a plane wave scattering from a rough surface is defined by,

$$\rho = \frac{E_s}{E_{s_0}}, \quad (1)$$

where E_s is the scattered field and E_{s_0} is the field reflected in the specular direction ($\theta_s = \theta_i$) by the same size smooth conducting plane under the same angle of incident.

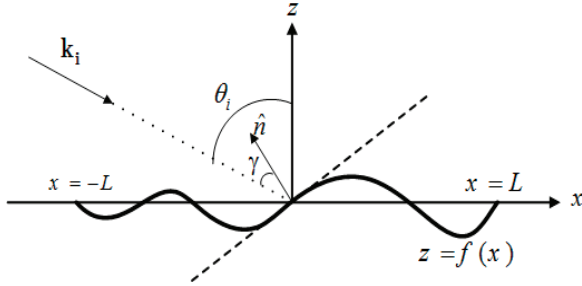


Fig. 1. Rough surface and tangent plane approximation.

For a perfect electric conductor surface, equation (1) has a closed analytic form by using the Kirchhoff approach [6],

$$\rho^\pm(\theta_i, \theta_s) = \pm F(\theta_i, \theta_s) \frac{1}{2L} \int_{-L}^L e^{j\mathbf{v} \cdot \mathbf{r}(x)} dx + \frac{e^\pm(L)}{2L}, \quad (2)$$

$$F(\theta_i, \theta_s) = \sec \theta_i \frac{1 + \cos(\theta_i + \theta_s)}{\cos \theta_i + \cos \theta_s}, \quad (3)$$

$$e^\pm(L) = \frac{j \sec \theta_i \sin \theta^\pm e^{j\mathbf{v} \cdot \mathbf{r}(x)}}{k (\cos \theta_i + \cos \theta_s)} \Big|_{-L}^L \quad (4)$$

$$\theta^+ = \theta_s \quad \theta^- = \theta_i,$$

where + and - denote TE and TM incident, respectively, θ_i , θ_s are incident and scattering angles, k is the wave number, $\mathbf{r}(x) = x\hat{x} + f(x)\hat{z}$

and \mathbf{v} is the difference of incident and scattered wave vectors,

$$\mathbf{v} = v_x \hat{x} + v_z \hat{z} = \mathbf{k}_i - \mathbf{k}_s. \quad (5)$$

The second term in equation (2) is the edge effect. It is negligible for $L \gg \lambda$ if $f(L) = f(-L) = 0$ [6]. Now consider a periodic surface with period Λ (i.e., $f(x) = f(x + \Lambda)$). So in equation (2) exponential term $e^{j\mathbf{v} \cdot \mathbf{r}(x)}$ will be periodic,

$$v_x \Lambda = 2\pi m, \quad m = 1, 2, 3, \dots \quad (6)$$

It is shown that in [6],

$$\sin \theta_{sm} = \sin \theta_i + m \frac{\lambda}{\Lambda}; \quad (m = 0, \pm 1, \dots). \quad (7)$$

Equation (7) is the well-known grating equation. For distinct θ_i , equation (7) is satisfied by specific m . First consider $L = (n + n_1)\Lambda$, where n is an integer and $0 \leq n_1 < 1$. Then, after some simplifications,

$$\rho^\pm(\theta_i, \theta_{sm}) = \pm \frac{F(\theta_i, \theta_{sm})}{2L} \frac{1}{\Lambda} \int_0^\Lambda e^{j\mathbf{v} \cdot \mathbf{r}(x)} dx + \frac{C(n_1)}{2L}, \quad (8)$$

$$C(n_1) = \pm F(\theta_i, \theta_{sm}) \left[\int_{-n_1\Lambda}^{n_1\Lambda} e^{j\mathbf{v} \cdot \mathbf{r}} dx - 2n_1 \int_0^\Lambda e^{j\mathbf{v} \cdot \mathbf{r}} dx \right] + e^\pm(2\pi m n_1 / v_x). \quad (9)$$

The symbol $C(n_1)$ represents the edge effect. For each θ_{sm} there is a lobe around it with half-width of [6],

$$\Delta \theta_{sm} \approx \frac{\lambda}{2L} \sec(\theta_{sm}). \quad (10)$$

Consider a sinusoidal surface, i.e., $f(x) = h \cos Kx$, where $K = 2\pi/\Lambda$ is the phase constant of the surface. Equation (8) yields to [6],

$$\rho^\pm(\theta_i, \theta_{sm}) \approx \pm j^m F(\theta_i, \theta_{sm}) J_m(s), \quad (11)$$

$$s = v_z h = -kh (\cos \theta_i + \cos \theta_{sm}), \quad (12)$$

where θ_{sm} is given by the grating equation (7) for each valid m , and $J_m(s)$ is the m -th order of the first kind Bessel function. This solution leads to some scattering lobes, directed to θ_{sm} angles with half-width of $\Delta \theta_{sm}$.

III. STRONG HARMONICS EXTRACTION FOR RANDOMLY ROUGH SURFACES

In the first step of strong harmonics extraction analysis, the rough surface (Fig. 1), is considered as a period of a periodic function (with period of $\Lambda = 2L$) represented by its Fourier series. This series is a summation of $\alpha_n \cos(nKx)$ and $\beta_n \sin(nKx)$ terms. Consider the first harmonic coefficient of cosine part, α_1 and $N-1$ strongest coefficients among other α_n s and β_n s. The selected harmonics are sorted based on their incremental indices. Now the sorted coefficients are saved in new variables a_n and b_n and their indices are saved in new variables c_n and d_n , respectively. So the approximated rough surface is

$$\begin{aligned} \tilde{f}(x) &= a_1 \cos(Kx) + \sum_{m=2}^{N_1} a_m \cos(c_m Kx) + \\ &\quad \sum_{m=1}^{N_2} b_m \sin(d_m Kx), \\ a_m &= \frac{2}{L} \int_{-L}^L f(x) \cos\left(\frac{n\pi}{L}x\right) dx \\ b_m &= \frac{2}{L} \int_{-L}^L f(x) \sin\left(\frac{n\pi}{L}x\right) dx \\ a_1 &= \alpha_1, \quad K = \frac{2\pi}{\Lambda} = \frac{\pi}{L}, \quad N_1 + N_2 = N. \end{aligned} \quad (13)$$

a_n and b_n can be computed numerically. To drive the closed analytical form of the normalized scattering coefficient, the first harmonic ($\cos(Kx)$) is always kept. It must be notified that equation (13) is an approximation of $z = f(x)$ on its domain, i.e., from $-L$ to L ($\Lambda = 2L$). Applying equation (8) to the approximated surface, equation (13), ignoring the edge effect and after some simplifications, the normalized scattering coefficient becomes (see appendix A),

$$\begin{aligned} \rho(\theta_i, \theta_{sm}) &\approx \pm F_2(\theta_i, \theta_{sm}) \times \sum_{q_1=-\infty}^{\infty} \sum_{q_2=-\infty}^{\infty} \dots \sum_{q_{N_1-1}=-\infty}^{\infty} \\ &\quad \sum_{p_1=-\infty}^{\infty} \sum_{p_2=-\infty}^{\infty} \dots \sum_{p_{N_2}=-\infty}^{\infty} \left[J_{q_1}(s_{N_1}) \times J_{q_2}(s_{N_1-1}) \dots \times \right. \\ &\quad \left. J_{q_{N_1-1}}(s_2) J_{p_1}(w_{N_2}) J_{p_2}(w_{N_2-1}) \dots J_{p_{N_2}}(w_1) \times \right. \\ &\quad \left. J_T(s_1) \times j^D \right], \end{aligned} \quad (14)$$

where

$$s_i = v_z a_i, \quad i = 1, 2, 3, \dots, N_1, \quad (15)$$

$$w_i = v_z b_i, \quad i = 1, 2, 3, \dots, N_2, \quad (16)$$

$$T = m + \sum_{i=1}^{N_1-1} c_{N_1-i+1} q_i + \sum_{i=1}^{N_2} d_{N_2-i+1} p_i, \quad (17)$$

$$\begin{aligned} D &= m + \sum_{i=1}^{N_1-1} q_i + \sum_{i=1}^{N_1-1} c_{N_1-i+1} q_i \\ &\quad + \sum_{i=1}^{N_2} d_{N_2-i+1} p_i, \end{aligned} \quad (18)$$

where v_z is the \hat{z} -component of \mathbf{v} , and m is defined by grating equation (7). Equation (14) is an $(N-1)$ -dimensional series. The Bessel function has intensive decreasing form as its order increases. So the infinite summations of equation (14) can be replaced by the terms of q_i and p_i in $[-M, M]$.

Equation (14) is the closed-form normalized scattering coefficient for the slightly rough perfect conductor surfaces. To use this method in ray tracing algorithm, the scattered field can be assumed as some rays (exactly m rays, where m is given by equation (7)) directed to θ_{sm} with the normalized amplitude given by truncated form of equation (14). So one can choose the dominant angles using an appropriate amplitude threshold and import them in ray tracing algorithm. In the next section we validate this formulation and explain about different parameters of it.

IV. VALIDATION AND RESULTS

To validate the above method, we consider the asphalt surface with roughness parameters of Table I. Both types of considered asphalt surfaces, satisfy the Kirchhoff approach condition for millimeter wave band ($\lambda = 5mm$ and $\lambda = 10mm$) [5]. The formula in equation (14) is for perfect conductor surface, but in millimeter-wave band, one can replace the lossy dielectric surface with perfect conductor as a good approximation because of the small penetration depth [10]. These two Gaussian random surfaces are generated numerically by spectral approach [3]. Without loss of generality, an even extension of each surface is generated. So the coefficients b_m are zero. Extraction of the first harmonic and the strong $N-1$ harmonics is the next step. Table II shows this process and their prominent extracted Fourier

series coefficients. Criterion for approximation is $\Delta \leq 20\%$, where

$$\Delta = \frac{\int_{-L}^L |f(x) - \tilde{f}(x)| dx}{\int_{-L}^L |f(x)| dx}, \quad (19)$$

while $f(x)$ is the original rough surface and $\tilde{f}(x)$ is the approximated surface given by equation (13). An efficient approach to find the dominant coefficients of Fourier series is defining an internal error criterion, which computes the change of Δ in each step of finding a_i (b_i). Then if the evaluated a_i (b_i) satisfy this internal criterion, it means that the derived Fourier coefficient is dominant and it could be kept. Otherwise, that would be ignored. The second step is the calculation of θ_{sm} . Valid θ_{sm} and m could be found by equation (7). By replacing θ_{sm} in equation (14), approximated $\rho(\theta_i, \theta_{sm})$ could be solved for each θ_{sm} . For each θ_{sm} scattering angle, there is a lobe with half-width that is given by equation (10). For validation, the method of moments (MOM) is used [3, 9].

Table I: Asphalt surface parameters [8].

Asphalt surface type	σ (mm)	l_c (mm)
Type1 (slightly rough asphalt)	0.36	≈ 5.2
Type2 (very rough asphalt)	0.7	≈ 5

Table II: Strong harmonics extracted for two asphalt surface for $\Delta \leq 20\%$.

Asphalt surface type	N	$\{a_n\}$	Δ
Type1	4	$\{a_1, a_3, a_4, a_8\}$	18.22%
Type2	5	$\{a_1, a_3, a_8, a_{10}, a_{17}\}$	14.83%

Because in the harmonics extraction method the incident wave is supposed to be a uniform plane wave and the edge effect is ignored, so for validating the results with MOM, uniform plane wave incident must be considered in numerical analysis too. For this goal, resistive sheet tapering method is used [7]. In this method, a relatively small portion of the sample surface is used to suppress the edge currents. Figures 2 and 3 show the normalized scattering coefficient for these two types of asphalt surfaces in two wavelengths

($\lambda = 5\text{mm}$ and 10mm , respectively). θ_i , the incident angle is 30° and $M = 8$ is chosen. It can be seen that for the rougher surface (type 2), scattering in non-specular direction becomes more prominent than the other (type 1). The deviation between the harmonic extraction analysis and MOM results of Figs. 2 and 3 is due to some approximation in deriving the relation in equation (14). But the global behavior of the scattered field pattern has an acceptable conforming to MOM.

The main reason for deviation of the results with MOM is related to this fact that the MOM reported results are related to scattering computation of large number of realizations for desired Gaussian rough surface, which are averaged. Therefore, our method has this ability to follow this average behavior acceptably. One of the error sources is the truncation of the series in equation (14) (value of M) and the other is the number of the extracted harmonics (N in equation (13)). Consider the asphalt surface type 1. Now consider three different scattering angles in Fig. 2 (a); $\theta_s = 30^\circ$, $\theta_s = 11.53^\circ$, $\theta_s = -30^\circ$. Positive angles are in clockwise. For these angles, normalized scattering coefficient for $M = 6, 8, 10$, and 12 are calculated and shown along with the MOM results in Table III. Due to small magnitude of the high order Bessel functions, ignoring the high values of M gives acceptable results. We can see that the differences between $M = 6$ and $M = 8$ are negligible. The results for $M = 10$ and $M = 12$ are the same. It can be concluded that the truncation of series in equation (14) does not cause a big change in the results. Another important error source is the number of the extracted harmonics. Higher N , increases the order of series in equation (14) and consequently the time of the computation process would increase severely.

Table III: $\rho(30^\circ, \theta_{sm})$ for different values of M (truncation effect in series of equation (14)).

M	$\theta_{sm} = 30^\circ$ (MOM : 0.9812)	$\theta_{sm} = 11.53^\circ$ (MOM : 0.0950)	$\theta_{sm} = -30^\circ$ (MOM : 0.0830)
6	0.9655	0.1000	0.1033
8	0.9698	0.1001	0.1044
10	0.9700	0.1002	0.1074
12	0.9700	0.1002	0.1074

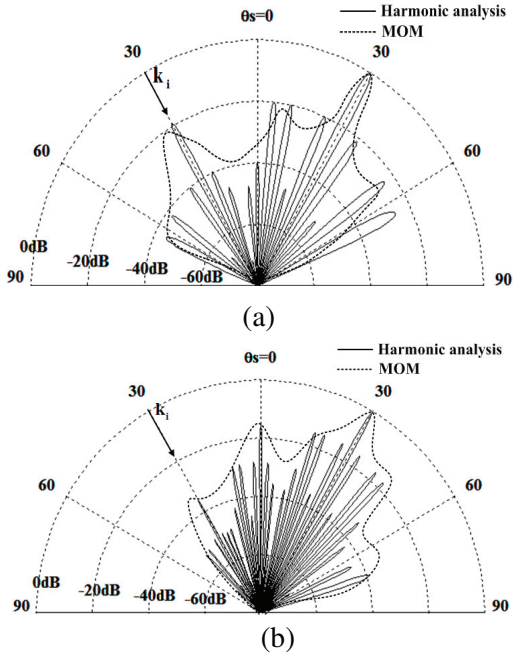


Fig. 2. Strong harmonics extraction analysis for asphalt type 1, $L = 5$ cm (a) $\theta_i = 30^\circ$, $\lambda = 10$ mm and (b) $\theta_i = 30^\circ$, $\lambda = 5$ mm, mean time for MOM is 8 min while for the relation in equation (19) is less than 5 sec.

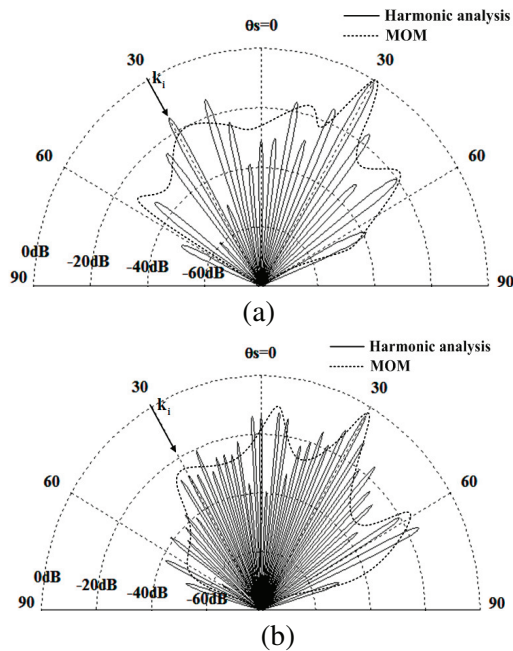


Fig. 3. Strong harmonics extraction analysis for asphalt type 2, $L = 5$ cm (a) $\theta_i = 30^\circ$, $\lambda = 10$ mm and (b) $\theta_i = 30^\circ$, $\lambda = 5$ mm, mean time for MoM is 8 min while for the relation in equation (19) is less than 5 sec.

Figure 4 represents the results for different number of extracted harmonics, $N = 3, 4, 5,$ and 7 , for rough surface of type 1 asphalt. For small N , ($N = 3$), a big error ($\Delta = 30\%$) in the approximation of the original surface resulted a bad conformity to the MOM method. It is obvious that by increasing N , a better answer is achievable (Fig. 4 (b), (c), (d)). By extracting more harmonics to some extent, the accuracy of the method will improve. But extracting more harmonics doesn't make notable change in the global form of the scattering pattern. So it can be seen that approximation with $\Delta \leq 20\%$ gives acceptable converged results. For two surfaces above, 4-5 strong harmonics must be extracted for $\Delta \leq 20\%$ (Table II). Our simulations show that decreasing Δ from 20% to 10% results 2% change in $\rho(\theta, \theta_{sm})$. One can define a threshold for the normalized scattering coefficients to select the dominant scattering angles. These angles show proper rays for ray tracing algorithm. The results are shown in Table IV for a -30dB threshold. Consequently, 6 rays is extracted and listed in Table IV. Apart from the specular direction with dominant amplitude, there are 5 rays, which are above the threshold (-30 dB). The ray width of each ray is also indicated in the following table.

Table IV: Selected scattering angles and the ray widths for threshold of -30dB.

Selected θ_{sm}	53.13°	36.86°	30°	23.57°	11.53°	-30°
$\rho(30^\circ, \theta_{sm})$	-22.2dB	-20.8dB	-0.13dB	-19.5dB	-20.2dB	-21.0dB
$\Delta\theta_{sm}$	9.568°	7.162°	6.589°	6.251°	5.847°	6.589°

V. CONCLUSION

A new method for rough surface scattering analysis for ray tracing algorithm is introduced. This method is enough accurate, computationally efficient and can be integrated well with the ray tracing algorithm. A rough surface is extended to a periodic rough surface first. Then, the surface is approximated by its strong harmonics of the Fourier series. The Kirchhoff approach is used for the approximated surface over a period, i.e., the length of the original rough surface. The scattering pattern in this method can be assumed as a sum of different rays at different angles, called the scattering angles. Using a proper threshold, the dominant rays can be chosen to be used in ray

tracing algorithm. The numerical results show a good global conformity to the results of the method of moments. The method is computationally efficient and can be easily integrated to the ray tracing algorithm.

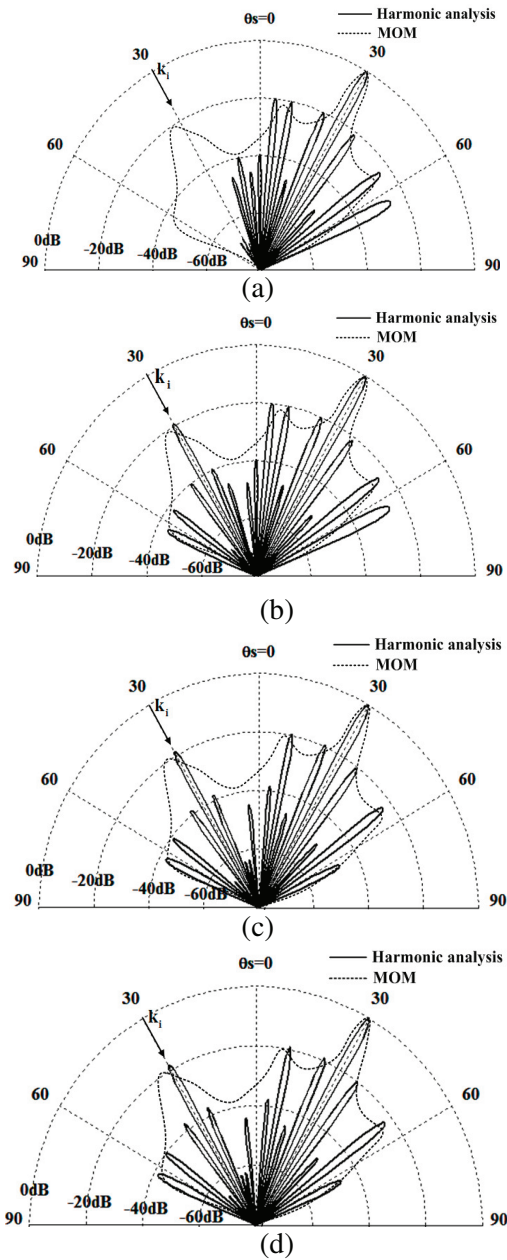


Fig. 4. Strong harmonics extraction analysis for asphalt type 1, $L = 5 \text{ cm}$ (a) $N = 3$ ($\Delta = 30\%$), (b) $N = 4$ ($\Delta = 18.22\%$), (c) $N = 5$ ($\Delta = 10.32\%$), and (d) $N = 7$ ($\Delta = 8.03\%$), mean time for MoM is 8 min while for the relation in equation (19) is 0.2, 0.9, 1.3, and 4.5 sec for $N = 3, 4, 5,$ and $7,$ respectively.

ACKNOWLEDGMENTS

The authors wish to thank Iran Telecommunication Research Center (ITRC) for supporting this research.

APPENDIX A

By replacing the approximated rough surface of equation (13) into equation (8) and ignoring the edge effect,

$$\frac{1}{\Lambda} \int_0^\Lambda e^{jv \cdot r} dx = \frac{1}{\Lambda} \int_0^\Lambda e^{j \left\{ v_x x + v_z \left(a_1 \cos(Kx) + \sum_{m=2}^{N_1} a_m \cos(c_m Kx) + \sum_{m=2}^{N_2} b_m \sin(d_m Kx) \right) \right\}} dx \quad (20)$$

we also have in [11],

$$e^{jx \cos \theta} = \sum_{m=-\infty}^{\infty} j^m J_m(x) e^{jm\theta}, \quad (21)$$

$$e^{jx \sin \theta} = \sum_{m=-\infty}^{\infty} J_m(x) e^{jm\theta}. \quad (22)$$

Using equations (21) and (22) in equation (20) and by replacing $Kx = t$, equation (20) is changed to,

$$\sum_{q_1=-\infty}^{\infty} \sum_{q_2=-\infty}^{\infty} \dots \sum_{q_{N_1-1}=-\infty}^{\infty} \sum_{p_1=-\infty}^{\infty} \sum_{p_2=-\infty}^{\infty} \dots \sum_{p_{N_2}=-\infty}^{\infty} \left[J_{q_1}(s_{N_1}) J_{q_2}(s_{N_1-1}) \dots J_{q_{N_1-1}}(s_2) \times J_{p_1}(w_{N_2}) J_{p_2}(w_{N_2-1}) \dots J_{p_{N_2}}(w_1) \right] \times \int_0^{2\pi} e^{j \left[m + \sum_{i=1}^{N_1-1} c_{N_1-i+1} q_i + \sum_{i=1}^{N_2} d_{N_2-i+1} p_i \right] t + s_1 \cos(t)} dt \quad (23)$$

where s_i and w_i are defined in equations (15) and (16). Then by using another Bessel identity in [11] yield,

$$\frac{1}{2\pi} \int_0^{2\pi} e^{jmt + jv_z h \cos t} dt = j^m J_m(v_z h), \quad (24)$$

in equation (23), relation (14) will be concluded.

REFERENCES

- [1] ITU-R-P.1410, "Propagation data and prediction methods required for the design of terrestrial broadband radio access systems operating in a frequency range from 3 to 60 GHz," 2007.
- [2] W. Ament, "Toward a theory of reflection by a rough surface," *IRE Proc.*, vol. 41, no. 1, pp. 142-146, 1953.

- [3] J. Kong and L. Tsang, *Scattering of Electromagnetic Waves (Numerical Simulations)*, vol. 2, John Wiley & Sons, 2001.
- [4] J. Li, L. X. Guo, and H. Zeng, "FDTD investigation on electromagnetic scattering from two-dimensional layered rough surfaces," *Applied Computational Electromagnetics Society (ACES) Journal*, vol. 25, no. 5, pp. 450-457, May 2010.
- [5] A. Fung, *Microwave Scattering and Emission Models and Their Applications*, Artech House Inc., 1994.
- [6] P. Bekkmann and A. Spizzicino, *The Scattering of Electromagnetic Waves from Rough Surface*, Artech House, 1987.
- [7] Y. Oh and K. Sarabandi, "Improved numerical simulation of electromagnetic wave scattering from perfectly conducting random surfaces," *IEE Proceedings: Microw. Antennas Propag.*, vol. 144, no. 4, pp. 256-260, 1997.
- [8] L. Ibos, et al., "Infrared emissivity measurement device: principle and applications," *Meas. Sci. Technol.*, vol. 17, pp. 2950-2956, 2006.
- [9] R. Harrington, *Field Computation by Moment Methods*, New York: Macmillan, 1968.
- [10] T. Peters, et al., "Simulation of two-dimensional dielectric structures with resistive sheets," *The University of Michigan, Radiation Laboratory*, no. 389055-1-F, 1986.
- [11] M. Abramowitz and I. Stegun, *Handbook of Mathematical Functions*, Washington DC, 1970.

A Compact UWB Band-Pass Filter with Ultra-Narrow Tri-Notch-Band Characteristic

Y. Li¹, W. Li^{1,2}, C. Liu¹, and Qiubo Ye³

¹ College of Information and Communications Engineering,
Harbin Engineering University, Harbin, Heilongjiang 150001, China
liyingsong@ieee.org, liwenxing@hrbeu.edu.cn, liuchengyuan@hrbeu.edu.cn

² Institute of Electromagnetic and Wireless Engineering,
Harbin Engineering University, Harbin, Heilongjiang 150001, China
liwenxing@hrbeu.edu.cn

³ Communications Research Centre, 3701 Carling Ave., Ottawa, K2H 8S2, Canada
qiubo.ye.1997@ieee.org

Abstract — This paper proposes a novel approach for designing compact ultra-wideband (UWB) band-pass filter with a good tri-notch-band characteristic, which is obtained by using the ring-stub multimode resonator (MMR). The equivalent model of the filter is achieved by using odd/even excitation resonance condition. The characteristics of the designed filter are investigated and analyzed by means of IE3D. This filter is designed, analyzed, fabricated, and measured successfully. Experimental and numerical results show that the proposed filter, with compact size of $25 \times 10 \text{ mm}^2$, has an impedance bandwidth range from 3 GHz to 10.6 GHz with the triple notch bands at 4.14 GHz, 6.1 GHz, and 7.1 GHz. The proposed filter can be incorporated into UWB radio systems in order to efficiently enhance the interference immunity from undesired signals.

Index Terms - Multimode resonator, notch band, RF identification (RFID) communication, ring-stub, and UWB filter.

I. INTRODUCTION

Since the Federal Communications Commission (FCC) released the frequency band from 3.1 GHz to 10.6 GHz for commercial ultra-wideband (UWB) communication applications in February 2002, the radio system has been

receiving great attention from academic, governmental and industrial field [1]. An UWB band-pass filter (BPF) is one of the key passive components to realize a UWB radio system. Therefore, a number of demands have been placed on the design of BPFs with large fractional bandwidths (FBWs). Recently, many efficient methods and viable structures have been proposed to develop UWB various BPFs [2-5]. The typical structures, including a low and high-pass filter configuration [2], coplanar waveguide (CPW) forms [3], right/left-handed structure [4], multimode resonator (MMR) [5], have been proposed and investigated. Although, most of these UWB BPFs are suitable for practical use, they still have some drawbacks, such as smooth out-of-band rejection performance and complex structures.

In addition, the UWB frequency band overlaps with the existing narrowband communication systems, which means that those radio signals may interfere with UWB systems and vice versa. To reduce the potential interference, a compact communication system, which operates in UWB frequency band requires a small BPF with a notched band characteristic in order to avoid being interfered by the undesired radio signals. Recently, many methods have been investigated to design an UWB BPF with a notched band, such as embedded open-circuited stub [6], defected ground

structures (DGS) [7], mismatch transmission line [8], parasitic coupled line [9] and E-shaped microstrip stepped impedance resonator (SIR) [10], which can effectively suppress undesired radio signals. Nevertheless, they are still large in size [6], not compatible with monolithic microwave integrated circuits (MMIC) [7], complex structure [8], and cannot provide multi-notch-band [6-10], such as tri-notch-band.

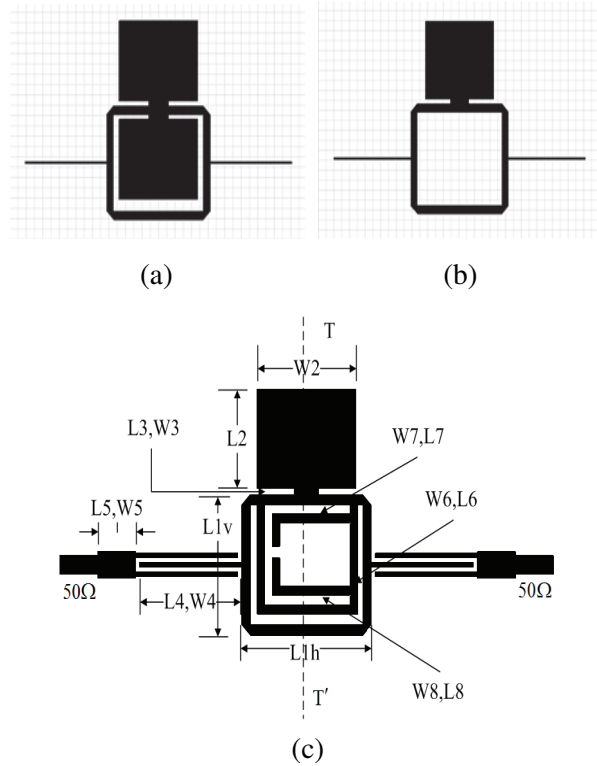
We propose a novel approach for designing compact UWB band-pass filter with a good tri-notch-band characteristic in this paper. The proposed tri-notch-band characteristic is obtained by using the ring-stub multi-mode resonator (MMR), and the central frequencies of these notch bands are 4.14 GHz, 6.1 GHz, and 7.1 GHz, respectively, so that the designed UWB filter can be used for 3.5 GHz WiMAX, 5.5 GHz WLAN, and 6.8 GHz RFID communication applications. The middle ring-stub MMR is analyzed by using odd and even mode. By using this method, we can get the whole resonance condition of the MMR. Compared to the previous UWB notch-band filters in [7-12], the tri-notch-band realized in the proposed filter can be operated simultaneously. The performance of the filter is simulated by using the IE3D software and implemented on the substrate with a relative dielectric constant of 6.15 and a thickness of 0.635 mm. Simulated and measured results agree reasonably well.

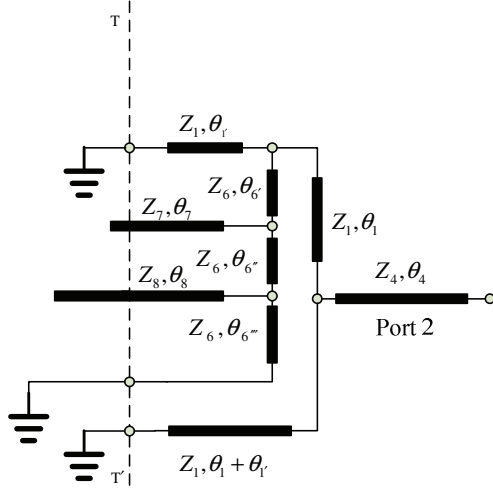
II. FILTER GEOMETRY

The proposed BPF is a modified form of the UWB ring resonator BPF presented in [13]. The configuration of the prototype UWB filter in [13] is shown in Fig. 1 (a). Next, we construct a simplified filter, which is illustrated in Fig. 1 (b). Then, several folded stubs are inserted into the middle ring resonator of the simplified filter to generate the desired tri-notch-band characteristic, and the configuration of our proposed triple band-notched UWB filter is shown in Fig. 1 (c). This filter is printed on a RT/Duroid 6006 with a dielectric constant of 6.15 and a thickness of 0.635 mm. The proposed filter is composed of two interdigital hairpin resonator units, a middle ring-stub MMR, folded stubs and two 50 Ω SIR-fed structures.

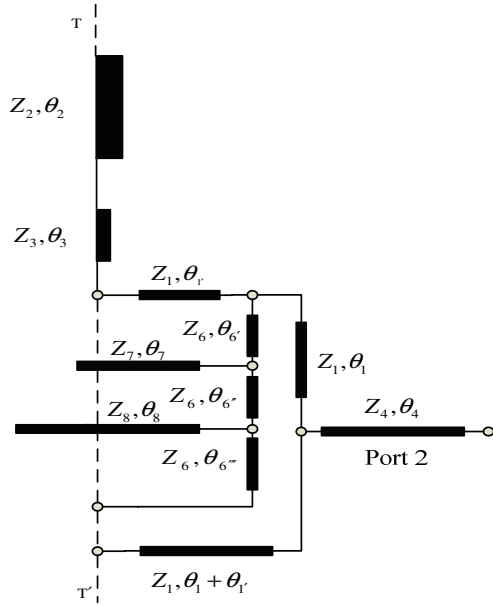
To simplify the analysis process, the odd-even-mode method is employed to analyze the proposed filter, which is also referred to the

articles [14-15]. Figure 2 shows the equivalent transmission line model of the proposed UWB filter with triple notch bands. The proposed transmission-line circuit model shown in Fig. 2 can be illustrated in Fig. 3 by using the odd-even-mode method with T-T' as the reference plane. Since $\theta_4 = \theta_1 + \theta_1 = \pi/4$, we use this known condition to simplify the designed filter structure.



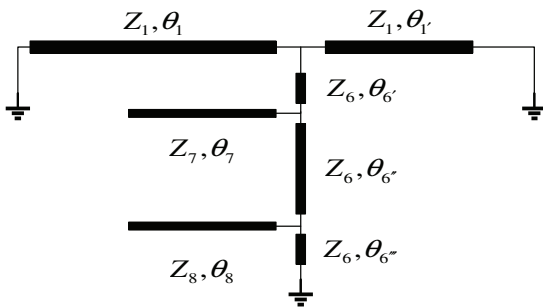


(a) odd-mode

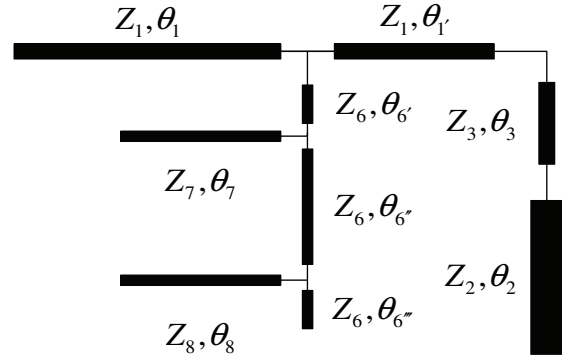


(b) even-mode

Fig. 3. Equivalent transmission line model of the proposed UWB filter with odd/even modes.



(a) odd-mode



(b) even-mode

Fig. 4. Simplified equivalent transmission line model of the proposed UWB filter for odd and even modes.

The equivalent transmission line model of the proposed UWB filter shown in Fig. 3 is simplified and shown in Fig. 4. The input admittance Y_{inodd} of the odd-mode resonator and Y_{ineven} of the even-mode resonator are expressed as follows,

$$Y_{inodd} = \frac{\frac{\tan \theta_1}{Z_1} + \frac{\frac{\tan \theta_{6c}}{Z_6} + \Delta}{1 - Z_6 \tan \theta_{6c} \Delta} + \frac{\cot \theta_{1'}}{Z_1}}{1 - Z_1 \tan \theta_1 \left(\frac{\frac{\tan \theta_{6c}}{Z_6} + \Delta}{1 - Z_6 \tan \theta_{6c} \Delta} + \frac{\cot \theta_{1'}}{Z_1} \right)} \quad (1)$$

where

$$\Delta = \frac{\frac{\tan \theta_7}{Z_7} + \frac{\left(\frac{\tan \theta_{6c}}{Z_6} + \frac{\cot \theta_{6c}}{Z_6} - \frac{\tan \theta_8}{Z_8} \right)}{1 - Z_6 \tan \theta_{6c} \left(\frac{\cot \theta_{6c}}{Z_6} - \frac{\tan \theta_8}{Z_8} \right)}}{\frac{\tan \theta_7}{Z_7} + \frac{\left(\frac{\tan \theta_{6c}}{Z_6} + \frac{\cot \theta_{6c}}{Z_6} - \frac{\tan \theta_8}{Z_8} \right)}{1 - Z_6 \tan \theta_{6c} \left(\frac{\cot \theta_{6c}}{Z_6} - \frac{\tan \theta_8}{Z_8} \right)}}$$

The resonance condition can be achieved at $R_{inodd} = 0$ then we have,

$$1 - Z_1 \tan \theta_1 \left(\frac{\frac{\tan \theta_{6c}}{Z_6} + \Delta}{1 - Z_6 \tan \theta_{6c} \Delta} + \frac{\cot \theta_{1'}}{Z_1} \right) = 0.$$

Because θ_{6c} is very small, then $\theta_{6c} \rightarrow 0$ and $\tan \theta_{6c} \rightarrow 0$. So the resonance condition can be simplified as,

$$1 - Z_1 \tan \theta_1 \left(\Delta + \frac{\cot \theta_1}{Z_1} \right) = 0.$$

Furthermore, $\theta_1 \approx \theta_1$, $\theta_{6'} \approx 2\theta_{6''}$. Thus, the resonance condition can be simplified as, $\tan \theta_7 = 0$ and $\tan \theta_{6'} + \cot \theta_{6''} - \tan \theta_8 = 0$. Thus, we have,

$$Y_{in\text{even}} = \frac{\frac{\tan \theta_1 + \Psi}{Z_1}}{1 - \tan \theta_1 Z_1 \Psi} \quad (2)$$

where

$$\Psi = \frac{\frac{\tan \theta_6}{Z_6} + \frac{\tan \theta_7}{Z_7} + \frac{\left(\frac{\tan \theta_{6'}}{Z_6} + \frac{\tan \theta_{6''}}{Z_6} + \frac{\tan \theta_8}{Z_8} \right)}{1 - Z_6 \tan \theta_6 \left(\frac{\tan \theta_{6'}}{Z_6} + \frac{\tan \theta_8}{Z_8} \right)}}{1 - Z_6 \tan \theta_6 \left[\frac{\tan \theta_7}{Z_7} + \frac{\left(\frac{\tan \theta_{6'}}{Z_6} + \frac{\tan \theta_{6''}}{Z_6} + \frac{\tan \theta_8}{Z_8} \right)}{1 - Z_6 \tan \theta_6 \left(\frac{\tan \theta_{6'}}{Z_6} + \frac{\tan \theta_8}{Z_8} \right)} \right]} + \frac{\frac{\tan \theta_1}{Z_1} + \frac{\left(\frac{\tan \theta_3}{Z_3} + \frac{\tan \theta_2}{Z_2} \right)}{1 - \frac{Z_3}{Z_2} \tan \theta_3 \tan \theta_2}}{1 - \tan \theta_1 Z_1 \left(\frac{\tan \theta_3}{Z_3} + \frac{\tan \theta_2}{Z_2} \right)}.$$

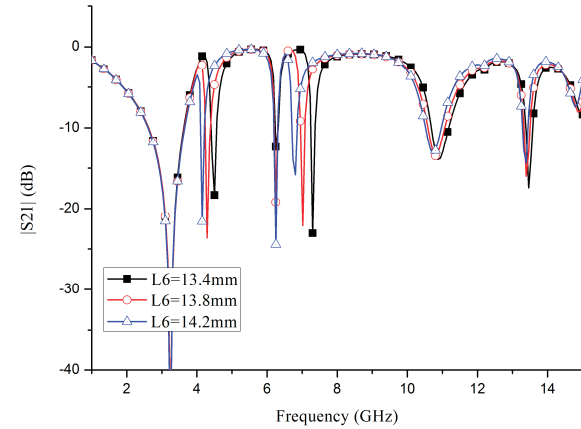
The resonance condition can be achieved at $Y_{in\text{even}} = 0$. Because $\theta_{6'}$ is very small, then $\theta_{6'} \rightarrow 0$ and $\tan \theta_{6'} \rightarrow 0$. Ψ can be simplified as,

$$\Psi = \frac{\frac{\tan \theta_7}{Z_7} + \frac{\left(\frac{\tan \theta_{6''}}{Z_6} + \frac{\tan \theta_{6''}}{Z_6} + \frac{\tan \theta_8}{Z_8} \right)}{1 - Z_6 \tan \theta_6 \left(\frac{\tan \theta_{6''}}{Z_6} + \frac{\tan \theta_8}{Z_8} \right)}}{\frac{\tan \theta_1}{Z_1} + \frac{\left(\frac{\tan \theta_3}{Z_3} + \frac{\tan \theta_2}{Z_2} \right)}{1 - \frac{Z_3}{Z_2} \tan \theta_3 \tan \theta_2}} + \frac{\left(\frac{\tan \theta_3}{Z_3} + \frac{\tan \theta_2}{Z_2} \right)}{1 - \tan \theta_1 Z_1 \left(\frac{\tan \theta_3}{Z_3} + \frac{\tan \theta_2}{Z_2} \right)}.$$

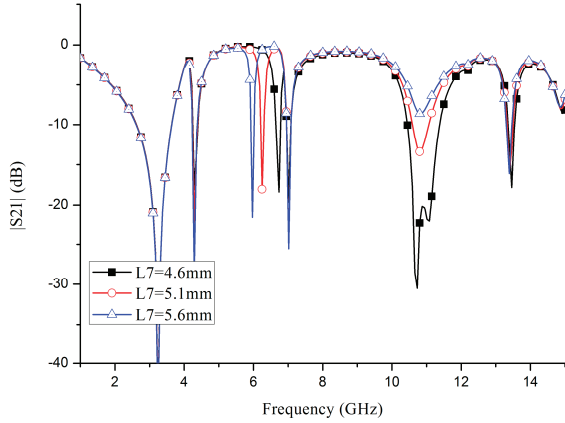
Here, $\theta_{6'} \approx 2\theta_{6''} \rightarrow \pi$, then we have $\theta_{6''} \rightarrow \frac{\pi}{2}$

and $\tan \theta_{6''} \rightarrow \infty$. In this case, $Y_{in\text{even}} = 0$ is impossible. So the resonance condition is $\tan \theta_7 = 0$ and $\tan \theta_{6'} + \cot \theta_{6''} - \tan \theta_8 = 0$. Above all, L7 is designed to control the center frequency of one notch band independently and L8/L6 are designed to adjust the center frequencies of the others notched bands.

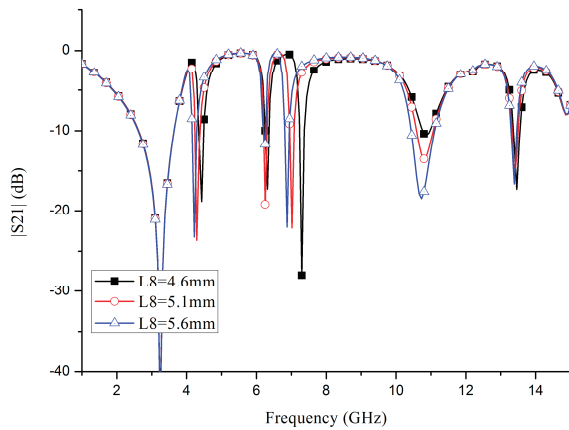
The frequency characteristics of the ring-stub multi-mode resonator are simulated by using IE3D as shown in Fig. 5. f_L , f_M and f_U denote the central frequencies of the lower, middle, and upper notched bands, respectively. It can be seen from Fig. 5 (a) that L6 has important effects on f_L and f_U while f_M remains constant. It can be seen from Fig. 5 (b) that L7 changes the center frequency of f_M . With the increase of L7, the center frequency of the middle notch band moves to the lower frequency. So, we can control the middle notch band by adjusting the dimension of L7. According to the Fig. 5 (c), we can see that L8 has important effect on f_U , which changes dramatically by tuning L8. Based on the discussions above, firstly f_L was designed by tuning the structure parameters (such as L6 and L8), and then f_M was designed by, adjusting L7. Finally, f_U was chosen by adjusting L6 and L8. The required three resonant frequencies of the notched bands can be simultaneously obtained by choosing the proper dimensions of the middle ring-stub multi-mode resonator and the stubs.



(a) Variation of insertion loss with parameter L6.



(b) Variation of insertion loss with parameter L7.



(c) Variation of insertion loss with parameter L8.

Fig. 5. Simulated insertion loss of the proposed asymmetric structure for varying parameters.

III. RESULTS AND DISCUSSION

In this paper, geometric parameters of the filter were adjusted and optimized by means of IE3D. Optimal parameters of the tri-notch-band UWB filter are listed in Table I. To verify the effectiveness of the proposed filter, the filter with tri-notch-band is fabricated and measured. The fabricated filter is shown in Fig. 6. The performance of the proposed filter is measured by using Anritsu 37347D vector network analyzer. Figures 7 and 8 demonstrate the frequency responses of proposed tri-notch-band UWB band-pass filter. Here, only S_{11} is adopted to analyze the proposed filter since the size of this filter is very small. The measured results agree well with the simulated results which help to verify the accuracy of the simulation. The differences

between the simulated and measured values may be due to the errors of the manufactured filter. The fabricated filter has a measured pass-band from 3 GHz to 10.6 GHz, while the center frequencies of the notched bands are 4.14 GHz, 6.1 GHz, and 7.1 GHz. The group delays are shown in Fig. 9, 0.2 ns and 0.6 ns at the mid-band frequency of lower pass-band and at the mid-band frequency of upper pass-band, respectively. It should be noted that the ring-stub MMR can generate three notched band at the desired frequency with no significant influence on the wide pass-band performance of the filter. In a word, the proposed UWB BPF has a good tri-notch-band characteristic for implementing the functions of UWB radio system.

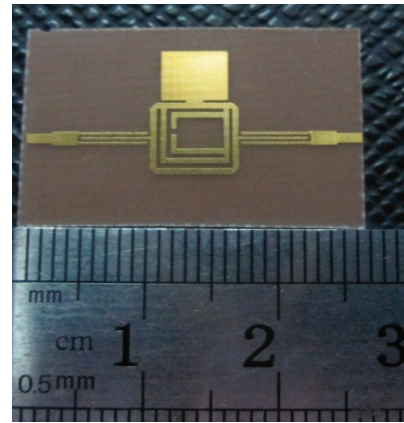


Fig. 6. The photo of the proposed tri-notch band UWB filter.

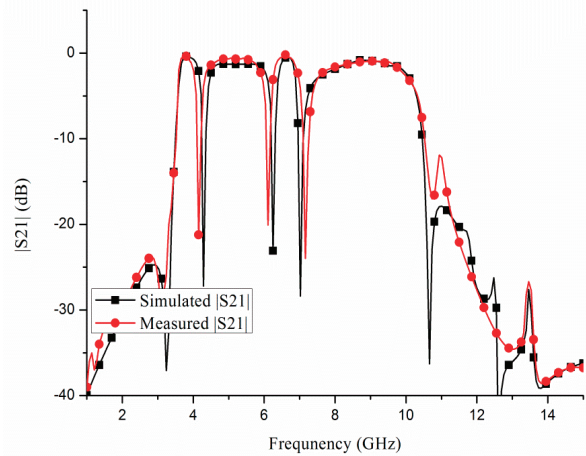
Fig. 7. Comparison between simulated and measured results for $|S_{21}|$ of the fabricated filter.

Table I: Dimensions of the proposed tri-notch band UWB filter.

Dimensions of the proposed tri-band filter (unit: mm)			
PARAMETER	SIZE	PARAMETER	SIZE
L1v	5.12	W1	0.46
L1h	5.92	W2	5.2
L2	4.25	W3	1.3
L3	0.25	W4	0.11
L4	5.39	W5	1.15
L5	2	W6	0.4
L6	3.8	W7	0.4
L7	5.1	W8	0.4
L8	5.1		

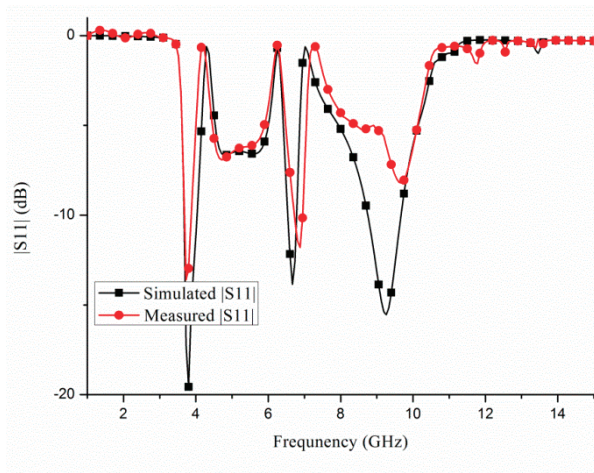


Fig. 8. Comparison between simulated and measured results for $|S_{11}|$ of the fabricated filter.

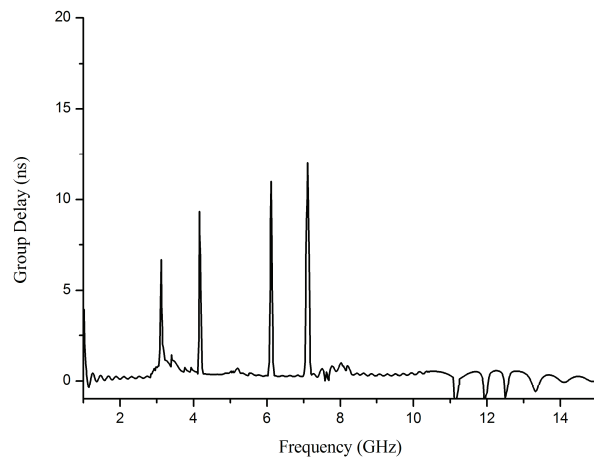


Fig. 9. Group delay of the fabricated filter.

IV. CONCLUSION

In this article, a compact UWB band-pass filter with an ultra-narrow tri-notch-band characteristic has been developed and manufactured. Inserting ring-stub MMR to the original UWB BPF leads to blocking undesired existing radio signals. The ring-stub multi-mode resonator can generate three narrow notched bands corresponding to the undesired radio signal frequencies with no significant influence on the wide pass-band performance of the filter. The measured results show that the proposed filter can cover the entire UWB band with three notch bands. The proposed filter is promising for using in UWB systems due to its simple structure, compact size, and excellent performance.

ACKNOWLEDGMENT

This work was supported by a grant from the National Defense “973” Basic Research Development Program of China (No. 6131380101). This paper is also supported by the National Nature Science Fund of China (No. 60902014), Nature Science Fund of Heilongjiang (QC2009C66) and the Fundamental Research Funds for the Central Universities (HEUCF1304). The authors are also thankful to Hebei VSTE Science and Technology Co., Ltd. for providing the measurement facility.

REFERENCES

- [1] FCC, *Revision of Part 15 of the Commission's Rules Regarding Ultra-Wideband Transmission Systems*, Federal Communications Commission, Tech. Rep. ET-Docket 98-153, FCC02-48, Apr. 2002.
- [2] C.-L. Hsu, F.-C. Hsu, and J.-T. Kuo, “Microstrip bandpass filters for ultra-wideband (UWB) wireless communications,” in *IEEE MTT-S International*, Long Beach, CA, pp. 679-682, 2005.
- [3] H. Wang, L. Zhu, and W. Menzel, “Ultra-wideband bandpass filter with hybrid microstrip/CPW structure,” *IEEE Microwave Wireless Compon. Lett.*, vol. 15, pp. 844-846, 2005.
- [4] J.-Q. Huang and Q.-X. Chu, “Compact UWB bandpass filter utilizing modified composite right/left-handed structure with cross coupling,” *Progress In Electromagnetics Research*, PIER vol. 107, pp. 179-186, 2010.
- [5] B. Yao, Y. Zhou, Q. Cao, and Y. Chen, “Compact UWB bandpass filter with improved upper-stopband performance,” *IEEE Microwave and*

- Wireless Components Lett.*, vol. 19, no. 1, pp. 27-29, Jan. 2009.
- [6] H. Shaman and J. Hong, "Ultra-wideband (UWB) bandpass filter with embedded band notch structures," *IEEE Microw. Wireless Compon. Lett.*, vol. 17, no. 3, pp. 193-195, Mar. 2007.
- [7] L. Chen, Y. Shang, and Y. Zhang, "Design of a UWB bandpass filter with a notched band and wide stopband," *Microw. J.*, vol. 52, no. 11, pp. 96-105, Nov. 2009.
- [8] T. Jiang, C. Liu, Y. Li, and M. Zhu, "Research on a novel microstrip UWB notch-band BPF," in *Proc. APMC*, pp. 261-264, 2009.
- [9] S. Pirani, J. Nourinia, and C. Ghobadi, "Band-notched UWB BPF design using parasitic coupled line," *IEEE Microwave and Wireless Components Lett.*, vol. 20, no. 8, pp. 444-446, August 2010.
- [10] Y.-L. Wu, C. Liao, and X.-Z. Xiong, "A dual-wideband band pass filter based on E-shaped microstrip SIR with upper-stopband performance," *Progress In Electromagnetics Research, PIER* vol. 108, pp. 141-153, 2010.
- [11] S. Gao, S. Xiao, and J. Li, "Compact ultra-wideband (UWB) bandpass filter with dual notched bands," *Applied Computational Electromagnetics Society (ACES) Journal*, vol. 27, no. 10, pp. 795-800, Oct. 2012.
- [12] C. Liu, Y. Li, and J. Zhang, "A novel UWB filter with WLAN and RFID stop-band rejection characteristic using tri-stage radial loaded stub resonators," *Applied Computational Electromagnetics Society (ACES) Journal*, vol. 27, no. 9, pp. 749-758, Sep. 2012.
- [13] C. Kim and K. Chang, "Ultra-wideband (UWB) ring resonator band-pass filter with a notched band," *IEEE Microwave and Wireless Components Lett.*, vol. 21, no. 4, pp. 206-208, 2011.
- [14] H.-W. Wu and Y.-F. Chen, "New compact ultra wideband bandpass filter using modified multi-mode resonator," *AEU-International Journal of Electronics and Communications*, vol. 66, no. 12, pp. 1021-1025, 2012.
- [15] H.-W. Wu and Y.-F. Chen, "Ultra wide band bandpass filter with dual-notched bands using stub-loaded rectangular ring multi-mode resonator," *Microelectronics Journal*, vol. 43, pp. 257-262, 2012.



Yingsong LI received his B.S. degree in Electrical and Information Engineering in 2006, and M.S. degree in Electromagnetic Field and Microwave Technology from Harbin Engineering University, 2006 and 2011, respectively. Now

he is a Ph.D. Candidate in Harbin Engineering University, China. He is a student member of Chinese Institute of Electronics (CIE), IEEE, IEICE and The Applied Computational Electromagnetics Society (ACES). He serves as reviewers for many international journals. He is also a guest editor of "Small Antennas: Miniaturization Techniques and Applications" in International Journal of Antennas and Propagation. His recent research interests are mainly in microwave theory, small antenna technologies, microwave filter designs and computational electromagnetics.



Wenxing LI received the B.S. and M.S. degrees from Harbin Engineering University, Harbin, Heilongjiang, China, in 1982, 1985, respectively. He is currently a full professor of College of Information and Communication Engineering, Harbin Engineering University, China. He is also the head of Research Centre of EM Engineering & RF Technology. He visited the Department of Electrical Engineering, The Pennsylvania State University, USA from June to August 2010. And he visited Oriental Institute of Technology, Taiwan from August to October, 2010. He is also the organizer of the 30th Progress in Electromagnetics Research Symposium (PIERS), IEEE International Workshop on Electromagnetics (iWEM), TPC of 2012 Asia-Pacific Symposium on Electromagnetic Compatibility (APEMC 2012) and 2012 Global Symposium on Millimeter Waves (GSMM 2012). His recent research interests are mainly in computational electromagnetic, microwave engineering, modern antenna design and microwave and millimeter wave circuits.



Chengyuan LIU received his B.S. degree in Electrical and Information Engineering, and M.S. degree in Electromagnetic Field and Microwave Technology from Harbin Engineering University, 2006 and 2011, respectively. Now he is a Ph.D. Candidate in Harbin Engineering University, China. He serves as receivers for the Journal of Electromagnetic Waves and Applications, Journal of Microwaves, Optoelectronics and Electromagnetic Applications, and Progress in Electromagnetics Research Series, Journal of Electromagnetic Waves and Applications. His research interests are mainly in microwave theory, UWB antenna and UWB filters.



Qiubo Ye received the B. S. degree from Hefei University of Technology, Hefei, Anhui, China, the M. S. degree from North China Electric Power University, Beijing, China, and the Ph. D. from the University of Manitoba, Winnipeg, Canada, all in Electrical Engineering. He was a R&D Engineer at Zeland Software (IE3D), Inc. from 2000 to 2001 and a Visiting Assistant Professor of Rose-Hulman Institute of Technology from 2001 to 2002. He joined the Communications Research Centre (CRC) Canada in 2002 as Project Leader & Research Scientist. Currently, he is Research Scientist at the CRC, an Adjunct Professor in Electronics Department, Carleton University, Ottawa, Canada and a Guest Professor of Harbin Engineering University, Harbin, China. He was the Chair of IEEE EMC-S Standards Education & Training Committee (SETCom) from 2006-2012. He is an author and co-author of many scientific papers as well as a book named “Numerical Methods for Electromagnetic Scattering by Large Structures: from Progressive Numerical Method to Projection Iterative Method”. He received Outstanding Engineer Award in 2013 and Outstanding Volunteer Award in 2011 from IEEE Ottawa Section. He was involved in organizing several international conferences as TPC member, publicity Chair, paper award committee member, etc. He is the chair of IASTED International Conference on Wireless Communications in 2011. He has been elected General Chair for IEEE International EMC Symposium 2016. His research interests include electromagnetic simulation for wireless and semiconductor product design, UWB antennas, EMC/EMI, etc.

Microstrip Patch Antenna Covered With Left Handed Metamaterial

E. Dogan¹, E. Unal¹, D. Kapusuz¹, M. Karaaslan¹, and C. Sabah²

¹Department of Electrical and Electronics Engineering
University of Mustafa Kemal, Iskenderun 31040, Hatay, Turkey
esradogan0688@gmail.com, eunal@mku.edu.tr, dilekkapusuz@gmail.com, mkaraaslan@mku.edu.tr

²Department of Electrical and Electronics Engineering, Middle East Technical University – Northern
Cyprus Campus, Kalkanli, Guzelyurt, TRNC / Mersin 10, Turkey
sabah@metu.edu.tr

Abstract — We present gain characteristics of microstrip patch antennas covered with metamaterial substrate composed of split-ring resonators (SRRs) and metallic strip. To determine the performance of the SRR-metallic strip mounted on microstrip patch antenna, the metamaterial has been proposed as an effective medium with extracted constitutive parameters. Simulation results are supported by experimental measurements. The experimental results confirm that the metamaterial covered patch antenna improves gain by an amount of -5.68 dB (60.3%) as well as radiation pattern (-8 dB to +20 dB) at WLAN communication.

Index Terms - Effective parameters, FDTD, gain, patch antenna, metamaterial, and split ring resonator.

I. INTRODUCTION

Microstrip patch antenna is one of the most commonly used antenna in portable communication devices due to compact, conformal, low cost, and ease of fabrication properties. Although, it offers many advantages as mentioned, it has some disadvantages, which result from conductor and dielectric losses. Beside this, gain reduction and poor directionality are also observed in this antenna due to surface waves [1]. Conductor and dielectric losses can be minimized by using better conducting metal and low loss dielectric substrate, but these choices result in higher fabrication cost. Gain, bandwidth enhancement, miniaturization, and broadband

directionality can be provided by using metamaterial structures [2-6]. Metamaterials are manmade structures designed to have properties that may not be found in nature. These structures have both negative effective permittivity and permeability at the same frequency range. It causes negative effective refractive index in the structure [7]. These properties of metamaterial provide novel application opportunities to several disciplines, such as microwave and optical cloaking, focusing of images, and sensing of biological and chemical substances.

Metamaterials have also many application areas for novel antenna systems [8-11]. One of the applications of metamaterials is miniaturization of the microstrip antennas with different types of artificial materials. The conventional way to reduce the antenna size is to use high permittivity substrate. This approach reduces the wavelength of the signal in the substrate [12]. But, this design results in more energy consumption due to high permittivity, since it decreases the bandwidth of the antenna impedance. One another way is to remove the substrate to minimize the effective dielectric constant. This application restricts the wave to travel in the substrate, hence, improving the gain of the patch antenna has been possible [13, 14]. However, the maximum gain enhancement does not exceed 2 dB with all these techniques and the directionality also does not change too much. Hence, many different solutions are proposed to overcome these problems, such as utilization of metamaterials with patch antenna [15-18].

This article describes a novel way to enhance both the gain and directionality of patch antenna used for WLAN application. Split ring resonators (SRR) for negative permeability and metal strip for negative permittivity are used to improve both gain and directionality of patch antenna. The effective permittivity of strip and permeability of SRR are evaluated by both finite element method (FEM) based high frequency structure simulator (HFSS) and finite difference time domain method (FDTD) based computer simulation technique (CST). The dimensions of the inclusions are optimized to realize negative values of the constitutive parameters at the operating frequency of antenna. The SRRs and metal strips are fabricated with optimum dimensions to provide negative constitutive parameters at 2.4 GHz. The fabricated metamaterial is mounted on microstrip patch antenna to observe the effects on it. The measurement results are in good agreement with simulated values. It has been noticed that the metamaterial considerably enhances the gain of the patch antenna.

II. METAMATERIAL DESIGN AND CONSTITUTIVE PARAMETERS

Figure 1 illustrates the front and back side of metamaterial structure, which consists of both circular split ring resonator (SRR) and metallic strip (MS). The combination structure is designed on two sides of 10 mm × 10 mm × 1.6 mm FR4-epoxy ($\epsilon = 4.4$, $\mu = 1$, and dielectric loss tangent $\delta\epsilon = 0.02$). While the SRR produce magnetic material-like responses and exhibit negative permittivity the MS acts as strong dielectric and exhibits negative permeability [19].



Fig. 1. Front and back view of metamaterial.

All the dimensions of the SRR and MS are optimized by HFSS to achieve negative

permittivity and permeability at 2.4 GHz. The TEM wave is applied to the metamaterial. E field is applied parallel to the MS and H field is applied normal to the plane of SRR. It means that the system is a direction dependent. The periodicity of one unit cell with SRR-MS is obtained by assigning perfectly electric conductor-PEC (side normal to E field) or perfectly magnetic conductor- PMC (side normal to H field) to the sides of the unit cell. The constitutive parameters are evaluated from scattering parameters (S_{11} and S_{21}) by using Nicolson Ross Weir (NRW) approximation [20, 21],

$$z = \sqrt{\frac{(1+S_{11})^2 - S_{21}^2}{(1-S_{11})^2 - S_{21}^2}} \quad (1)$$

$$n = \frac{j}{k_0 d} \ln \left(\frac{S_{21}}{1-S_{11} \frac{z-1}{1+z}} \right), \quad (2)$$

$$\epsilon_{\text{eff}} = n/z; \mu_{\text{eff}} = n.z \quad (3)$$

where z , d , and k_0 represent impedance, thickness of the metamaterial and free space wave number, respectively. The effective permittivity, permeability and refractive index are denoted by ϵ_{eff} , μ_{eff} , and n , respectively. The simulations are realized up to 6 GHz. All of the electromagnetic constitutive parameters are negative at 2.4 GHz. Hence, this structure can be used as negative refractive index metamaterial with patch antenna operating at this frequency as shown in Fig. 2.

Microstrip patch antenna is fabricated to operate at frequency range in which permittivity and permeability of metamaterial utilized with this antenna are negative. In this study, the frequency of 2.4 GHz is chosen for the operating frequency of microstrip patch antenna of which specifications are shown in Table I.

Table I: Dimensions of patch antenna on FR4 laminate.

Parameter	Magnitude	Unit
Operating frequency	2.4	GHz
Patch length(L)	59	mm
Patch Width(W)	42.4	mm
Laminate length (Lg)	75	mm
Feed	coaxial	-
Laminate Thickness	1.6	mm

The microstrip patch antenna is fabricated on an FR4 substrate ($\epsilon = 4.4$, $\mu = 1$, and dielectric loss tangent $\delta\epsilon = 0.02$).

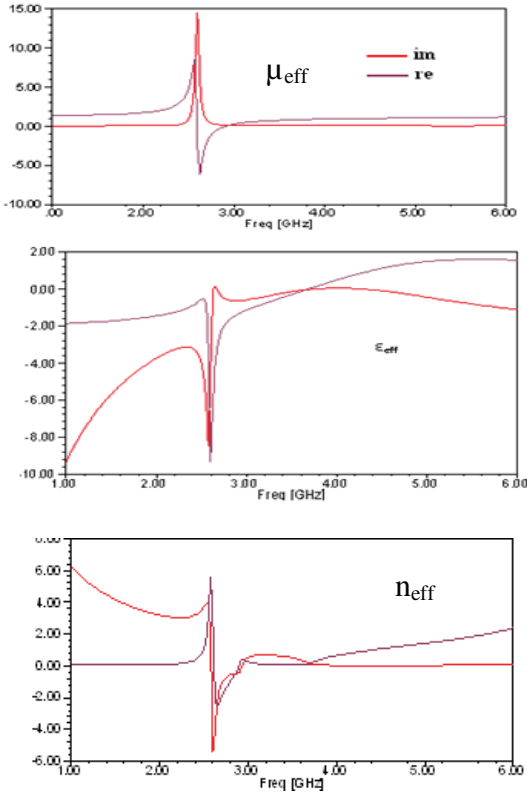
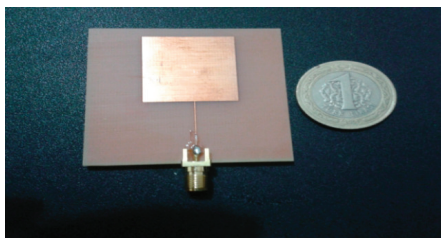


Fig. 2. Effective parameters of metamaterial.

The evaluated results are obtained by HFSS and CST simulators and measured results of microstrip patch antenna without metamaterial are shown in Fig. 3. Return loss measurement is realized by using ENA series network analyzer (E5071B). While return loss (gain value), S_{11} value, of patch antenna is -13.68 dB in HFSS and -16.64 dB in CST, measured value is only -9.42 dB. The difference between measured and simulated values of antenna results from measurement mistakes and fabrication process.



S_{11}	HFSS	CST	Measurement
Patch Antenna	-13.68dB	-16.64 dB	-9.42 dB

Fig. 3. Microstrip patch antenna without metamaterial and return losses in dB.

Effect of the metamaterial to return loss of the microstrip patch antenna is investigated by placing metamaterial on it. The SRR-MS structure is fabricated to obtain negative constitutive parameters at 2.4 GHz and it is periodically mounted on microstrip antenna as shown in Fig. 4.

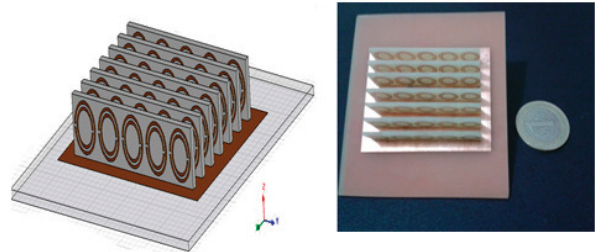


Fig. 4. Fabrication of patch antenna-metamaterial system.

The direction of the metamaterial is important to improve gain of the patch antenna, since the metamaterial has anisotropic behavior. Therefore, they are mounted such that the center of SRR are parallel to H field and MT is parallel to E field direction of the antenna. The distance between the periodically arranged metamaterials is 2 mm. The simulated and measured results of microstrip patch antenna covered with metamaterial are shown in Fig. 5.

While the return loss decreases down to -20.27 dB in HFSS simulation and -23.33 dB in CST simulation, it is observed -15.1 dB in measurement at 2.4 GHz. This means 60.3% enhancement of the antenna gain (return loss) with respect to antenna without metamaterial. The enhancement results of antenna with and without metamaterial is indicated in Table II. Good gain improvement (return loss) is obtained for all of HFSS-CST and measurement results. Although, measured return loss (S_{11}) of the patch antenna with metamaterial indicates several modes at different frequencies as shown in Fig. 5 (c), but these modes are not sufficient to mention about new extra radiation frequencies. Since the return losses of these extra modes are higher than -10 dB.

Table II: Comparison of simulation and measurement results of return loss (S_{11}).

	HFSS	CST	Measurement
W/O MTM	-13.6812 dB	-16.64 dB	-9.42 dB
with MTM	-20.2712 dB	-23.33 dB	-15.1 dB
Gain	-6.59 dB	-6.69 dB	-5.68 dB

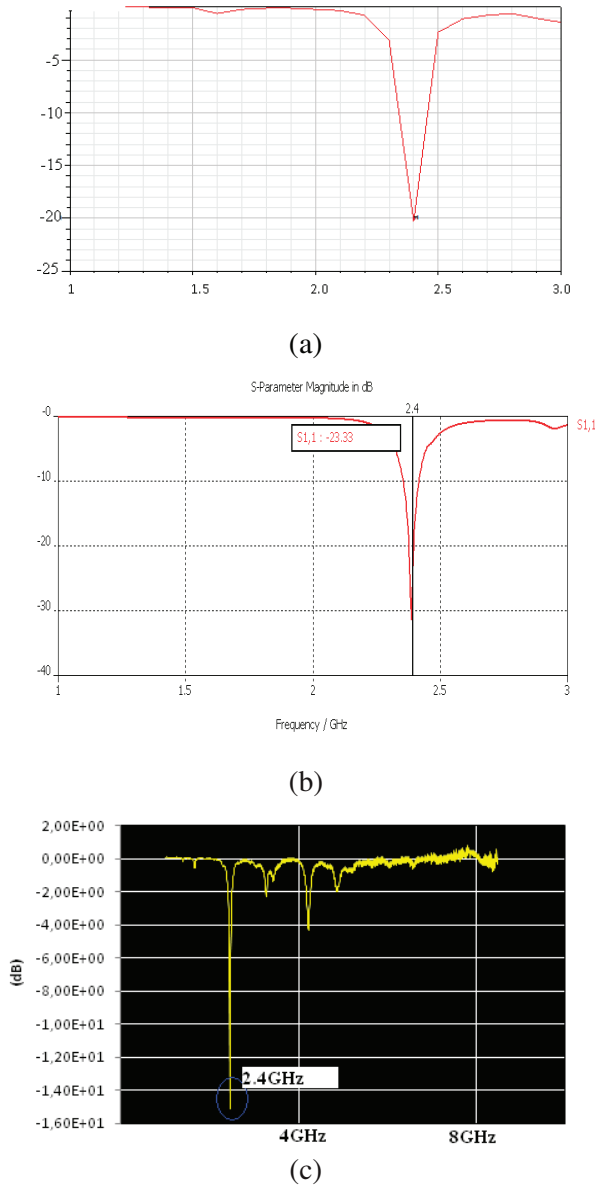


Fig. 5. (a) HFSS simulation, (b) CST simulation, (c) and measurement results of patch antenna with metamaterial.

It is well known that the radiation pattern of the antenna with and without metamaterial give exact idea about the gain of the antenna system, since the return loss (S_{11}) is not enough alone to decide the antenna performance. The radiation patterns of the patch antenna with and without metamaterial are evaluated by HFSS as shown in Figs. 6 and 7. The radiation patterns of H plane are simulated at every 30° between $0^\circ/180^\circ$. Although, the maximum radiation gain of the antenna without metamaterial is -8 dB (Fig. 7), it reaches

up to +20 dB for antenna with metamaterial (Fig. 6). These exhibits that metamaterial not only provide minimization of return loss (S_{11} value) but also give chance to enhancement of the antenna gain.

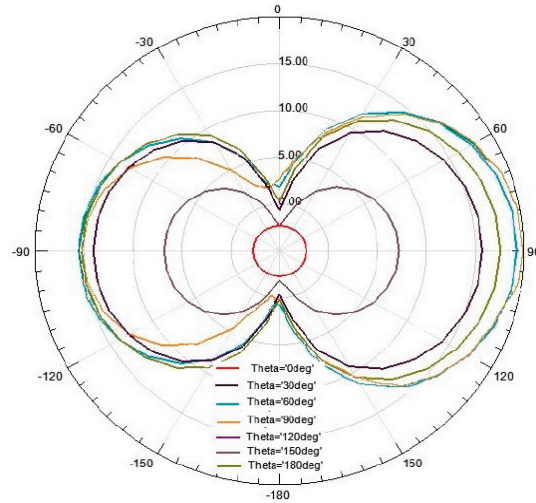


Fig. 6. HFSS simulation of the radiation pattern for the patch antenna with metamaterial.

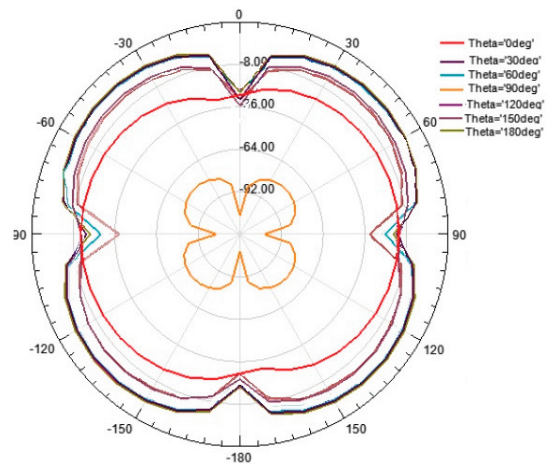


Fig. 7. HFSS simulation of the radiation pattern for the patch antenna without metamaterial.

Beside the simulations of radiation pattern, measurement is also realized to observe the effect of metamaterial on patch antenna by using MATS1000. The HFSS simulation for patch antenna without metamaterial and measurement result for patch antenna with metamaterial are shown in Fig. 8. Two different antennas are used at the measurement. One of them is metamaterial mounted patch antenna and the other one is ring

antenna to observe the radiation pattern of H plane. Whereas simulation result of H plane radiation gain is around -72 dB, measurement result is much better (-47.5 dB). These results indicate the enhancement of antenna radiation gain due to the metamaterial.

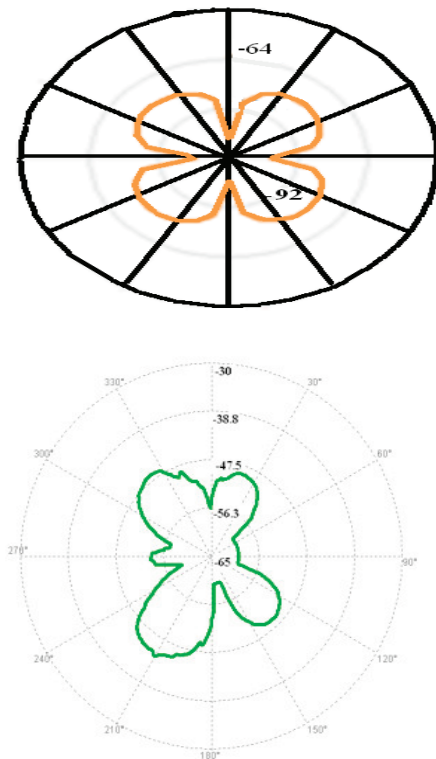


Fig. 8. Simulation and measurement radiation pattern results of patch antenna without and with metamaterial (H plane).

III. CONCLUSIONS

In this study, simulation, fabrication, and measurement are investigated for microstrip patch antenna covered with metamaterial composed of SRR and MS. The results show that good improvement in the antenna characteristics in terms of gain is achieved. The gain of the microstrip patch antenna with metamaterial is increased by 6.69 dB from simulation and 5.68 dB from measurement. It can be concluded that microstrip patch antenna based on metamaterial exhibits improvement on the antenna gain performance. Therefore, metamaterials provide potential application areas to antenna researchers, such as improvement of the gain or radiation properties of any type of antenna.

ACKNOWLEDGEMENT

We would like to thank the Scientific and Technological Research Council of Turkey (Tubitak-113E290) for its financial support.

REFERENCES

- [1] R. Waterhouse, *Microstrip Patch Antennas—A Designer's Guide*, Kluwer Academic Publishers, Boston, MA, 2003.
- [2] M. Palandoken, A. Grede, and H. Henke, "Broadband microstrip antenna with left-handed metamaterials," *IEEE Trans. Antennas Propag.*, vol. 57, pp. 331-338, 2009.
- [3] S. Burokur, M. Latrach, and S. Toutain, "Theoretical investigation of a circular patch antenna in the presence of left-handed metamaterial," *IEEE Antennas Wirel. Propag. Lett.*, vol. 4, pp. 183-186, 2005.
- [4] T. Liu, X.-Y. Cao, J. Gao, Q. Yang, and W.-Q. Li, "Design of miniaturized broadband and high gain metamaterial patch antenna," *Microwave Opt. Technol. Lett.*, vol. 53, pp. 2858-2861, 2011.
- [5] M. Veysi and A. Jafargholi, "Directivity and bandwidth enhancement of proximity-coupled microstrip antenna using metamaterial cover," *Applied Comp. Electromagnetics Society (ACES) Journal*, vol. 27, no. 3, pp. 261-270, March 2012.
- [6] A. Jafargholi and M. Kamyab, "Dipole antenna miniaturization using single-cell metamaterial," *Applied Comp. Electromagnetics Society (ACES) Journal*, vol. 27, no. 3, pp. 261-270, March 2012.
- [7] R. Ziolkowski, "Double negative metamaterial design, experiment and applications," *IEEE Trans. Microwave Theory Tech.*, vol. 51, pp. 396-399, 2003.
- [8] J. Liu, W. Shao, and B. Wang, "A dual-band metamaterial design using double SRR structures," *Applied Comp. Electromagnetics Society (ACES) Journal*, vol. 26, no. 6, pp. 459-463, June 2011.
- [9] M. Tang, S. Xiao, D. Wang, J. Xiong, K. Chen, and B. Wang, "Negative index of reflection in planar metamaterial composed of single split-ring resonators," *Applied Comp. Electromagnetics Society (ACES) Journal*, vol. 26, no. 3, pp. 250-258, March 2011.
- [10] W. Abdouni, A.-C. Tarot, and A. Sharaiha, "Realization of a compact patch antenna over an artificial magneto-dielectric substrate," *24th Annual Review of Progress in Applied Comp. Electromagnetics (ACES)*, pp. 149-152, Niagara Falls, Canada 2008.
- [11] C. Fazi, S. Shi, I. Mirza, and D. Prather, "Split ring resonator slab modeling for a metamaterial loaded loop antenna," *23rd Annual Review of Progress in*

Applied Comp. Electromagnetics (ACES), pp. 117-122, Verona, Italy, March, 2007.

- [12] Z. Szabo, G. Park, R. Hedge, and E.-P. Li, "A unique extraction of metamaterial parameters based on Kramers–Kronig relationship," *IEEE Trans. Microwave Theory Tech.*, vol. 58, pp.2646-2653, 2010.
- [13] Y. Lo, "Theory and experiment on microstrip antennas," *IEEE Trans. Antennas Propag.*, vol. 27 pp. 137-145, 1979.
- [14] R. Hwang and S. Peng, "Surface-wave suppression of resonance type periodic structures," *IEEE Trans. Antennas Propag.*, vol. 51, pp. 1221-1229, 2003.
- [15] S. Yeap and Z. Chen, "Microstrip patch antennas with enhanced gain by partial substrate removal," *IEEE Trans. Antennas Propag.*, vol. 58, pp. 2811-2816, 2010.
- [16] J. Colburn and Y. Rahmat-Samii, "Patch antennas on externally perforated high dielectric permittivity material," *Electron Lett.*, vol. 31, pp. 1710-1712, 1995.
- [17] H. Mosallaei and K. Sarabandi, "Antenna miniaturization and bandwidth enhancement using a reactive impedance substrate," *IEEE Trans. Antennas Propag.*, vol. 52, pp. 2403-2414, 2004.
- [18] P. Ikonen, S. Maslovski, and S. Tretyakov, "PIFA loaded with artificial magnetic material: Practical example for two utilization strategies," *Microwave Opt. Technol. Lett.*, vol. 46, pp. 554-556, 2005.
- [19] P. Ikonen, S. Maslovski, C. Simovski, and S. Tretyakov, "On artificial magneto dielectric loading for improving the impedance bandwidth properties of microstrip antennas," *IEEE Trans. Antennas Propag.*, vol. 54, pp. 1654-1662, 2006.
- [20] A. Nicolson and G. Ross, "Measurement of the intrinsic properties of materials by time domain techniques," *IEEE Trans. on Instrumentation and Measurement*, IM-19, pp. 377-382, 1970.
- [21] W. Weir, "Automatic measurement of complex dielectric constant and permeability at microwave frequencies," *Proceedings of the IEEE*, vol. 62, pp. 33-36, 1974.



Esra DOĞAN received the B.S degree in Electrical – Electronics Engineering from the Mustafa Kemal University in 2010 and M.S degree from the Mustafa Kemal University, Hatay, in Electrical-Electronics Engineering in 2012. She worked at Mustafa Kemal University. Her current research interests are Left Hand Metamaterial, Metamaterial antenna Applications, antenna design and testing.



Muharrem Karaaslan received the Ph.D. degree in Physics Department from University of Çukurova, Adana, Turkey, in 2009. He is the coauthor of about 20 scientific contributions published in international books, journals and peer-reviewed conference proceedings. His research interest includes the applications of metamaterials in the analysis and synthesis of antennas, waveguides.



Emin Ünal received the Ph.D. degree in Electrical and Electronics Engineering from University of Gaziantep, Turkey, in 1994. He is the coauthor of about 20 scientific contributions published in international books, journals and peer-reviewed conference proceedings. His research interest includes Frequency selective surfaces and metamaterials.



Dilek Kapusuz received the Associate degree in Industrial Electronics Department from 9 Eylül University, İzmir, Turkey, in 2001, and B.S degree as an Electronics Teacher in Electronics and Computer Education Department from Kocaeli University Technical Education Faculty, Kocaeli, Turkey, in 2007. She has carried out some studies on SRR Structures and Metamaterials as to present her Certificate of Completion Project between the years of 2005-2006.



Cumali Sabah (M'12) was born in Iskenderun, Turkey. He received the B.Sc., M.Sc., and Ph.D. degrees in electrical and electronics engineering from the University of Gaziantep, Gaziantep, Turkey. He is currently with Goethe University, Frankfurt, Germany, where he is the Group Leader of the Metamaterial Group of the Physikalisches Institut, and is also responsible for the management of postdoctoral studies and the supervision of undergraduate and graduate students. His research interests include the microwave and electromagnetic investigation of unconventional materials and structures, wave propagation, scattering, complex media, and metamaterials and their applications.

Application of the Protruded Structures to Design an UWB Slot Antenna with Band-Notched Characteristic

N. Ojaroudi ¹, M. Mehranpour ¹, S. Ojaroudi ², and Y. Ojaroudi ²

¹Young Researchers Club
Ardabil Branch, Islamic Azad University, Ardabil, Iran
n.ojaroudi@yahoo.com, mehranpour.mehdi@gmail.com

²Young Researchers Club
Germi Branch, Islamic Azad University, Germi, Iran
s.ojaroudi.p@gmail.com, y.ojaroudi@iaugermi.ac.ir

Abstract — A different method to design a novel ultra-wideband (UWB) slot antenna with band-notch performance is presented. In order to increase the impedance bandwidth of the slot antenna, we use a rectangular slot with a pair of L-shaped strips protruded inside the rectangular slot in the ground plane that with this structure UWB frequency range can be achieved. Additionally, by using square-ring radiating stub with two Γ -shaped strips protruded inside the square-ring stub, a frequency notch band performance has been obtained. The designed antenna has a small size of 20×20 mm² while showing the radiation performance in the frequency band of 3.07 GHz to over 14.67 GHz with a band rejection performance in the frequency band of 5.05 GHz to 5.93 GHz. Simulated and experimental results obtained for this antenna show that it exhibits good radiation behavior within the UWB frequency range.

Index Terms — Protruded strips, slot antenna, and UWB Systems.

I. INTRODUCTION

It is a well-known fact that planar microstrip antennas present really appealing physical features, such as simple structure, small size, and low cost [1]. Due to all these interesting characteristics, planar antennas are extremely attractive to be used in emerging ultra-wideband (UWB) applications. [2-5]. In the UWB communication systems, one of the key issues is the design of a compact antenna while providing wideband characteristic over the

whole operating band. Consequently, a number of planar slot antennas with different geometries have been experimentally characterized [6-9].

Despite the advantages of UWB, the frequency range for UWB systems between 3.1 GHz–10.6 GHz will cause interference to the existing wireless communication systems for example the wireless local area network (WLAN) for IEEE 802.11a operating in 5.15 GHz–5.35 GHz and 5.725 GHz–5.825 GHz bands, so the UWB antenna with a band-notched function is required [10-14].

In this paper, to achieve the above purposes such as the frequency range for UWB systems and single band-notched characteristic (to avoid the interference between UWB and WLAN systems), at the first step of the design algorithm, an extra rectangular slot with a pair of L-shaped strips protruded inside the rectangular slot in the ground plane was used to enhance the bandwidth. Also the modified square-ring radiating stub with two protruded Γ -shaped strips was applied to generate a band-notched performance.

II. ANTENNA DESIGN

The proposed slot antenna fed by a 50-Ohm microstrip line is shown in Fig. 1, which is printed on an FR4 substrate of thickness 0.8 mm, and permittivity 4.4. The width of the microstrip feed line is fixed at 1.5 mm. The basic antenna structure consists of a square radiating stub, a feed line, and a ground plane with a rectangular slot. The square-ring radiating stub with two Γ -shaped

strips protruded inside the square-ring stub is connected to a feed line, as shown in Fig. 1. On the other side of the substrate, a conducting ground plane with a rectangular slot with a pair of L-shaped strips protruded inside the rectangular slot in the ground plane is placed. The proposed antenna is connected to a 50Ω SMA connector for signal transmission.

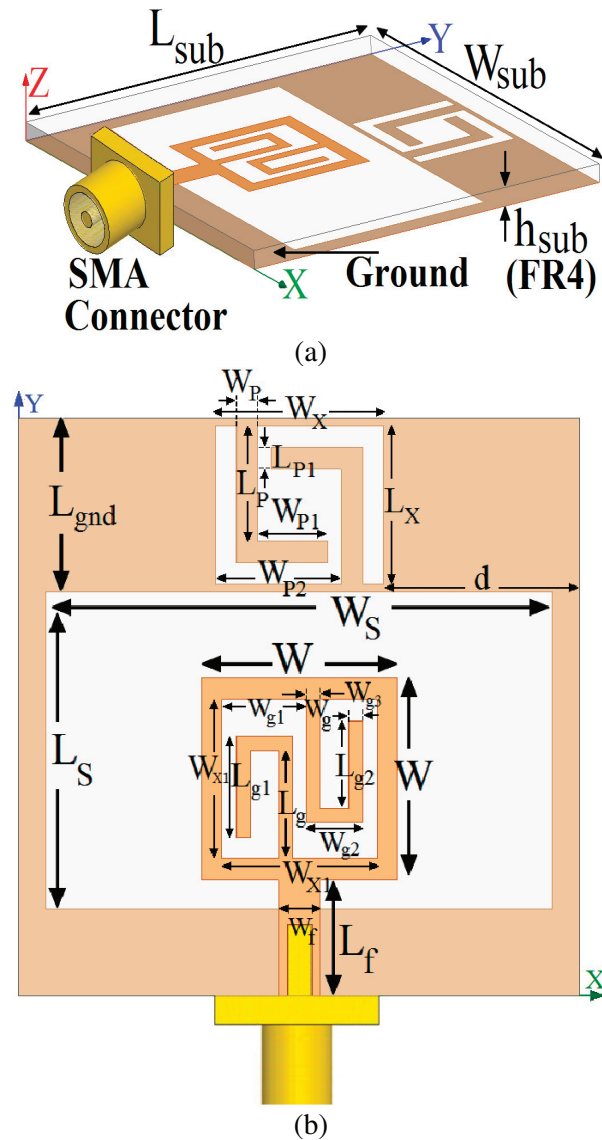


Fig. 1. Geometry of the proposed slot antenna, (a) side view and (b) top view.

In this work, we start by choosing the aperture length L_s . We have a lot of flexibility in choosing this parameter. The length of the aperture mostly affects the antenna bandwidth. As L_s decreases, so

does the antenna BW and vice versa. In the next step, we have to determine the aperture width W_s . The aperture width is approximately, where is the slot wavelength that depends on a number of parameters such as the slot width as well as the thickness and dielectric constant of the substrate on which the slot is fabricated. The last and final step in the design is to choose the width of the radiating patch W . This parameter is approximately, where is the guided wavelength in the microstrip line [3].

In this study, to design a novel antenna, the modified protruded L-shaped and Γ -shaped strips are placed inside rectangular slot in the ground plane and square-ring stub, respectively. Regarding defected ground structures (DGS) theory, the creating slots in the ground plane provide additional current paths. Moreover, these structures change the inductance and capacitance of the input impedance, which in turn leads to change the bandwidth [4-6]. Therefore, by cutting an extra rectangular slot with a pair of L-shaped strips in the ground plane, much enhanced impedance bandwidth may be achieved.

In addition, to create a desired frequency band-stop characteristic, a pair of Γ -shaped strips is protruded inside square-ring radiating stub. At the notched frequency, the current flows are more dominant around the Γ -shaped strips, and they are oppositely directed between the parasitic element and the radiating stub. As a result, the desired high attenuation near the notch frequency can be produced [10-12]. Final values of the presented antenna design parameters are specified in Table. I.

Table. I. Final dimensions of the antenna.

Parameter	W_{sub}	L_{sub}	h_{sub}	W_f	L_f	W
(mm)	20	20	0.8	1.5	4	7
Parameter	W_s	L_s	W_x	L_x	W_{x1}	W_p
(mm)	18	11	6	5.5	5	1
Parameter	L_p	W_{p1}	L_{p1}	W_{p2}	W_g	L_g
(mm)	3.25	2.5	1.5	4.5	0.5	4
Parameter	W_{g1}	L_{g1}	W_{g2}	W_{g3}	d	L_{gnd}
(mm)	3.25	3	1.25	0.5	7	6

III. RESULTS AND DISCUSSIONS

The proposed microstrip-fed slot antenna with various design parameters were constructed, and the numerical and experimental results of the input

impedance and radiation characteristics are presented and discussed. The analysis and performance of the proposed antenna is explored by using Ansoft simulation software high-frequency structure simulator (HFSS) [15], for better impedance matching.

The configuration of the presented slot antenna was shown in Fig. 1. Geometry for the ordinary square slot antenna (Fig. 2 (a)), with a rectangular slot with a pair of L-shaped strips protruded inside the rectangular slot in the ground plane (Fig. 2 (b)), and the proposed antenna (Fig. 2 (c)) structures are shown in Fig. 2. Return loss characteristics for structures that shown in Fig. 2 are compared in Fig. 3.

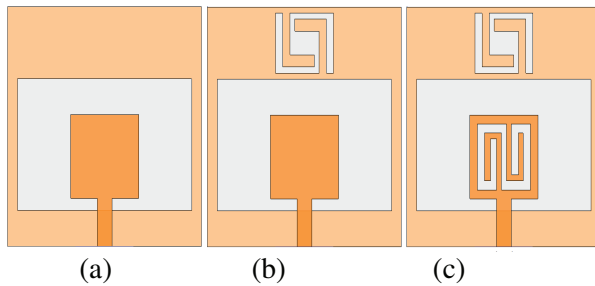


Fig. 2. (a) Ordinary square antenna with two L-shaped slits, (b) with four L-shaped slits, and (c) the proposed antenna structure.

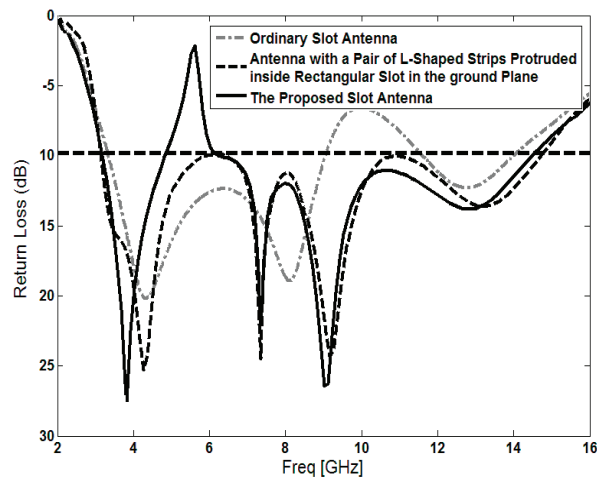


Fig. 3. Simulated return loss characteristics for the various structures of the antenna shown in Fig. 2.

As shown in Fig. 3, it is observed that the upper frequency bandwidth is affected by using the rectangular slot with a pair of L-shaped strips

protruded inside the rectangular slot in the ground plane. In the proposed design, by using the modified DGS consist of the extra rectangular slot with a pair of L-shaped strips in the ground plane, an additional resonance at 9 GHz is excited and hence, much wider impedance bandwidth can be produced, especially at the higher frequencies. By using this modified structure in the ground plane, the usable upper frequency of the antenna is extended from 8.7 GHz to 14.67 GHz. Also, the WLAN band-notched property is sensitive to the square-ring radiating stub with two Γ -shaped strips protruded inside the square-ring stub.

In the proposed antenna configuration, the ordinary rectangular slot can provide the fundamental and next higher resonant radiation band at 4.1 GHz and 8 GHz, respectively, in the absence of the modified protruded strips. The upper frequency bandwidth is significantly affected using the pair of protruded L-shaped strips inside the extra rectangular slot in the ground plane. This behavior is mainly due to the change of surface current path by the dimensions of L-shaped strips as shown in Fig. 4 (a). In addition, by using these modified DGS on the other side of substrate, the impedance bandwidth is effectively improved at the upper frequency. As shown in Fig. 4 (b), the current is concentrated on the edges of the interior and exterior of the protruded Γ -shaped strips inside the square-ring radiating stub at the notched frequency (5.5 GHz). This figure shows that the electrical current for the notched frequency (Fig. 4 (b)) does change direction along the bottom and top edge of the radiating stub [16-17].

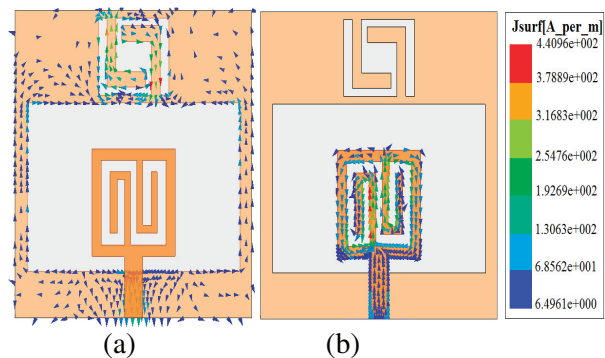


Fig. 4. Simulated surface current distributions for the proposed antenna at, (a) 9 GHz (resonance frequency) and (b) 5.5 GHz (notched frequency).

Figure 5 shows the simulated VSWR curves with different values of L_g . As shown in Fig. 5, when the length of the protruded Γ -shaped strips increases from 3.25 mm to 4.50 mm, the centre of notch frequency is decreases from 5.86 GHz to 5.11 GHz. From these results, we can conclude that the notch frequency is controllable by changing the length of the protruded Γ -shaped strips [18-19].

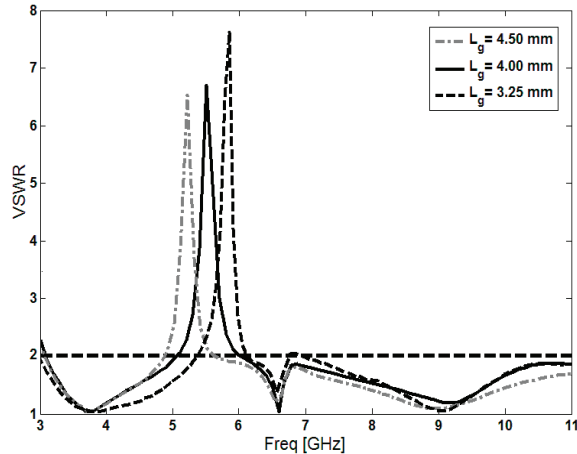


Fig. 5. Simulated VSWR for the proposed antenna with different values of L_g .

The proposed antenna with optimal design as shown in Fig. 6 was built and tested. The VSWR characteristic was measured using a HP 8720ES network analyzer in an anechoic chamber. The radiation patterns have been measured inside an anechoic chamber using a double-ridged horn antenna as a reference antenna placed at a distance of 2 m.

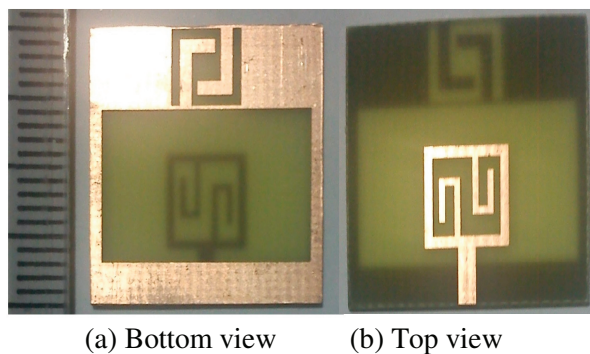


Fig. 6. Prototype of the realized antenna.

The measured and simulated VSWR characteristics of the proposed antenna were shown in Fig. 7. The fabricated antenna has the frequency band of 3.07 to over 14.67 GHz with a rejection band around 5.05 to 5.93 GHz.

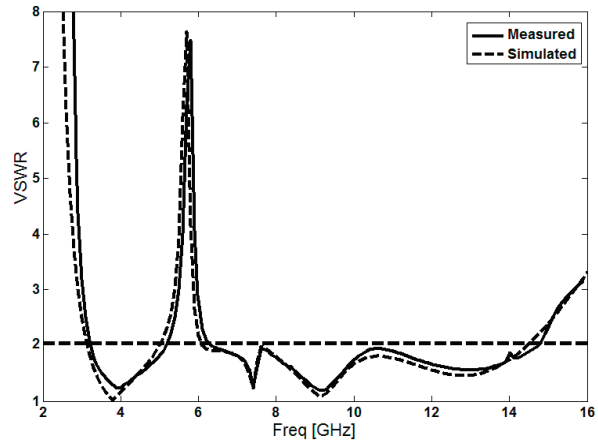


Fig. 7. Measured and simulated VSWR for the proposed antenna.

Figure 8 depicts the measured radiation patterns of the proposed antenna including the co-polarization and cross-polarization in the H-plane (x - z plane) and E-plane (y - z plane). It can be seen that quasi-omnidirectional radiation pattern can be observed on x - z plane over the whole UWB frequency range, especially at the low frequencies. The radiation patterns on the y - z plane display a typical figure-of-eight, similar to that of a conventional dipole antenna. It should be noticed that the radiation patterns in E-plane become imbalanced as frequency increases because of the increasing effects of the cross polarization. The patterns indicate at higher frequencies, more ripples can be observed in both E- and H-planes owing to the generation of higher-order modes [20-23].

IV. CONCLUSION

In this paper, a novel design of UWB slot antenna with variable band-notched function is proposed. The presented slot antenna can operate from 3.07 GHz to 14.67 GHz for $VSWR < 2$ with a rejection band around 5.05 GHz-5.93 GHz. By using a rectangular slot with a pair of protruded L-shaped strips in the ground plane, an additional resonance at higher frequency range is excited and much wider impedance bandwidth is produced. In

order to generate a frequency band-stop performance, we use the square-ring radiating stub with two protruded Γ -shaped strips. The designed antenna has a small size. The measured results showed good agreement with the simulated results. Experimental results show that the presented slot antenna can be a good candidate for UWB applications.

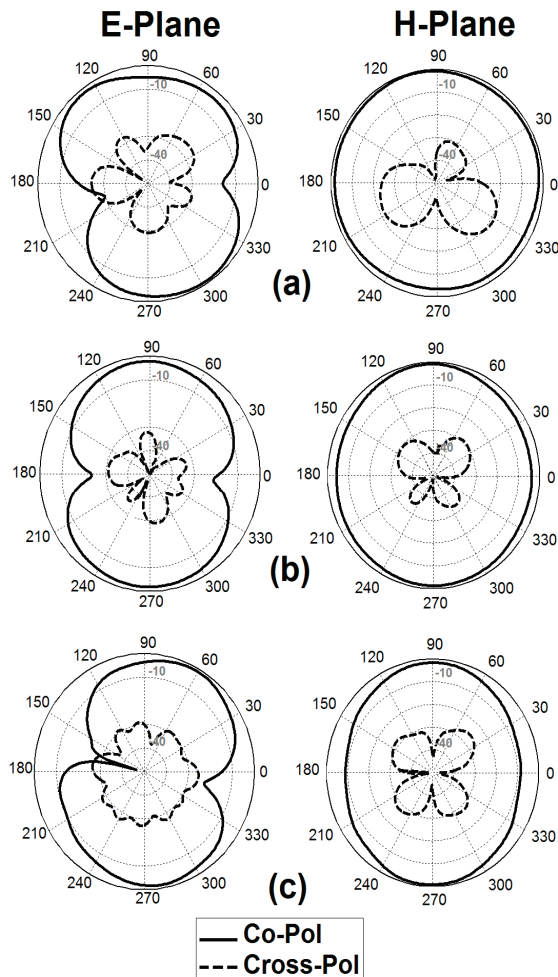


Fig. 8. Measured radiation patterns of the proposed antenna (a) 4 GHz, (b) 7 GHz, and (c) 10 GHz.

ACKNOWLEDGMENT

The authors are thankful to Microwave Technology (MWT) Company staff for their beneficial and professional help (www.microwave-technology.com).

REFERENCES

- [1] H. Schantz, *The Art and Science of Ultra Wideband Antennas*, Artech House 2005.
- [2] N. Ojaroudi, "A new design of koch fractal slot antenna for ultra-wideband applications," *21th Telecommunications Forum, TELFOR*, Belgrade, Serbia, pp. 1051-1054, November 2013.
- [3] J. Sze and K. Wong, "Bandwidth enhancement of a microstrip line-fed printed wide-slot antenna," *IEEE Trans. Antennas Propag.*, vol. 49, pp. 1020-1024, 2001.
- [4] M. N.-Jahromi and N. K.-Barchloui, "Analysis of the behavior of Sierpinski carpet monopole antenna," *Applied Computational Electromagnetics Society (ACES) Journal*, vol. 24, no. 1, pp. 32-36, February 2009.
- [5] N. Ojaroudi, "Compact UWB monopole antenna with enhanced bandwidth using rotated L-shaped slots and parasitic structures," *Microw. Opt. Technol. Lett.*, vol. 56, pp. 175-178, 2014.
- [6] N. Ojaroudi, S. Amiri, and F. Geran, "A novel design of reconfigurable monopole antenna for UWB applications," *Applied Computational Electromagnetics Society (ACES) Journal*, vol. 28, no. 6, pp. 633-639, July 2013.
- [7] W. Weng, "Optimal design of an ultra-wideband antenna with the irregular shape on radiator using particle swarm optimization," *Applied Computational Electromagnetics Society (ACES) Journal*, vol. 27, no. 5, pp. 427-434, May 2012.
- [8] M. Mighani, M. Akbari, and N. Felegari, "A novel SWB small rhombic microstrip antenna with parasitic rectangle into slot of the feed line," *Applied Computational Electromagnetics Society (ACES) Journal*, vol. 27, no. 1, pp. 74-79, January 2012.
- [9] R. Azim, M. Islam, and N. Misran, "Design of a planar UWB antenna with new band enhancement technique," *Applied Computational Electromagnetics Society (ACES) Journal*, vol. 26, no. 10, pp. 856-862, October 2011.
- [10] N. Ojaroudi, "Small microstrip-fed slot antenna with frequency band-stop function," *21th Telecommunications Forum, TELFOR 2013*, 27 - 28 November, 2013, Belgrade, Serbia., pp. 1047-1050, 2013.
- [11] N. Ojaroudi, "Application of protruded strip resonators to design an UWB slot antenna with WLAN band-notched characteristic," *Progress in Electromagnetics Research C*, vol. 47, pp. 111-117, 2014.
- [12] M. Ojaroudi, N. Ojaroudi, and Y. Ebazadeh, "Dual band-notch small square monopole antenna with enhanced bandwidth characteristics for UWB applications," *Applied Computational*

- Electromagnetics Society (ACES) Journal*, vol. 27, no. 5, pp. 420-426, May 2012.
- [13] G. Zhang, J. Hong, B. Wang, and G. Song, "Switched band-notched UWB/ WLAN monopole antenna," *Applied Computational Electromagnetics Society (ACES) Journal*, vol. 27, no. 3, pp. 256-260, March 2012.
- [14] M. Mighani, M. Akbari, and N. Felegari, "A CPW dual band notched UWB antenna," *Applied Computational Electromagnetics Society (ACES) Journal*, vol. 27, no. 4, pp. 352-359, April 2012.
- [15] *Ansoft High Frequency Structure Simulator (HFSS)*, ver. 13, Ansoft Corporation, 2010.
- [16] J. William and R. Nakkeeran, "A new UWB slot antenna with rejection of WiMax and WLAN bands," *Applied Computational Electromagnetics Society (ACES) Journal*, vol. 25, no. 9, pp. 787-793, September 2010.
- [17] T.-G. Ma and S.-J. Wu, "Ultra-wideband band-notched folded strip monopole antenna," *IEEE Trans. Antennas Propag.*, vol. 55, pp. 2473-2479, 2007.
- [18] C. Liu, T. Jiang, and Y. Li, "A novel UWB filter with notch-band characteristic using radial-UIR/SIR loaded stub resonators," *Journal of Electromagnetic Waves and Applications*, vol. 25, pp. 233-245, 2011.
- [19] J. Ding, Z. Lin, Z. Ying, and S. He, "A compact ultra-wideband slot antenna with multiple notch frequency bands," *Microwave and Optical Technology Letter*, vol. 49, no. 12, pp. 3056-3060, 2007.
- [20] C. Sim, W. Chung, and C. Lee, "Planar UWB antenna with 5 GHz band rejection switching function at ground plane," *Progress In Electromagnetics Research*, vol. 106, pp. 321-333, 2010.
- [21] N. Ojaroudi, "Design of ultra-wideband monopole antenna with enhanced bandwidth," *21th Telecommunications Forum*, TELFOR, Belgrade, Serbia, pp. 1043-1046, 27 – 28 November 2013.
- [22] N. Ojaroudi, "Microstrip monopole antenna with dual band-stop function for UWB applications," *Microw. Opt. Technol. Lett.*, vol. 56, pp. 818-822, 2014.
- [23] N. Ojaroudi, Sh. Amiri, and F. Geran, "Reconfigurable monopole antenna with controllable band-notched performance for UWB communications," *20th Telecommunications Forum*, TELFOR, Belgrade, Serbia, pp. 1176-1178, November 2013.